Universidad Miguel Hernández

Programa de Doctorado en Tecnologías Industriales y de Telecomunicación

Universidad Autónoma de Nuevo León

Facultad de Ingeniería Mecánica y Eléctrica
Programa de Doctorado en Ingeniería Eléctrica

Decoding kinematic variables from electroencephalographic signals during lower limb mobility protocols

Thesis presented by:

Luis Antonio Mercado Cerda

Director: Dr. José María Azorín Poveda
Co-director: Dra. Griselda Quiroz Compeán

2021

Esta Tesis Doctoral se presenta bajo la modalidad de tesis convencional. El indicio de calidad asociado a la misma corresponde a la contribución “Offline Lower-Limb Kinematic Decodification by Segments of EEG Signals” presentada en el congreso internacional “40th International Conference of the IEEE Engineering in Medicine and Biology Society” y publicada en las actas de dicho congreso. La referencia bibliográfica completa de esta publicación es la siguiente:

- Luis Mercado, J.M. Azorín, Miguel Platas, A. Úbeda, and Griselda Quiroz, Offline Lower-Limb Kinematic Decodification by Segments of EEG Signals, Proceedings of the 40th International Conference of the IEEE Engineering in Medicine and Biology Society (Honolulu, HI, July 17-21, 2018), pp. 2398-2401, 2018, DOI: 10.1109/EMBC.2018.8512840, ISBN: 978-1-5386-3646-6.

AUTORIZACIÓN DE PRESENTACIÓN DE TESIS DOCTORAL EN LA MODALIDAD DE TESIS CONVENCIONAL

Director: Dr. José M. Azorín Poveda,
Codirectora: Dra. Griselda Quiroz Compeán

Título de la tesis: ***Decoding kinematic variables from electroencephalographic signals during lower limb mobility protocols***

Autor: Luis Antonio Mercado Cerda

Universidad Miguel Hernández de Elche, Universidad Autónoma de Nuevo León

El director y codirectora de la tesis reseñada AUTORIZAN SU PRESENTACIÓN EN LA MODALIDAD DE TESIS CONVENCIONAL.

En Elche, a 2 de julio de 2021.

Fdo: Dr. José María Azorín Poveda

Fdo: Dra. Griselda Quiroz Compeán

PROGRAMA DE DOCTORADO EN TECNOLOGÍAS INDUSTRIALES
Y DE TELECOMUNICACIÓN

Dr. D. Óscar Reinoso García, Coordinador del Programa de Doctorado en Tencologías Industriales y de Telecomunicación de la Universidad Miguel Hernández de Elche.

Certifica

Que el trabajo realizado por D. Luis Antonio Mercado Cerda titulado **Decoding kinematic variables from electroencephalographic signals during lower limb mobility protocols** ha sido dirigido por el Dr. José María Azorín Poveda y codirigido por la Dra. Griselda Quiroz Compeán y se encuentra en condiciones de ser leído y defendido como Tesis Doctoral ante el correspondiente tribunal en la Universidad Miguel Hernández de Elche.

Lo que firmo para los efectos oportunos.

Fdo.: Dr. D. Óscar Reinoso García
Coordinador del Programa de Doctorado en Tecnologías Industriales y de Telecomunicación

UANL
UNIVERSIDAD AUTÓNOMA DE NUEVO LEÓN

FIME
FACULTAD DE INGENIERÍA MECÁNICA Y ELÉCTRICA

PROGAMA DE DOCTORADO EN INGENIERÍA ELÉCTRICA

Dr. Ernesto Vázquez Martínez, Coordinador Académico del Programa de Doctorado en Ingeniería Eléctrica de la Facultad de Ingeniería Mecánica y Eléctrica de la Universidad Autónoma de Nuevo León.

Certifica

Que el trabajo realizado por D. Luis Antonio Mercado Cerda titulado **Decoding kinematic variables from electroencephalographic signals during lower limb mobility protocols** ha sido dirigida por el Dr. José María Azorín Poveda y codirigido por la Dra. Griselda Quiroz Compeán y se encuentra en condiciones de ser leído y defendido como Tesis Doctoral ante el correspondiente tribunal en la Universidad Miguel Hernández de Elche. Cabe mencionar que D. Luis Antonio Mercado realizó una estancia de investigación en la Universidad Miguel Hernández de Elche en el period comprendido entre el 15 de marzo de 2017 y el 15 de enero de 2018.

Lo firmo para los efectos oportunos, en San Nicólas de los Garza, Nuevo León, México, a 8 de marzo de 2021.

Fdo.: Dr. Ernesto Vázquez Martínez
Coordinador Académico
Programa de Doctorado en Ingeniería Eléctrica
evazquez@gmail.com
(81) 1801-1740

ACKNOWLEDGMENTS

First I would like to thank my thesis advisor, Dr. Griselda Quiroz Compeán, for all her patience, support, and specially her guidance in the development and writing of this thesis.

I would like to give my gratitude to Dr. Juan Angel Rodríguez Liñán, Dr. Luis Martín Torres Treviño, and Dr. Miguel Ángel Platas Garza for their assistance and teachings that formed part of the basis of this thesis. I would also like to thank Dr. Dania Gutiérrez Ruiz for providing her assistance, and part of the required equipment for the experiments. Thanks to all the test subjects for granting their time and services in performing the experiments.

I would like to thank Dr. José M. Azorín, for receiving me as a guest and as a doctorate candidate in the Department of Automation and Systems Engineering, in the Brain-Machine Interface Systems Lab, of the Miguel Hernández University of Elche during my research stay between March 15, 2017 and December 28, 2017. Furthermore, thanks to my friends in Elche, whom also welcomed me: Yordhana, Edu, Marisol, Ándres, Quique, and José Antonio; for those brunches and meals we shared.

Also thanks to my friends, for giving me support and friendship during the development of this thesis.

Finally, I would like to specially thank my parents. Dr. Luis Antonio Mercado Gómez and Ms. Maria Guillermina Cerda Ruiz for their unconditional love and support. For their live teachings and guidance throughout my life.

Thank you God, for granting me the strength, hearing my prayers, and blessing me with all the supporting people that surround me.

Contents

Acknowledgments iii

List of Figures viii

List of Tables xviii

Abstract xxi

Resumen xxiii

1 Introduction 1

1.1 Motivation 1

1.2 Problem Description 6

1.3 Hypothesis 7

1.4 Objectives 7

1.4.1 Main Objective 7

1.4.2 Particular Objectives 7

1.5 Thesis Contribution 8

2 Methods 11

2.1 Randomness & nonlinear dynamical analysis 11

2.1.1 Hurst exponent 12
2.1.2 Correlation dimension 15
2.1.3 Largest Lyapunov exponent 17
2.2 Decodification 20
2.2.1 Linear optimum filter 21
2.2.2 Genetic Algorithm 27
2.2.3 Evaluation metrics 30

3 Experimental Setups **33**
3.1 Synchronous protocols 34
3.1.1 Data Acquisition 36
3.1.2 Signal Preprocessing 38
3.2 Asynchronous protocols 41
3.2.1 Data Acquisition 42
3.2.2 Signal Preprocessing 44

4 Results **47**
4.1 Randomness & nonlinear dynamical analysis 47
4.1.1 Hurst exponent 49
4.1.2 Correlation dimension 52
4.1.3 Largest Lyapunov exponent 52
4.2 Parametric adjustment for asynchronous protocols 55
4.3 Decodification by segments 63
4.4 Parametric adjustment for synchronous protocols 85

4.5 Optimization by genetic algorithm 92

5 Conclusions and Future Work 105

5.1 Conclusions 105

5.2 Future Work 110

5.3 Scientific Production 111

5.3.1 Journal papers 111

5.3.2 Book Chapter 111

5.3.3 Divulgation papers 112

5.3.4 Scientific conferences 112

5.3.5 Research internships 112

A Article 115

I Introduction 116

II Materials and Methods 117

II.a Experimental Setup 117

II.b Data Acquisition 117

II.c Signal Preprocessing 118

II.d Decoding Method 119

III Results 119

IV Discussion 124

V Concluding remarks 124

Acknowledgment 125

Funding 125

References 125

Bibliography **127**

List of Figures

2.1 Different types of time series with their respective *log* plotting, and the estimated H values. Top: random series with an estimated H value close to 0.5; middle: anti-persistent time series (sine wave) with an H value close to 0; bottom: persistent time series (EEG) with an H value close to 1. 14

2.2 A schematic representation of the evolution and replacement procedure used to estimate Lyapunov exponents from experimental data. The largest Lyapunov exponent is computed from the growth of length elements. When the length of the vector between two points becomes large, a new point is chosen near the reference trajectory, minimizing both the replacement length L and the orientation change θ (Text and image taken from [56]). 19

2.3 Block diagram representation of the statistical filtering problem (modified from [74]). 22

3.1 Tasks performed by the subjects: a) raising the foot by performing an isotonic extension of the knee, and b) raising the knee by realizing an isotonic flexion on the hip joint. 36

3.2 One subject using the EEG system and performing Task 1, following indications displayed on the screen. From left to right: first resting period (indicated by a white dot on the screen), raising of the right lower limb (indicated by a green upward arrow), lowering of the right lower limb (indicated by a red downward arrow), and second resting period (indicated by a white dot). 36

3.3 Frames of the indications presented in the video to rest (white dot, 30 s), raise or lower the limb (green and red arrow respectively, 10 repetitions, each lasted 3 s); from start to finish the entire trial lasted 120 s. 36

3.4 Electrode distribution of the International 10/20 System. 19 active electrodes were connected to the MOBITA-W-32EEG system. Electrodes A1 and A2 were used as references during the impedance checking. 37

3.5 Test subject wearing three spherical markers allocated on the right hip, knee, and ankle, for video processing. 38

3.6 Type of movement performed by the subjects with a self imposed pace, i.e., an asynchronous movement. 42

3.7 Electrode distribution of the international 10/10 system. Highlighted are 32 g.LADYbird active electrodes, which were connected to two g.USBamp amplifiers (g.tec medical engineering Gmbh, Schiedlberg, Austria) interconnected through a g.INTERsync module. 43

3.8 Tag numbers of the seven IMUs connected to the TechHub with the following placement: one in the lumbar area, and the remaining six placed on both thighs, shanks, and feet. This distribution allowed to obtain the angular velocities of the hip, knee, and ankle joints of each leg. (Image taken with permission from [106]). 44

3.9 Environment of the experiment showing both equipments and two users. From left to right: the TechHub, the lumbar IMU, the EEG cap, the g.USBamp amplifiers, the inertial sensor A over the thigh, and the inertial sensor B over the shank. 45

4.1 Top: frames of the indications presented in the video to rest (white dot, 30 s), raise or lower the limb (green and red arrows respectively, 10 repetitions each, lasting 3 s). The entire trial lasted, from start to finish, 120 s. Bottom: illustration of the EEG signal segmentation of a full trial into forty time windows 3 s each (3000 samples), where blue is the resting time (20 windows, 10 at the beginning and 10 at the end), green the raising time (10 windows), and red the lowering time (10 windows) of the limb. Each time window served as inputs to the nonlinear analyses. 48

4.2 Mean and standard deviations of H calculated between eight subjects and ten trials, for nine electrodes during Task 1. 50

4.3 Mean and standard deviations of H calculated between eight subjects and ten trials, for nine electrodes during Task 2. 50

4.4 Mean and standard deviations of the EEG signal calculated between eight subjects and ten trials, for nine electrodes during Task 1. 51

4.5 Mean and standard deviations of the EEG signal calculated between eight subjects and ten trials, for nine electrodes during Task 2. 51

4.6 Mean and standard deviations of CD calculated between eight subjects and ten trials, for nine electrodes during Task 1. 53

4.7 Mean and standard deviations of CD calculated between eight subjects and ten trials, for nine electrodes during Task 2. 53

4.8 Mean and standard deviations of LLE calculated between eight subjects and ten trials, for nine electrodes during Task 1. 54

4.9 Mean and standard deviations of LLE calculated between eight subjects and ten trials, for nine electrodes during Task 2. 54

4.10 42 electrode array combinations used in the experimental setup from Section 3.2, represented in a binary table using 21 electrodes, namely FC5, FC3, FC1, FCz, FC2, FC4, FC6, C5, C3, C1, Cz, C2, C4, C6, CP5, CP3, CP1, CPz, CP2, CP4, and CP6. Colors define the combinations of regions on the scalp: red for FC, yellow for C, orange for CP, blue for FC-C, purple for FC-CP, and green for FC-C-CP. . . 56

4.11 Correlation coefficient (CC) values for eight subjects, arranged in 42 arrays by 10 delays in the past, ranged from 0.5 s to 5 s. Colors represent the different cortical regions seen in Figure 4.10. 58

4.12 Normalized root mean square error (NRMSE) values for eight subjects, arranged in 42 arrays by 10 delays in the past, ranged from 0.5 s to 5 s. Colors represent the different cortical regions seen in Figure 4.10. 59

4.13 Signal-to-noise ratio (SNR) values for eight subjects, arranged in 42 arrays by 10 delays in the past, ranged from 0.5 s to 5 s. Colors represent the different cortical regions seen in Figure 4.10. 60

4.14 Plots of the actual joint velocity of the knee (dotted line) compared to their decodification (solid line) of eight subjects. These MLR decodifications were performed with array 12 (7 electrodes) and a time delay of 3.5 s. 62

4.15 Illustrative sections for which a MLR equation was created: (a) Decoder 1 (D1) where yellow corresponds to a single MLR equation for all activities, (b) Decoder 2 (D2) where blue corresponds to resting periods, and cyan to the movement period, (c) Decoder 3 (D3) where blue corresponds to resting periods, green for the raising, and red for the lowering period. 63

4.16 Graphs of the actual hip and knee joint angles (dotted line) compared to their decodification (solid line). These decodifications were performed with a time delay of 3.5 s. For each sub-figure from top to bottom: D1, D2, and D3. 69

4.17 Graphs of the actual hip and knee joint angles (dotted line) compared to their decodification (solid line). These decodifications were performed with a time delay of 3.5 s. For each sub-figure from top to bottom: D1, D2, and D3. 70

4.18 Graphs of the actual hip and knee joint angles (dotted line) compared to their decodification (solid line). These decodifications were performed with a time delay of 3.5 s. For each sub-figure from top to bottom: D1, D2, and D3. 71

4.19 Graphs of the actual hip and knee joint angles (dotted line) compared to their decodification (solid line). These decodifications were performed with a time delay of 3.5 s. For each sub-figure from top to bottom: D1, D2, and D3. 72

4.20 Graphs of the actual hip and knee joint angles (dotted line) compared to their decodification (solid line). These decodifications were performed with a time delay of 3.5 s. For each sub-figure from top to bottom: D1, D2, and D3. 73

4.21 Graphs of the actual hip and knee joint angles (dotted line) compared to their decodification (solid line). These decodifications were performed with a time delay of 3.5 s. For each sub-figure from top to bottom: D1, D2, and D3. 74

4.22 Graphs of the actual hip and knee joint angles (dotted line) compared to their decodification (solid line). These decodifications were performed with a time delay of 3.5 s. For each sub-figure from top to bottom: D1, D2, and D3. 75

4.23 Graphs of the actual hip and knee joint angles (dotted line) compared to their decodification (solid line). These decodifications were performed with a time delay of 3.5 s. For each sub-figure from top to bottom: D1, D2, and D3. 76

4.24 Graphs of the actual hip and knee joint angles (dotted line) compared to their decodification (solid line). These decodifications were performed with a time delay of 3.5 s. For each sub-figure from top to bottom: D1, D2, and D3. 77

4.25 Graphs of the actual hip and knee joint angles (dotted line) compared to their decodification (solid line). These decodifications were performed with a time delay of 3.5 s. For each sub-figure from top to bottom: D1, D2, and D3. 78

4.26 Graphs of the actual hip and knee joint angles (dotted line) compared to their decodification (solid line). These decodifications were performed with a time delay of 3.5 s. For each sub-figure from top to bottom: D1, D2, and D3. 79

4.27 Graphs of the actual hip and knee joint angles (dotted line) compared to their decodification (solid line). These decodifications were performed with a time delay of 3.5 s. For each sub-figure from top to bottom: D1, D2, and D3. 80

4.28 Graphs of the actual hip and knee joint angles (dotted line) compared to their decodification (solid line). These decodifications were performed with a time delay of 3.5 s. For each sub-figure from top to bottom: D1, D2, and D3. 81

4.29 Graphs of the actual hip and knee joint angles (dotted line) compared to their decodification (solid line). These decodifications were performed with a time delay of 3.5 s. For each sub-figure from top to bottom: D1, D2, and D3. 82

4.30 Graphs of the actual hip and knee joint angles (dotted line) compared to their decodification (solid line). These decodifications were performed with a time delay of 3.5 s. For each sub-figure from top to bottom: D1, D2, and D3. 83

4.31 Graphs of the actual hip and knee joint angles (dotted line) compared to their decodification (solid line). These decodifications were performed with a time delay of 3.5 s. For each sub-figure from top to bottom: D1, D2, and D3. 84

4.32 100 array combinations represented in a binary table, using 19 electrodes, namely Fp1, Fp2, F3, F4, C3, C4, P3, P4, O1, O2, F7, F8, T3, T4, T5, T6, Cz, Fz, and Pz. 87

4.33 Normalized occurrence of each electrode of the best 10% of arrays considering the correlation coefficient (a & e), normalized root mean square error (b & f), and signal-to-noise ratio (c & g). The normalized occurrence of the electrodes combining the three metrics is depict in d & h. The first row of the image corresponds to Task 1 and the second row to Task 2. 89

4.34 Normalized occurrence between subjects of each combination of gaps and delay of the best 10% considering the correlation coefficient (a & e), normalized root mean square error (b & f), and signal-to-noise ratio (c & g). The normalized occurrence of the delay and gaps combinations mixing the three metrics is depicted in d & h. The first row of the image corresponds to Task 1 and the second row to Task 2. 90

4.35 Graph of the actual knee joint angle (blue dot line) compared to the segmented decodification without transformation functions (green dash-dot line) and with transformation functions (red solid line) for Subject 1 during Task 1. 97

4.36 Graph of the actual knee joint angle (blue dot line) compared to the segmented decodification without transformation functions (green dash-dot line) and with transformation functions (red solid line) for Subject 2 during Task 1. 97

4.37 Graph of the actual knee joint angle (blue dot line) compared to the segmented decodification without transformation functions (green dash-dot line) and with transformation functions (red solid line) for Subject 3 during Task 1. 98

4.38 Graph of the actual knee joint angle (blue dot line) compared to the segmented decodification without transformation functions (green dash-dot line) and with transformation functions (red solid line) for Subject 4 during Task 1. 98

4.39 Graph of the actual knee joint angle (blue dot line) compared to the segmented decodification without transformation functions (green dash-dot line) and with transformation functions (red solid line) for Subject 5 during Task 1. 99

4.40 Graph of the actual knee joint angle (blue dot line) compared to the segmented decodification without transformation functions (green dash-dot line) and with transformation functions (red solid line) for Subject 6 during Task 1. 99

4.41 Graph of the actual knee joint angle (blue dot line) compared to the segmented decodification without transformation functions (green dash-dot line) and with transformation functions (red solid line) for Subject 7 during Task 1. 100

4.42 Graph of the actual knee joint angle (blue dot line) compared to the segmented decodification without transformation functions (green dash-dot line) and with transformation functions (red solid line) for Subject 8 during Task 1. 100

4.43 Graph of the actual hip joint angle (blue dot line) compared to the segmented decodification without transformation functions (green dash-dot line) and with transformation functions (red solid line) for Subject 1 during Task 2. 101

4.44 Graph of the actual hip joint angle (blue dot line) compared to the segmented decodification without transformation functions (green dash-dot line) and with transformation functions (red solid line) for Subject 2 during Task 2. 101

4.45 Graph of the actual hip joint angle (blue dot line) compared to the segmented decodification without transformation functions (green dash-dot line) and with transformation functions (red solid line) for Subject 3 during Task 2. 102

4.46 Graph of the actual hip joint angle (blue dot line) compared to the segmented decodification without transformation functions (green dash-dot line) and with transformation functions (red solid line) for Subject 4 during Task 2. 102

4.47 Graph of the actual hip joint angle (blue dot line) compared to the segmented decodification without transformation functions (green dash-dot line) and with transformation functions (red solid line) for Subject 5 during Task 2. 103

4.48 Graph of the actual hip joint angle (blue dot line) compared to the segmented decodification without transformation functions (green dash-dot line) and with transformation functions (red solid line) for Subject 6 during Task 2. 103

4.49 Graph of the actual hip joint angle (blue dot line) compared to the segmented decodification without transformation functions (green dash-dot line) and with transformation functions (red solid line) for Subject 7 during Task 2. 104

4.50 Graph of the actual hip joint angle (blue dot line) compared to the segmented decodification without transformation functions (green dash-dot line) and with transformation functions (red solid line) for Subject 8 during Task 2. 104

A.1 Test subject wearing three spherical markers allocated on the right hip, knee and ankle, for video processing. 118

A.2 Illustrative sections for which a MLR was created. The same angles are displayed in order to illustrate the sections: (a) Decoder 1 (D1) where yellow corresponds to a single MLR for all activities, (b) Decoder 2 (D2) where blue corresponds to resting periods, and cyan to the movement period, (c) Decoder 3 (D3) where blue corresponds to resting periods, green for the raising and red for the lowering period. 120

A.3 Decodification of the knee angles using three decoders. From top to bottom: Decoder 1 (D1), Decoder 2 (D2), and Decoder 3 (D3). As illustrated in Figure A.2. 124

List of Tables

4.1 Combinations of sets with their respective electrode array and time delay. 61

4.2 Correlation coefficient (CC) values of the decodifications of the hip and knee angles for eight subjects and their mean and standard deviations for Tasks 1 and 2. D1, D2, and D3 stand for the decoder used. 66

4.3 Normalized root mean square error (NRMSE) values of the decodifications of the hip and knee angles for eight subjects and their mean and standard deviations for Tasks 1 and 2. D1, D2, and D3 stand for the decoder used. 67

4.4 Signal-to-noise ratio (SNR) values of the decodifications of the hip and knee angles for eight subjects and their mean and standard deviations for Tasks 1 and 2. D1, D2, and D3 stand for the decoder used. 68

4.5 Comparing the configurations of previously used parameters (Old) and the parametric adjustment (New) for the segmented decodifications. Task 1 values at the top and Task 2 values at the bottom of the table. CC and SNR values increase with the new configuration, while the NRMSE values decrease. 91

4.6 Values of the genetic representation and their respective transformation function. S_n represents the n-th electrode of the EEG signals. . . 93

4.7 Parameters chosen for the genetic algorithm. 94

4.8 Comparison of the segmented decodification with and without transformation function. The last column displays the chromosome of the best performance obtained by the GA using the NRMSE fitness value for the knee joint angle decodification during Task 1. Additionally, the metrics of CC and SNR are also displayed. 95

4.9 Comparison of the segmented decodification with and without transformation function. The last column displays the chromosome of the best performance obtained by the GA using the NRMSE fitness value for the hip joint angle decodification during Task 2. Additionally, the metrics of CC and SNR are also displayed. 96

4.10 Chromosome and its respective transformation functions of the subject with the best performance of the fitness value from Table 4.8. . . 96

4.11 Chromosome and its respective transformation functions of the subject with the best performance of the fitness value from Table 4.9. . . 96

A.1 Pearson correlation coefficient (CC) values of the decodifications of the hip and knee angles for nine subjects and their mean and standard deviations for trial types 1 and 2. D1-D3 stand for the decoder used. 121

A.2 Normalized root mean square error (NRMSE) values of the decodifications of the hip and knee angles for nine subjects and their mean and standard deviations for trial types 1 and 2. D1-D3 stand for the decoder used. 122

A.3 Signal-Noise Ratio (SNR) values of the decodifications of the hip and knee angles for nine subjects and their mean and standard deviations for trial types 1 and 2. D1-D3 stand for the decoder used. 123

ABSTRACT

ABSTRACT

Due to the prevalence of disabilities that affect the lower limbs in the growing population, it seems necessary to provide assistance to those that lost their ability to walk and grant means to those that lack such function. A brain-computer interface (BCI) is a useful technology that includes systems or devices that sense and respond to neural processes, allowing a disabled user to interact with any device by interpreting neurophysiological signals. BCI systems have been based on electroencephalography (EEG) which consists of sensing electrical signals from the brain using noninvasive sensors on the surface of the scalp. BCIs appear to be under two categories: the discrete classification of human tasks and the continuous trajectory reconstruction of kinematics or kinetics. This research consists on proving that it is possible to make a continuous trajectory reconstruction, also called decodification, from slow cortical potentials, i.e., low frequencies of the EEG signals. In this study, two types of lower limb mobility protocols are proposed: synchronous movements consisting in raising and lowering the foot or the knee within fixed time periods, and asynchronous movements consisting of self-paced continuous flexions and extensions of the knee in a given set of time.

The first approach presents evidence of the nonlinear characteristics of the EEG signals during synchronous lower limb mobility protocols. Whereas in the literature, it has only been reported the characterization of these signals between different mental states. To characterize the behavior of the EEG signal, the randomness, complexity, nonstationarity, and nonlinearity of the EEG were studied. Firstly, randomness is analyzed by the Hurst exponent, which also is used to characterize the nonstationary behavior of the EEG signals. In this thesis, the Hurst exponent values of the brain signal show a nonrandom persistent time series, when considering small time windows. The correlation dimension is used as a measure of the complexity of the system related to the number of degrees of freedom, and it is also used to distinguish between random, periodic, or chaotic behavior. The correlation dimension has shown that the underlying system of the brain can range in a relatively low number of dimensions. Finally, the largest Lyapunov exponent is used to confirm the presence of chaos in the underlying dynamics of the time series. In this thesis, the largest Lyapunov exponent values seem to be strictly positive, which is often considered as a definition of deterministic chaos. Implying that the underlying dynamics is indeed nonlinear. With these insights, we could define a nonarbitrary selection of a candidate model (e.g., computational model or neural network) to classify motion tasks and/or to resolve the continuous trajectory reconstruction of lower limb kinematics. This selection could provide reliable and affined methods for EEG-based BCI systems to manipulate assistive devices useful in neuromuscular rehabilitation.

The second approach presents additional evidence of decodification using slow cortical potentials. Different electrode arrays and time ranges were tested to compare performances of the reconstruction, proving certain electrodes contribute in greater amount than others to the decodification. The decodification of segmented signals for different types of tasks gave a better performance compared to using a single decoder for the entire signals. Finally, the usage of transformation functions to the EEG signals in order to later be used by the decoder proved there exists combinations of equations that give better results than using the EEG signal directly.

In summary, the approach to characterize the EEG signals gives information that can be useful for further studies regarding the mathematical modeling of neural activity during motor tasks. Whereas the second approach shows evidence of improvement for decodification of the kinematics from neural signals. Both results could be starting points to further improve the understanding of neuro-motor tasks and their application of artificial reproduction of movements from EEG signals through a BCI.

Resumen

Resumen

Debido a la prevalencia de las discapacidades que afectan los extremidades inferiores en la creciente población, parace necesario proveer asistencia a aquellas personas que perdieron la habilidad de caminar u otorgar medios para aquellos que no cuentan con esa función. Una interfaz cerebro-computadora (BCI, por sus siglas en inglés) es una herramienta tecnológica que incluye sistemas o dispositivos que sensan y responden a procesos neurales, permitiendo a un usuario discapacitado interactuar con cualquier dispositivo mediante la interpretación de sus señales neurofisiológicas. Los sistemas BCI han estado basados en la electroencefalografía (EEG) la cual consiste en sensar las señales electricas del cerebro usando sensores no invasivos en la superficie del cuero cabelludo. Las BCI parecen estar bajo dos categorias: la clasificación discreta de tareas humanas y la reconstrucción continua de trayectorias cinemáticas o cinéticas. Este trabajo consiste en demostrar que es posible realizar una reconstruccioón continua de trayectoria, también llamada decodificación, a partir de potenciales corticales lentos, i.e., bajas frecuencias de las señales EEG. En este estudio, dos tipos de protocolos de movilidad de los extremidades inferiores son presentados: movimientos síncronos que consisten en levantar y bajar el pie o la rodilla dentro de periodos de tiempo fijos, y movimientos asíncronos que consisten de flexiones y extensiones continuas de la rodilla a cierto ritmo en un tiempo determinado.

El primer enfoque presenta evidencia de las características no lineales de las señales EEG durante protocolos síncronos de movilidad de una extremidad inferior. Mientras que en la literatura sólo a sido reportada la caracterización de estas señales durante differentes estados mentales. Para caracterizar el comportamiento de la señal EEG, la aleatoriedad, complejidad, no estacionariedad y la no linealidad

de la EEG fueron estudiadas. En primer lugar, la aleatoriedad es analizada por el exponente de Hurst, el cual también es usado para caracterizar el comportamiento no estacionario de las señales EEG. En esta tesis, los valores del exponente de Hurst de la señal cerebral muestran que es una serie en el tiempo persistente no aleatoria, esto es cuando se consideran ventanas de tiempo pequeñas. La dimensión de correlación es usada como una medida de la complejidad del sistema relacionado con el número de grados de libertad, y también es usada para distinguir entre un comportamiento aleatorio, periodico o caótico. La dimensión de correlación ha mostrado que el sistema subyacente del cerebro puede oscilar en un número de dimensiones relativamente bajo. Finalmente, el exponente de Lyapunov mayor es usado para confirmar la presencia de caos en la dinámica subyacente de las series de tiempo. Los valores del exponente de Lyapunov aparentan ser estrictamente positivos, esto es frecuentemente considerado como una definición del caos determinista. Lo cual implica que la dinámica subyacente es ciertamente no lineal. Con estos conocimientos, podríamos definir una selección no arbitraria de un modelo candidato (e.g., modelo computacional o red neuronal) para clasificar tareas motrices y/o para resolver la recontrucción continua de trayectoria de la cinemática de una extremidad inferior. Esta selección podría proveer métodos fiables y afines para los sistemas BCI basados en EEG para manipular dispositivos de asistencia útiles en la rehabilitación neuromuscular.

El segundo enfoque presenta evidencia adicional de la decodificación usando potenciales corticales lentos. Diferentes conjuntos de electrodos y rangos de tiempo fueron probados para comparar los desempeños de la reconstrucción, demostrando que ciertos electrodos contribuyen en mayor medida que otros en la decodificación. La decodificación de las señales segmentadas para los diferentes tipos de tareas otorgaron un mejor desempeño comparado con usar un solo decodificador a las señales enteras. Finalmente, el uso de funciones de transformación a las señales EEG para después ser usadas por el decodificador demostraron que existen combinaciones de ecuaciones que dan mejores resultados que usar las señales EEG directamente.

En resumen, el enfoque de la caracterización de las señales EEG da información que puede ser de utilidad para estudios posteriores sobre el modelamiento matemático de la actividad neural durante actividades motrices. Mientras que el

segundo enfoque muestra evidencia de la mejora de la decodicación de la cinemática a partir de la señales neurales. Ambos resultados pueden ser puntos iniciales para mejorar el entendimiento de las funciones neuromotoras y su posterior aplicación de la reproducción artificial de movimientos a partir de las señales EEG a través de una BCI.

Chapter 1

Introduction

1.1 Motivation

According to the World Health Organization (WHO), over 15% of the population of the world has some kind of disability [1]. In 2011, in the European Union, there were 16,817,587 people with a walking disability, and 9,902,557 had difficulty of standing or sitting [2]. Just in the U.S. in 2014, around 39 million people had a disability associated with their ambulatory activities such as having difficulty walking, climbing stairs, or had the necessity of using a wheelchair, walker, cane, or crutches [3]. In a similar way, the most constant type of disability present in the Asia-Pacific region is a physical type, involving upper and lower limb limitations [4]. Lower limb disabilities can be caused by health conditions that belong to broad categories such as congenital anomalies, chronic conditions, or injuries. Congenital anomalies affect an estimated 1 in 33 infants and result in approximately 3.2 million birth defect-related disabilities every year [5]. In the U.S., 1 in 2858 births have spina bifida, which includes leg weakness, or paralysis. Also, musculoskeletal defects in the lower limbs are estimated to be 701 cases each year [6]. The impairment in motor or sensory function of the lower extremities, called Paraplegia, is caused by spinal cord injury (SCI). Every year, around the world, between 250,000 and 500,000 people suffer a spinal cord injury, that may result from trauma, disease, or degeneration (cancer). There is no reliable estimate of global prevalence, but estimated annual global incidence is 40 to 80 cases per million population. Up to 90% of these cases are due to traumatic causes, though the proportion of nontraumatic spinal cord injury appears to be growing [7]. Annually, 15 million people worldwide suffer a stroke. Of these, 5 million die and another 5 million are left permanently disabled [8]. According to the Encuesta Nacional de Salud y Nutrición (ENSANUT) 2012 in Mexico, around 4.9% of male and 5.8% of female population (around 2.5 and 3 million respectively) had the disability of walking or movement [9]. Briefing all these global statistics, it can be seen that lower limb disabilities are prevalent, thus it comes as a challenge to assist this disabled growing population.

The WHO defines congenital anomalies, also known as birth defects, as structural or functional anomalies, including metabolic disorders, which are present at the time of birth [5]. The before mentioned congenital anomaly of spina bifida, more accurately referred to as myelomeningocele, is a defect of primary neurulation that results from failure of fusion in the caudal region of the neural tube [10]. According to the Centers for Disease Control and Prevention (CDC), myelomeningocele is the most serious type of spina bifida. With this condition, a sac of fluid comes through an opening in the back of the baby. Part of the spinal cord and nerves are in this sac and are damaged. This type of spina bifida causes moderate to severe disabilities, loss of feeling in the legs or feet, and inability to move the legs [11]. Regarding musculoskeletal disabilities, lower limb reduction defects occur when a part of or the entire leg (lower limb) of a fetus fails to form completely during pregnancy. The defect is referred to as a limb reduction because a limb is reduced from its normal size or in some cases the limb is entirely missing. The cause of limb reduction defects is unknown. However, research has shown that certain behaviors or exposures during pregnancy can increase the risk of having a baby with a limb reduction defect [12]. According to the WHO, symptoms of spinal cord injury depend on the severity of injury and its location on the spinal cord. Symptoms may include partial or complete loss of sensory function or motor control of arms, legs, and/or body. The most severe spinal cord injury affects the systems that regulate bowel or bladder control, breathing, heart rate, and blood pressure. Most people with spinal cord injury experience chronic pain [7]. The WHO also mentions that stroke is caused by the interruption of the blood supply to the brain, usually because a blood vessel bursts or is blocked by a clot. This cuts off the supply of oxygen and nutrients, causing damage to the brain tissue. The most common symptom of a stroke is sudden weakness or numbness of the face, arm, or leg, most often on one side of the body. Other symptoms include: difficulty walking, dizziness, loss of balance or coordination, severe headache with no known cause, fainting or unconsciousness. The effects of a stroke depend on which part of the brain is injured and how severely it is affected. A very severe stroke can cause sudden death [13]. Due to the prevalence of disabilities that affect the lower limbs in the growing population, it seems necessary to provide assistance to those that lost their ability to walk and grant means to those that lack said ability.

According to the CDC, people with spina bifida on the upper part of the spine (near the head) might have paralyzed legs and use wheelchairs. Those with spina bifida on the lower part of the spine (near the hips) might have more use of their legs and use crutches, braces, or walkers, or they might be able to walk without these devices [14]. The goal for treatment of limb reduction defects is to provide a limb that has proper function and appearance. Treatment may include the usage of prosthetics, orthotics, or rehabilitation (physical therapy). Treatments to address SCI focus on restoring some degree of walking or locomotor activity, using techniques like treadmill training, overground training, or functional electrical stimulation [15]. In a similar way, gait recovery is a major objective in the rehabilitation program for stroke patients [16]. Although some of the current methods, procedures, or techniques used for lower limb disabled people have good results, most consist on prolonged periods of time in rehabilitation, or have a degree of discomfort to the user.

In order to provide the lower limb disabled people with a mean to restore the mobility they once had, without the extensive or uncomfortable treatments, the cyber physical systems (CPS) research community has shown great interest in the integration of both cyber systems and biomedical systems. The typical CPS are known as brain-machine interfaces (BMI), also called brain-computer interfaces (BCI). BMI are useful technologies that include systems or devices that sense and respond to neural processes, allowing a disabled user to interact with any device by interpreting neurophysiological signals. The signals acquired by the BMI systems tend to control an external device, like a computer cursor, an internet browser, an exoskeleton, or prosthesis. BMI systems have been based on electroencephalography (EEG) which consists of sensing electrical signals from the brain using noninvasive sensors on the surface of the scalp. An EEG signal is a measurement of currents from many neurons in the cerebral cortex, which generate an electrical field over the scalp measurable by an array of electrodes. The amplitudes and frequencies of such signals include information about the state and change of the neural activity, and reflect the dynamics of electrical activity of the brain. On the scalp, these amplitudes commonly lie within $10 - 100$ μV, and the different frequency ranges are distinguished by brain waves, called (from low to high frequencies): delta (δ), theta (θ), alpha (α), beta (β), and gamma (γ) [17]. The electrical discharge that the sensors record possess relevant information of the brain signal. This signal can also be acquired with invasive sensors, such as intracortical microelectrodes or electrocorticography (ECoG). However, these types of approaches have certain risk of brain injury; this is because there is the disadvantage of requiring a surgery to allocate the electrodes in the brain. Although data acquired noninvasively via EEG has low signal-to-noise ratio and spatial resolution [18, 19, 20], it is easier to repair or replace an EEG interface.

EEG signals tend to help in computer aided diagnosis (CAD) by characterizing between brain states, ranging from healthy, pathological or induced: predicting seizures, classifying sleep stages, depth of anesthesia, Alzheimer, memory impairments, coma, emotional states, depression, schizophrenia, cognition, dementia [21]. For example, Acharya et al. [22] reported that linear and nonlinear methods have been applied to identify the changes in EEG signals in order to detect depression. However, their focus was primarily on the nonlinear methods of higher order spectra and recurrence quantification analysis. Ibrahim et al. [23] listed some of the EEG signal processing and feature extraction methods used for aiding diagnosis of epilepsy. This includes linear methods on time domain, frequency domain, and some studies using the time-frequency domain, as well as nonlinear methods including entropy, largest Lyapunov exponent and others. In particular, they used a combination of discrete wavelet transform and Shannon entropy as features for a feed-forward neural network which classified epilepsy states. Aldea et al. [24] focus on using some of the mentioned nonlinear methods applied to EEG signals to compare between healthy subjects, epileptic subjects, and subjects with Parkinson disease. The focus in [24] was on methods of the nonlinear dynamics like: largest Lyapunov exponent, correlation dimension and Hurst exponent, after using a wavelet transform on the EEG signal.

EEG-based BMI systems are applied to treat a wide variety of motor disorders like amyotrophic lateral sclerosis, stroke, or SCI. There are many studies worldwide exploring this field. For example, Yu et al. [25] presented a brain controlled lower extremity exoskeleton rehabilitation robot where left and right hand motor imagery movements were classified in order to control the speed of the gait. In their work, power spectral density was used to extract features from the EEG, and the classifiers used were linear discriminant analysis and random forest algorithm. On the approach taken by Sayed et al. [26], the features of the motor imagery tasks were obtained from the nonlinear methods of affine-invariant moments and distance series transform from the state space trajectory. Such features were then used on different classifiers including the K-nearest neighbor, support vector machines, linear discriminant analysis, and quadratic discriminant analysis. He et al. [27] focused on stroke neurorehabilitation, utilizing the X1, which is a powered robotic lower limb exoskeleton from the NASA. That BMI consisted in applying principal component analysis to the EEG signal to reduce the dimensionality and then using a 10th order unscented Kalman filter, all these in order to decode lower limb joint kinematics during walking. Their work showed preliminary evidence of integrating an EEG-based BMI with a lower limb robotic exoskeleton.

Recently He et al. 2018 [28] presented a review where studies of BMI were used to control lower limb robotic systems. In that review, two categories were mentioned: the discrete classification and the continuous trajectory reconstruction. Such literature showed that discrete classification has been widely addressed to classify between walk versus stand tasks commonly using the EEG method. As examples, the works of Do et al. 2013 [29], Kilicarslan et al. 2013 [30], Kwak et al. 2015 [31], García-Cossio et al. 2015 [32], López-Larraz et al. 2016 [33], Donati et al. 2016 [34], Lee et al. 2017 [35], and Zhang et al. 2017 [36] can be highlighted. The main focus of these studies is in the classification of the brain signals during idling and walking. With this, it can be seen that the BMI is subject to the activation of those specific activities. The results provided evidence that ambulation using brain signals is possible. These studies of discrete classification have outnumbered the studies of the category of continuous trajectory reconstruction on the review of He et al. [28]. There, only two studies landed in this category, and only one was performed on humans, He et al. 2014 [27]. That study showed the feasibility of decoding lower limb joint kinematics and kinetics during walking using an exoskeleton as a potential diagnostic, assistive, and therapeutic tool for stroke rehabilitation.

1.2 Problem Description

Many studies using EEG when implementing a BMI (or BCI) tend to use the discrete classification approach, which starts by recording the mental task of a subject. The recorded signals pass through a preprocessing, followed by the extraction of features that have characteristics of the brain signal. Then these features are discriminated using a classification (pattern recognition). Finally, the identified signal is associated with an action performed by the external device or computer. Several studies of EEG signals have succeeded in classifying the movement intention in lower limb motor tasks [37], generally using linear methods for the classification, like linear discriminant analysis and support vector machines. However, the discrete classification methods tend to have difficulty in increasing the number of classes, thus having a limited number of tasks to be classified [28]. As the intent is detected by the BMI or BCI, the system should execute realistic movements according to the mental process of the user, as if no disability was present. For this reason, a continuous trajectory reconstruction from the EEG signals into the limb kinematics is desired, instead of a limited number of classes of movements. Many techniques have been used for the continuous trajectory reconstruction approach [38], including Wiener filters, Kalman filters, particle filters, and artificial neural networks. In the literature, the nature of the EEG signals is considered nonlinear, thus the nonlinear methods probably lead to a better performance than the widely used conventional linear methods, since they could not forecast brain behavior [39, 40]. There is a limited number of studies that reconstruct the trajectories from the EEG signals into lower limb kinematics [27, 41, 42, 43], and mostly linear methods are applied. When a nonlinear method is used, its parameters are commonly arbitrarily selected. The mentioned studies show results of the continuous trajectory reconstruction of the lower limb kinematics obtained with the protocol of actual walking. However, although the performances are considered to be relatively high or acceptable, this could be further improve. Moreover, the walking protocol, i.e., the gait, is considered a periodic trajectory since most of these studies performed the gait in treadmills. Thus it comes to interest to reconstruct the continuous kinematics under a set of different movements. For this reason, two types of lower limb mobility protocols are proposed: (i) to perform synchronous movements consisting in raising and lowering the foot or the knee within fixed time periods, and (ii) to perform asynchronous movements consisting of a continuous movement of the knee freely in a set of time. It also comes to interest to analyze the nonlinear features of the EEG signals in order to propose feature-based methods that improve the solution of continuous trajectory reconstruction problems.

1.3 Hypothesis

The hypothesis of this research is that the continuous trajectory reconstruction (from here on called decodification) of the kinematics can be obtained from slow cortical potentials, i.e., low frequencies of the EEG signals, during protocols of synchronous lower limb movements.

1.4 Objectives

1.4.1 Main Objective

To decode lower limb kinematic variables from neural signals using EEG signals acquired during lower limb mobility protocols.

1.4.2 Particular Objectives

1. To obtain a data base of neural and kinematic signals during lower limb mobility protocols.
2. To analyze nonlinear characteristics to understand the neural signal.

3. To compare different EEG electrode arrays and time ranges for the decoding of the signals.

4. Compare different decoding procedures to select the more reliable one for the desired decoding during lower limb mobility protocols.

1.5 Thesis Contribution

The following contributions have been achieved by the development of this thesis:

- This thesis presents evidence of the nonlinear characteristics of the EEG signals during synchronous lower limb mobility protocols. Whereas in the literature, it has only been reported the characterization of these signals between different mental states. Particularly, the evidence of the nonlinear characteristics consists of:
  1. The Hurst exponent values of the brain signal show a nonrandom persistent time series, when considering small time windows.
  2. The correlation dimension has shown that the underlying system of the brain can range in a relatively low number of dimensions.
  3. The largest Lyapunov exponent values seem to be strictly positive, which suggests that the dynamics of the brain signal is nonlinear, this is based on the premise that a linear system with a positive LLE implies unstable trajectories, and also based in the fact that the brain signals are bounded.

- This thesis presents the methodology and additional evidence of decodification with slow cortical potentials, which consists of:
  1. Different electrode arrays, time ranges, and number of used samples were tested to compared performances of the reconstruction, proving certain electrodes contribute in greater amount than others to the decodification.
  2. The decodification of segmented signals for the different types of tasks gave a better performance compared to using a single decoder for the entire signals.

3. The usage of transformation functions to the EEG signals in order to later be used by the decoder proved there exists combinations of equations that give better results than using the EEG signal directly.

CHAPTER 2

METHODS

The methods applied in order to fulfill the objectives are described in this chapter, which cover the nonlinear characterization of the EEG signal, the decoding of the EEG signals into kinematic values, and a genetic algorithm used to perform an optimization of the decodification.

2.1 RANDOMNESS & NONLINEAR DYNAMICAL ANALYSIS

It has been reported that nonlinear features are capable of capturing the complex physiological phenomena of the EEG signal such as chaotic behavior or abrupt transitions in the time series [44]. To carry out the analysis of the EEG signal, in this thesis the randomness, complexity, and nonlinearity of the EEG signal during lower limb motion tasks were studied. Firstly, randomness is analyzed by the Hurst exponent (H), also H is used to characterize the nonstationary behavior of the EEG signals [45]. After that, the correlation dimension (CD) is used as a measure of the complexity of the system related to the number of degrees of freedom, also CD is used to distinguish between random, periodic, or chaotic behavior [46, 45]. Finally, the largest Lyapunov exponent (LLE) is used to confirm the presence of chaos in the underlying dynamics of the time series; furthermore, the positiveness of LLE is a necessary (but not sufficient) condition of chaos. In fact, according to Scarlat et al. [47] if a time series exhibits an irregular pattern, nonlinear dependence, low estimate of CD, and positive estimate of LLE, then the underlying system possesses chaotic dynamics. The selected methods and a description are given next.

2.1.1 HURST EXPONENT

Hydrologist Harold Edwin Hurst developed a statistical methodology for distinguishing random from non-random systems and to identify the persistence of trends, known as rescaled range analysis or R/S analysis. However, Benoit Mandelbrot recognized the potential of such methodology to be applied in fractal geometry. In Hurst's honor, H is used as a measure to evaluate self-similarity, autocorrelation, predictability, and the degree of presence or absence of long-range dependence in a time series [48]. H relates to the rate at which these evaluations decrease as the lag between pairs of values increases. It is also a measure of the smoothness of a fractal time-series based on the asymptotic behavior of the rescaled range of the process [46].

In time series analysis of EEG, H is usually used to characterize the nonstationary behaviour [49]. For example, Natarajan et al. 2004 [45] obtained H values that indicated that the randomness or the disorderliness of the EEG decreased after music/reflexologic stimulation. Kannathal et al. 2005 [50] showed that there is a negative correlation between the values of CD and H between a control group and an epileptic group. Also a comparison between a control group and an alcoholic group showed that, the former group has a value closer to being random. Acharya et al. 2005 [51] analyzed EEG signals during different sleep stages with the self-similarity parameter of H. They showed that the value gradually decreases from the sleep stage 0 (awake) to stage 1. Then it had a maximum value in sleep stage 2, from which it decreased in the stages 3 and 4. Finally, they observed an increase on sleep stage 5 (REM, rapid eye movement sleep). These studies, show that the H value, can determine if the EEG time series have a random or non-random behavior under different brain conditions.

The Hurst exponent rather than calculated, it is estimated. To estimate H, one must first regress, or estimate the dependence of the rescaled range on the time span of observation. To do this, a time series of full length N is divided into A segments of shorter length n, so that $A \cdot n = N$. Each segment is defined as w_a for $a = 1, 2, ..., A$, where there are $X_{k,a}$ elements for $k = 1, 2, ..., n$. The rescaled range is calculated, for each of the A smaller time series, as follows:

1. Calculate the mean of the a segment of length n:
$$m_a = \frac{1}{n}\sum_{k=1}^{n} X_{k,a}. \tag{2.1}$$
2. Calculate the cumulative deviate series Z from the mean-adjusted series as
$$Z_{k,a} = \sum_{i=1}^{k}(X_{k,a} - m_a), \quad k = 1, 2, ..., n. \tag{2.2}$$
3. The range R_a is defined as the difference between the maximum and minimum values of $X_{k,a}$ for each a segment:
$$R_a = \max\{X_{k,a}\} - \min\{X_{k,a}\}, \quad \text{where } 1 \leq k \leq n. \tag{2.3}$$
4. For each segment the standard deviation is calculated by
$$S_a = \sqrt{\frac{1}{n}\sum_{k=1}^{n}(X_{k,a} - m_a)^2}. \tag{2.4}$$
5. For each segment, the range R_a is divided by the corresponding standard deviation S_a to calculate the rescaled range R_a/S_a [52].

After all the segments have their rescaled range, an average over all the partial time series is performed. H is estimated by fitting the power law $E[R_a/S_a] = Cn^H$ to the data. This estimation can be done by plotting $\log[R_a/S_a]$ as a function of $\log n$, and fitting a straight line, where the slope of the line gives the H value. The Hurst exponent is able to classify time series into types and provide some insight into their dynamics [48]. Depending of the value taken by H, the time series can be classified as the following types:

- **Random series:** If $H = 0.5$, the behavior of the time series is completely random, and it indicates the absence of correlation between the increments of the signal, as seen in the top part of Figure 2.1.

- **Anti-persistent time series:** When $0 < H < 0.5$, indicates of anti-persistent or anti-correlated behavior and the closer the value is to 0, the stronger is the tendency for the time series to revert to its long-term means value. In this type of behavior, an increase will most likely be followed by a decrease or vice-versa, as visualized in Figure 2.1.

- **Persistent time series:** If $0.5 < H < 1$, the time series shows a persistent or correlated process, the larger the H value the stronger the trend, i.e., an increase in values will most likely be followed by an increase in the short term and a decrease in values will most likely be followed by another decrease in the short term, as seen in the bottom part of Figure 2.1.

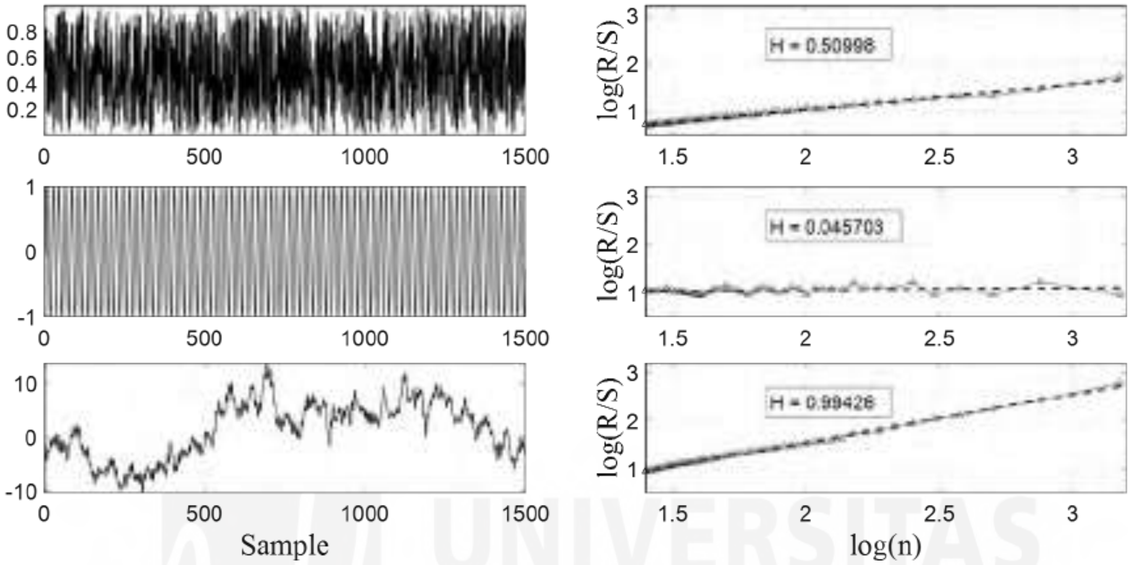

Figure 2.1: Different types of time series with their respective *log* plotting, and the estimated H values. Top: random series with an estimated H value close to 0.5; middle: anti-persistent time series (sine wave) with an H value close to 0; bottom: persistent time series (EEG) with an H value close to 1.

To emphasize the random or nonrandom behavior of the time series, and the stationarity or nonstationarity, statistics (mean and standard deviation) of the studied signal are calculated. In order to do so, the mean $\bar{x}$ is considered as the sum of the sampled values divided by the number of samples, as given by

$$\bar{x} = \frac{1}{n}\sum_{i=1}^{n} x_i = \frac{x_1 + x_2 + ... + x_n}{n}, \tag{2.5}$$

where x_i are the samples and n is the number of samples. The standard deviation, i.e., the square root of the sample variance, which is the average of the squared deviations about the sample mean, is given by the following:

$$\sigma = \sqrt{\frac{1}{n}\sum_{i=1}^{n}(x_i - \bar{x})^2}. \tag{2.6}$$

In a stationary process, parameters such as the mean and variance (the square of the standard deviation) do not change over time. Generally, for the EEG signals during mental and physical activities, the mean and standard deviation change from one segment to the next, thus considering the signal nonstationary. However, during normal brain condition, the EEG is considered stationary only withing short intervals, i.e., quasistationary [17].

2.1.2 CORRELATION DIMENSION

In mathemathics, a set with space filling properties is usually quantified by dimension measurements. Such set can be embedded in an abstract mathematical space or a real space, which also has an associated dimension. According to Camastra et al. 2003 [53], there are many kinds of dimensions, e.g., the topological dimension of a point is 0, and a volume has dimension 3. It is important to note that the topological dimensions are always integers. Fractal dimensions, on the contrary, consider noninteger dimensional values. Nontrivial and simple examples of fractal dimensions are a wiggly line or curve between any two points. These lines intuitively fill up more space than a smooth line, but still do not fill up enough space to be considered a surface (dimension 2). However, all three compared lines have a topological dimension of 1. The former lines are deemed fractal if their fractal dimension is greater than their topological dimension [54]. To measure this fractal dimension in nonlinear dynamics time series, the simplest dimension measurement to perform is the CD, assessed with the Grassberger-Procaccia algorithm [55]. In nonlinear dynamics, the time evolution of the system cannot be often obtained as a closed formula but it can be represented as a path in an abstract mathematical space called phase space. By using a process called phase space embedding, it is possible to reconstruct the path that shares the same invariant properties as the phase space trajectory. This process can be done by using just one time series component of the system. Usually phase space trajectories of deterministic dynamical systems tend to evolve towards a particular set of coordinates called an attractor and the dimension of the attractor is less than that of the full phase space [56].

Most applications of the CD on nonlinear analysis to electrophysiological time series have been to stationary time series such as an extended EEG or steady-state response [56]. For example, Natarajan et al. 2004 [45] estimated the correlation dimension of EEG data sets recorded for various mental states. They found that the EEG signal becomes less complex when the person is subjected to music of his/her choice or under reflexological stimulation, compared to a normal resting state. Kannathal et al. 2005 [50], by the calculation of CD, encountered that such value is lower during an epileptic activity compared to a nonepilectic one. They also found that an EEG of an alcoholic subject exhibits more complexity than that of an epileptic EEG, indicated by the correlation dimension values. Acharya et al. 2005 [51] quantified the cortical function at different sleep stages, tabulating that CD decreases from the sleep stage 0 (awake) to the stages 1-4, and then the value increases during the stage 5 (REM). With these studies, it can be seen that the use of CD to evaluate transitory responses has been less explored [56].

The correlation dimension is a nonlinear parameter frequently used to measure the dimensionality of a underlying process in relation to its geometrical reconstruction in phase space. The calculation of CD is based on the correlation integral, which is the probability that any two randomly chosen points on the attractor are closer together than a given distance r. The correlation integral function is calculated as

$$C(r) = \frac{1}{N^2} \sum_{x=1}^{N} \sum_{y=1, x \neq y}^{N} \Theta(r - |X_x - X_y|), \tag{2.7}$$

where r is the radial distance around each reference point, $C(r)$ is the correlation integral, X_x and X_y are points of the trajectory in the phase space, N is the number of data points in phase space, and Θ is the Heaviside function, $\Theta(x) = 0$ if $x \leq 0$ and $\Theta(x) = 1$ if $x > 0$. The integral (2.7) just considers the total number of pairs of points which have a distance between them that is less than distance r. As the number of points tends to infinity ($N \to \infty$), and the distance between them tends to zero ($r \to 0$), the correlation integral takes the form of $C(r) \sim r^{\mathrm{CD}}$, where a log-log graph of the $C(r)$ versus r gives an estimate of CD. Thus, CD is then calculated using the fundamental definition:

$$\mathrm{CD} = \lim_{r \to 0} \frac{\log C(r)}{\log(r)}. \tag{2.8}$$

The correlation dimension, as a quantitative parameter, is a measure of the complexity of the dynamical system related to the number of degrees of freedom. Computing

CD, by distinguishing its convergence, the system can be understood as random, periodic, or chaotic [45, 46]. CD does not converge in the case of a random signal. However, it converges to finite values for periodic or deterministic systems [46].

2.1.3 LARGEST LYAPUNOV EXPONENT

In mathematics, the Lyapunov exponent of a dynamical system quantifies the sensitivity to initial conditions by characterizing the rate of separation of infinitesimally close trajectories. Quantitatively, two trajectories in phase space with initial conditions separated $L(k_0)$ diverge or converge at a rate given by

$$|L(k)| \approx e^{\lambda k}|L(k_0)|, \tag{2.9}$$

where λ is the Lyapunov exponent, $L(\cdot)$ denotes the distance between trajectories at iteration k, and k_0 stands as the initial point. This rate of separation can differ depending of the initial separation vector. For this reason, there is a spectrum of Lyapunov exponents equal in number to the dimensionality of the phase space. However, it is common to refer to LLE, because it gives a notion of predictability for a dynamical system. λ is useful for distinguishing among the various types of orbits and it works for discrete as well as continuous systems. The signs of the exponents, in general, provide a qualitative picture of the dynamics of the system, where the movement of the orbits can be of the next types [57]:

- $\lambda < 0$: A negative exponent implies a stable periodic orbit or that the orbit attracts to a stable fixed point. These types of exponents are characteristic of dissipative or non-conservative systems, which exhibit asymptotic stability. In some cases, the more negative the exponent the greater the stability. For instance, when $\lambda \sim -\infty$ it is considered as a superstable fixed point or superstable periodic point.

- $\lambda = 0$: In this case, the value of zero stands for a marginally stable orbit, i.e., the orbit is a neutral or an eventually fixed point. A value of zero indicates that the system is in a steady state mode, which means is a conservative system exhibiting Lyapunov stability.

- $\lambda > 0$: The orbit is unstable and probably chaotic. In this case, there is no order to the orbit that ensues, i.e., nearby points will diverge to any arbitrary separation, eventually visiting all neighborhoods in the phase space.

To indicate the long-term behavior of the EEG time series, some studies have applied the LLE to quantify the predictability of the signal. Natarajan et al. 2004 [45], stated that a LLE value closer to one indicated a chaotic behavior of the time series, and that the value fell due to the influence of the music and reflexological stimulation. Kannathal et al. 2005 [50] with the LLE value, found that the value drops on alcoholic EEG compared to a control group. Acharya et al. 2005 [51] showed that the LLE value increased for sleep stage 3 and 5 due to the more variation involved as compared to the other states. These studies showed that, in general, the EEG under different mental or brain conditions present a rate of divergence. EEG just decreases in rate but never achieves a complete stability.

Generally, Lyapunov exponents can be extracted using two different ways. The first method is based on the estimation of local Jacobi matrices from the mathematical model of the dynamical system and is capable of estimating all the Lyapunov exponents. The second method is based on the idea of following the time evolution of nearby points of a time series. This last method provides only an estimation of the LLE, which as mentioned before gives a notion of predictability for the dynamical system.

The algorithm proposed by Wolf et al. [58] allows to determine the LLE from a time series and has the following approach: a point on the attractor is reconstructed by

$$\{x(k), x(k+\tau), ..., x(k+(m-1)\tau)\}, \quad \text{for} \quad k = 0, 1, 2, ..., M \tag{2.10}$$

where x is the time series with an m-dimensional phase portrait and a delay coordinate τ, and M is the total number of replacement steps. Then, the nearest neighbor to the initial point is located at

$$\{x(k_0), x(k_0+\tau), ..., x(k_0+(m-1)\tau)\}. \tag{2.11}$$

This procedure is repeated until the fiducial trajectory has traversed the entire time series, then the mean exponential rate of divergence of two initially close orbits is estimated through the following:

$$\mathrm{LLE} = \frac{1}{k_M - k_0} \sum_{l=1}^{M} \log_2 \frac{L'(k_l)}{L(k_{l-1})}, \tag{2.12}$$

where the distance between two reconstructed points is $L(k_0)$. At a later time k_1, initial distance evolves to distance $L'(k_1)$. A new data point is searched that satisfies two criteria reasonably well: its separation, $L(k_1)$, from the evolved fiducial point is small, and the angular separation between the evolved and replacement elements is small (Figure 2.2).

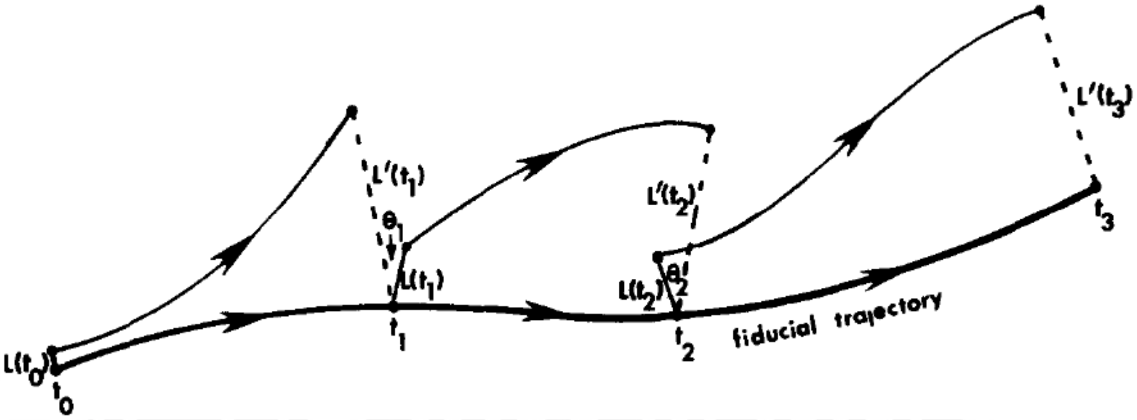

Figure 2.2: A schematic representation of the evolution and replacement procedure used to estimate Lyapunov exponents from experimental data. The largest Lyapunov exponent is computed from the growth of length elements. When the length of the vector between two points becomes large, a new point is chosen near the reference trajectory, minimizing both the replacement length L and the orientation change θ (Text and image taken from [56]).

The three methods described in this section are mainly used in order to study the randomness, complexity, and nonlinearity of the EEG signals. Randomness is analyzed by H [59], which also can characterize the nonstationarity behavior of EEG signals [45]. The complexity of the system is related to the number of degrees of freedom, and it can be measured with CD, which is also able to distinguish between random, periodic, or chaotic behavior [46, 45]. The LLE can confirm the presence of chaos in the underlying dynamics of a time series. Furthermore, its positiveness is a necessary but not a sufficient condition of chaos. It has to be taken in consideration that, according to Scarlat et al. [47], if a time series exhibits an irregular pattern, nonlinear dependence, low estimate of CD, and positive estimate of LLE, then the underlying system possesses chaotic dynamics. The set of indices these methods provide are expected to give insight of the underlying dynamics of the EEG signals during lower limb motor tasks. Such insights might give discernment for the construction or usage of a proper method applied to the decodification of the lower limb kinematics.

2.2 Decodification

As mentioned at the end of Section 1.1, He et al. 2018 [28] stated two categories of decodification: the continuous trajectory reconstruction and the discrete classification of tasks. However, such review was mainly focus on lower limb powered robotics systems such as exoskeletons and orthoses enhanced by BMIs. Furthermore, the outputs of the BMIs can be grouped according to their level of control. As claimed in their review, the highest and medium levels of control belong to the discrete classisifaction category, and the lowest level of control belongs to the continuous trajectory reconstruction category. The only reported study under that category in the review that involved humans was He et al. 2014 [27], which reconstructed joint angles and electromyography (EMG) envelopes of the lower limbs. Nevertheless, the reason behind the inclusion of just one study is due to the criteria taken in the review. If the criteria is reduced, the number of studies that perform a decodification by a continuous trajectory reconstruction increases. For example, the review mentions the study of Luu et al. 2017 [60], which adapted the method of He et al. 2014 [27], to control a virtual avatar on a screen in real time. Similar to the study of Luu et al. [60], other studies solely focus on the decodification of the EEG signal, i.e., the analysis of the signals without the need of a powered robotic system.

Fitzsimmons et al. 2009 [20] were the first to prove that linear decoders could reconstruct lower limb trajectories based on intracortical recording in nonhuman primates. Where 80 experimental records (10-15 min) were split in two halves used for both training and testing. Pressaco et al. 2011 [42] also showed that neural decoding could be performed with linear decoders to the locomotion in humans using noninvasive EEG signals. Where 5 min data records were divided in five segments, with multiple combinations of four segments for training and one segment for testing. Pressaco et al. 2012 [61] extended their study, with the decoding of both legs during locomotion. Using the same procedure as their previous work. Úbeda et al. 2014 [41] also applied linear decoders to EEG signals, but only focusing on the knee angle. Furthermore, different walking speeds were considered. Fold cross-validation was used depending on the number of runs performed by each subject. These mentioned studies focused on the task of locomotion. However, Úbeda et al. 2015 [62] proposed single joint movements in order to decrease the noise provoked by the gait. The works of Fitzsimmons et al. 2009 [20] and Pressaco et al. 2011, 2012 [42, 61] used the Wiener filter as the chosen linear decoder. This filter has been used in many studies of BMI because of its relative simplicity and efficacy. In some studies it takes the given name Wiener filter (see, e.g., [63, 64, 65, 66]). However, some studies call the used algorithm multiple (or multidimensional) lineal regression (see, e.g., [19, 62, 67, 68, 69, 70, 71, 72, 73]). The description of these algorithms and their similarities are explained next.

2.2.1 Linear optimum filter

Consider the block diagram of Figure 2.3 built around a linear discrete-time filter [74]

$$y(n) = \sum_{l=0}^{L-1} w_l x(n-l), \tag{2.13}$$

where the input of the filter consists of a time series $x(n)$ at some discrete time n, and the filter is itself characterized by the finite impulse response (FIR) w of length L. The output of the filter is denoted $y(n)$, and it can be corrupted by an additive measurement noise or estimation errors $e(n)$, leading to a linear regression model for the observed output or desired response

$$d(n) = y(n) + e(n) = \sum_{l=0}^{L-1} w_l x(n-l) + e(n). \tag{2.14}$$

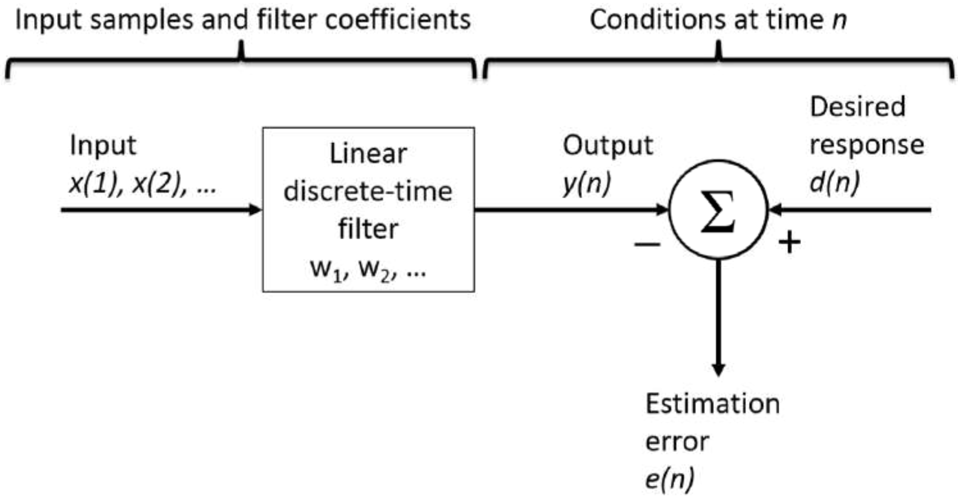
Input samples and filter coefficients
Conditions at time *n*
Input
x(1), x(2), ...
Linear discrete-time filter
$w_1, w_2, \ldots$
Output
y(n)
Desired response
d(n)
Σ
−
+
Estimation error
e(n)

Figure 2.3: Block diagram representation of the statistical filtering problem (modified from [74]).

This linear regression model can also be used even if the input-output relation of the given data pairs $[x(n), d(n)]$ is nonlinear, with w being the linear approximation to the actual relation between the data pairs. In that case, in $e(n)$ there would be a component associated to the additive noise perturbations, but also another one representing errors. In the context of (2.14), w can be seen as a quantity to be estimated by a linear filter, with (2.13) giving the output of the filter. This output is still considered as an estimate of the reference signal $d(n)$ or the output $y(n)$. Therefore, the problem of optimal filtering is analogous to the one of linear estimation [75].

The estimation error $e(n)$ is defined as the difference between the desired response $d(n)$ and the estimation of the filter $y(n)$, as seen in

$$e(n) = d(n) - y(n). \tag{2.15}$$

The requirement is to make the estimation error $e(n)$ as minimum as possible with a statistical criterion, cost function, or index of performance [74]. Some common optimization criteria in the literature are: least squares, minimum mean square error (MMSE), least absolute sum, minimum mean absolute error, and least mean fourth. Particularly, the MMSE criterion results in a second order dependence for the cost function on the unknown coefficients in the impulse response of the filter. In addition, the cost function has a distinct minimum that uniquely defines the optimum statistical design of the filter [74]. The mean square error (MSE) is defined by

$$\epsilon = E\left[|e(n)|^2\right] = E\left[|d(n) - y(n)|^2\right], \tag{2.16}$$

where $E[\cdot]$ is the expected value, and if this criterion is selected, the optimal solution to the linear estimation problem can be presented as

$$w_{opt} = \arg\min_{w} \epsilon. \tag{2.17}$$

As (2.16) is in a quadratic form, the optimal solution will be at the point where the cost function has zero gradient, i.e.,

$$\nabla_w \epsilon = \frac{\partial \epsilon}{\partial w} = 0. \tag{2.18}$$

Using (2.13) to expand (2.16), the gradient can be calculated as

$$\frac{\partial \epsilon}{\partial w} = E\left[2\underbrace{\left|d(n) - \sum_{l=0}^{L-1} w_l x(n-l)\right|}_{e(n)} x(n-l)\right] = 0. \tag{2.19}$$

From (2.19), given the signals $x(n)$ and $d(n)$, the latter can be assume to be generated by the linear regression model (2.14). In order to do this assumption, the system w would have to be equal to the optimal filter w_{opt}, in which the residual error $e(n)$ has to be uncorrelated to the input $x(n)$ [75]. Therefore (2.19) implies that

$$E\{e(n)x(n-l)\} = 0, \text{ for } l = 0, 1, ..., L-1. \tag{2.20}$$

This is called the *principle of orthogonality*, and it implies that the optimal condition is achieved if and only if the error $e(n)$ is decorrelated from the samples $x(n-l), l = 0, 1, ..., L-1$, i.e., the error is orthogonal to all the data used to form the estimate. Equation (2.20) is also defined as the cross correlation vector $R_{ex}(l)$ between the error and the input. Note that

$$\begin{aligned} R_{ex}(l) =& E\{e(n)x(n-l)\} = \\ =& E\{(d(n) - y(n))x(n-l)\} = \\ =& E\{d(n)x(n-l)\} - E\{y(n)x(n-l)\} = \\ =& R_{dx}(l) - R_{yx}(l), \end{aligned} \tag{2.21}$$

where $R_{dx}(l)$ is the cross correlation between the desired response and the input, and $R_{yx}(l)$ is the cross correlation between the estimation of the filter and the input. Therefore, an alternative way of stating the orthogonality principle (2.20), based on (2.21), is that

$$R_{dx}(l) = R_{yx}(l). \tag{2.22}$$

In order to find the impulse response values, observe that since $y(n)$ is obtained by filtering $x(n)$ through a linear time-invariant (LTI) system with impulse response w_l, the following relationship applies:

$$R_{yx}(l) = R_{xx}(l)w_l, \tag{2.23}$$

where $R_{xx}(l)$ is the input autocorrelation matrix. Combining this with the alternative statement of the orthogonality condition (2.22), we can write

$$R_{xx}(l)w_l = R_{dx}(l). \tag{2.24}$$

Equation (2.24) defines the optimum filter coefficients, in terms of two correlation functions. These equations are called the Wiener-Hopf equations. Under the assumption on the positive definiteness of R_{xx}, the solution of (2.24) is given by

$$w_{opt} = R_{xx}^{-1} R_{dx}, \tag{2.25}$$

which is known as the Wiener filter. The FIR Wiener filter is related to the least squares estimate, but minimizing the error criterion of the latter does not rely on cross correlations or autocorrelations. Its solution converges to the Wiener filter solution.

The statistical theory of regression is concerned with the prediction of a dependent variable y by other measured independent variable x (the regressor). The case of one independent variable is called simple linear regression. For more than one independent variable, the process is called multiple linear regression (MLR) [76]. This term is distinct from multivariate linear regression, where multiple correlated dependent variables are predicted, rather than a single variable [77]. Typically, an exact a priori information about the relationship between y and x is not supplied [78]. Therefore, a suitable parametrization is estimated, constrained to be linear, by fitting y to a linear combination of x:

$$y_i = \beta_1 x_{i1} + \cdots + \beta_L x_{iL} + \varepsilon_i = \sum_{j=1}^{L} \beta_j x_{ij} + \varepsilon_i, \quad \text{for } i \in 1, 2, ..., n, \tag{2.26}$$

where y_i is the response for the i-th observation, β_j is the coefficient of the j-th predictor, x_{ij} is the j-th predictor for the i-th observation, and ε_i is the i-th error. The problem is to find a function of the regressors such that the error

$$\varepsilon_i = y_i - \sum_{j=1}^{L} \beta_j x_{ij}, \tag{2.27}$$

becomes small. If y and x are described within a stochastic framework, the aim is to minimize the following:

$$E\left[\varepsilon_i\right]^2 = E\left[y_i - \sum_{j=1}^{L} \beta_j x_{ij}\right]^2, \tag{2.28}$$

which leads to

$$V_n(\beta) = \frac{1}{n} \sum_{i=1}^{n} \left[y_i - \sum_{j=1}^{L} \beta_j x_{ij}\right]^2. \tag{2.29}$$

A suitable β to choose is the minimizing argument of (2.29):

$$\hat{\beta}_n = \arg\min V_n(\beta). \tag{2.30}$$

This is the least square estimate (LSE) which is a set of formulations for solving statistical problems involved in linear regression. Notice that this method of selecting β makes sense whether or not there is a stochastic framework for the problem. The parameter $\hat{\beta}_n$ is the value that gives the best performing predictor when applied to past data. The unique feature of (2.29) is that it is a quadratic function of β. Thus, it can be minimized analytically, and also all $\hat{\beta}_n$ that satisfy

$$\left[\frac{1}{n} \sum_{i=1}^{n} x_i x_i^T\right] \hat{\beta}_n = \frac{1}{n} \sum_{i=1}^{n} x_i y_i. \tag{2.31}$$

yield the global minimum of $V_n(\beta)$. The set of linear equations in (2.31) are known as the normal equations. If the matrix on the left side is invertible, the LSE becomes

$$\hat{\beta}_n = \left[\frac{1}{n} \sum_{i=1}^{n} x_i x_i^T\right]^{-1} \frac{1}{n} \sum_{i=1}^{n} x_i y_i. \tag{2.32}$$

The relation between the Wiener filter and the LSE can be appreciated by comparing the minimization (2.17) and (2.30), that lead to (2.25) and (2.32).

For some calculations, (2.29) can be expressed in matrix form

$$V_n(\beta) = \frac{1}{n}\,|Y - X\beta|^2 = \frac{1}{n}(Y - X\beta)^T(Y - X\beta), \tag{2.33}$$

where

$$\mathbf{X} = \begin{bmatrix} x_{11} & x_{12} & \cdots & x_{1L} \\ x_{21} & x_{22} & \cdots & x_{2L} \\ \vdots & \vdots & \ddots & \vdots \\ x_{n1} & x_{n2} & \cdots & x_{nL} \end{bmatrix}, \qquad \boldsymbol{\beta} = \begin{bmatrix} \beta_1 \\ \beta_2 \\ \vdots \\ \beta_L \end{bmatrix}, \quad \text{and} \qquad \mathbf{Y} = \begin{bmatrix} y_1 \\ y_2 \\ \vdots \\ y_n \end{bmatrix}.$$

Then, the gradient of error should vanish at minimum:

$$\nabla V_n(\beta) = \frac{1}{n}\left[-2X^T Y + 2X^T X\beta\right] = 0. \tag{2.34}$$

Hence, (2.31) takes the form

$$[X^T X]\hat{\beta}_n = X^T Y, \tag{2.35}$$

and the estimate becomes

$$\hat{\beta}_n = [X^T X]^{-1} X^T Y. \tag{2.36}$$

Usually, the regressors X are extended with a constant, $x_{i0} = 1$ for all $i = 1, 2, ..., n$, where the coefficient β_0 corresponding to this regressor is called the intercept.

The Wiener filter, used in many studies (see, e.g., [20, 42, 61, 63, 64, 65, 66]), is a class of linear optimum discrete-time filter, which focuses on optimizing a cost function. The selected optimization for the filter is the minimization of the mean square value of the estimation error, i.e., the least mean square (LMS) value. It has been stated that there is a correspondence between the LMS algorithm and the linear LSE [74]. One can appreciate the similarities mainly in the minimization criterion. The least squares approach is often used to fit linear regression models, like the MLR used in many studies (see, e.g., [19, 62, 67, 68, 69, 70, 71, 72, 73]), where sometimes they are also called multidimensional linear regression models. These types of methods have been widely used because of their simple but powerful solution [79]. Thus, the method of MLR was chosen for the decodification process in this thesis. Furthermore, the MLR is expected to behave in a simple and efficient manner, without displaying a heavy computational burden.

2.2.2 Genetic Algorithm

In 1975 John Holland presented the genetic algorithm (GA) as an abstraction of biological evolution and gave a theoretical framework for adaptation. The genetic algorithm of Holland is a method for moving from one population of chromosomes to a new population by using a kind of natural selection together with the genetics-inspired operators of crossover, mutation, and inversion. The evolutionary-computation community has no rigorous definition of genetic algorithm accepted that differentiates them from other evolutionary computation methods. However, GAs have at least the following elements in common: populations of chromosomes, selection according to fitness, crossover to produce new offspring, and random mutation of new offspring [80].

GAs have been used in some BMI or other types of wearable robots. However, the implementation of the GA in these studies is to find the optimum model or optimal set of parameters for an estimation of a biological signal from another biological signal. For example, Oyong et al. 2010 [81], used a GA which performed two tasks. The first task was to find the most appropriate mathematical model (7 proposed models) that fitted the processed EMG data into the actual torque of the upper limb movement. The second task was to find the optimum parameters associated with the chosen model. Paek et al. 2013 [82] reconstructed surface EMG from EEG signals using a linear model (the Wiener filter). However, they used a GA to find the optimal set of EEG sensors (from 49 sensors) that maximized the performance of the reconstruction. Hayashi et al. 2015 [83] estimated from EEG signals if tests subjects moved the elbow joint. The motion of the elbow was estimated by using an artificial neural network. Nevertheless, the weights for the hidden and output layers were obtained with a GA. These studies show that the GA are mostly used to find an optimal solution for the different methods or models used for estimation or reconstruction of one signal from another type of signal.

In a GA, a population of candidate solutions (called individuals) to an optimization problem is evolved toward better solutions [80]. This collection of candidate solutions to a problem is called the search space. Each candidate solution has a set of properties which can be mutated and altered [84]. This set of properties (also called chromosomes) need a genetic representation of the candidate solutions. The chromosomes in a GA population typically take the form of bit strings or an array of bits [84]. Arrays of other types and structures can be used in essentially the same way. The main property that makes these genetic representations convenient is that their parts are easily aligned due to their fixed size [80, 84]. The GA processes populations of individuals, successively replacing one such population with another. The GA most often requires a fitness function that assigns a score (or fitness value) to each individual in the current population. The fitness value of an individual depends on how well that individual solves the problem at hand [80]. After the genetic representation and the fitness function are defined, a GA starts by generating an initial population of solutions and then to improve it through repetitive application of operators that include selection, crossover, and mutation. Each iteration of this repetitive process is called a generation. An entire set of generations is called a run.

The genetic operators are explain next, which are included in the pseudo-code (Algorithm 1).

Algorithm 1 Genetic algorithm pseudo-code.

```
Initialize population
repeat
  Evaluation
  Selection
  Crossover
  Mutation
until Generations completed
```

Selection: During each iteration, a portion of the existing population is selected to breed a new population. Individuals are selected based on their fitness value, where solutions more fit have high probability to be selected to reproduce and generate the new population [80, 81].

Crossover: Crossover is a method of producing a new individual from a pair of selected chromosome. This operator exchanges the subsequences before and after a randomly chosen crossover point in the selected parent chromosomes to create a new individual that shares their characteristics [80, 81].

Mutation: This operator is applied to an individual by randomly modifying a part of its structure, enabling the GA to create a new individual for the next generation [80, 81].

Expanding in detail the pseudo-code, a GA follows the next list of steps [80]:

1. Begin with a randomly generated population of n chromosomes (candidate solutions to a problem).
2. Calculate the fitness of each chromosome in the population.
3. Repeat the following steps until n offspring have been created:
    (a) Select a pair of parent chromosomes from the current population, based on the fitness value. Selection is done with replacement, meaning that the same chromosome can be selected more than once to become a parent.
    (b) With probability pc (the crossover probability or crossover rate), crossover the pair at a randomly chosen point (chosen with uniform probability) to form an offspring. If no crossover takes place, form the offspring that is an exact copy of a parent.
    (c) Mutate the offspring with probability pm (the mutation probability or mutation rate), and place the resulting chromosome in the new population.
4. Replace the current population with the new population.
5. Go to step 2.

Generally, new generations have better overall fitness value than previous generations. Therefore, at the end of a run, there is often one or more highly fit chromosomes in the population. Since randomness plays a large role in each run, more runs with different initial populations will generate different detailed behaviors. Here the simple procedure for most applications of GAs was described. There are many parameters to consider when applying this method, such as size of the population and probabilities of crossover and mutation. Success of the algorithm depends on these details [80].

Several studies have implemented the GA to find an optimization of a model or set of parameters (see, e.g., [81, 82, 83]). The GA applied in this study, attempts to find an optimal set of functions that improves the performance of the MLR method applied for the decodification. As mentioned in this section, the GA requires of a fitness value for the selection operator. Some functions of evaluation are described in the next section. These evaluation metrics are used to evaluate the decodification itself. However, only one of these evaluation metrics is used for the fitness value.

2.2.3 Evaluation metrics

Estimating the performance of the prediction model is crucial to the decodification of neural signals. Discrete classification methods have some established performance metrics [85] and there exist some studies that compare those metrics for the use in BCIs [86]. Most of these metrics include the number of correct classifications and the number of mistaken classifications presented in what is called a confusion matrix. However, when using continuous trajectory reconstruction methods for the decodification of neural signals, there are different performance metrics used in the literature. Spüler et al. 2015 [87] mention the following: correlation coefficient (CC), normalized root mean square error (NRMSE), signal-to-noise ratio (SNR), coefficient of determination, and global deviation. Some of these metrics are described next.

Correlation coefficient: The most used metric to evaluate the continuous trajectory reconstruction decodification is the CC (also called Pearson's correlation coefficient, r-value, or Pearson's r-value). The CC is a dimensionless measure of the linear relation between two quantitative variables, in which usually the value lies in the range of -1 to $+1$. Negative values of CC correspond to an inverse linear relation between the variables, and positive values correspond to a direct linear relationship. When the value approaches zero, it is an indication of the absence of correlation (but not necessarily the independence of the two variables) [88]. A common form of the correlation coefficient is the following:

$$\mathrm{CC}(x,y) = \frac{\sum_{i=1}^{N}(x_i - \bar{x})(y_i - \bar{y})}{\sqrt{\sum_{i=1}^{N}(x_i - \bar{x})^2}\sqrt{\sum_{i=1}^{N}(y_i - \bar{y})^2}}, \tag{2.37}$$

where x and y are two variables, $\bar{x}$ is the mean of x, $\bar{y}$ is the mean of y, and N is the number of samples.

Normalized root mean square error: Root mean square error (RMSE) is a metric commonly used in regression analysis that measures the standard deviation of the residuals (or prediction errors). Usually, the RMSE is considered a measure of the differences between values predicted or reconstructed by a model and the real or actually observed values. The RMSE (also called root mean square deviation, RMSD) is defined by:

$$\mathrm{RMSE} = \sqrt{\frac{\sum_{i=1}^{N}(y-\hat{y})^2}{N}}, \tag{2.38}$$

where y is the observed variable, $\hat{y}$ is the predicted or reconstructed values of y, and N is the number of samples. The RMSE is useful to compare different methods applied to the same dataset, but should not be used when comparing across datasets that have different scales [89]. Normalizing the RMSE facilitates the comparison between datasets with different scales [87] and is usually represented as a percentage. Since there is no consistent means of normalization in the literature, the common choice is the range (defined as the maximum value minus the minimum value) of the observed data:

$$\mathrm{NRMSE} = \frac{\sqrt{\frac{\sum_{i=1}^{N}(y-\hat{y})^2}{N}}}{(y_{\max} - y_{\min})}, \tag{2.39}$$

where $y_{\max}$ and $y_{\min}$ indicate the maximum and minimum values of the indicated signal.

Signal-to-noise ratio: The SNR is a unitless measure that compares the level of a desired signal to the level of background noise. This comparison is defined as the ratio of the power of a signal (meaningful information) to the power of background noise (unwanted signal):

$$\mathrm{SNR} = \frac{P_{signal}}{P_{noise}}, \tag{2.40}$$

where P is average power. If the variance of the signal and noise are known, and both have a mean of zero, the SNR can be calculated by:

$$\mathrm{SNR} = \frac{\sigma^2_{signal}}{\sigma^2_{noise}}. \tag{2.41}$$

However, if the variance or mean values are unknown, the power of a random variable equals its mean-squared value. Thus, the signal power equals $E\left[S^2\right]$ [90], where S can be the signal or the noise. SNR is widely used in science and engineering and has been previously used to measure BCI and BMI decoding performance (see, e.g., [20, 42, 61, 90, 91, 92, 93, 94, 95]). The SNR gives a measure of the accuracy of estimated position in terms of the error variance. High SNR values are desired since they are produced when the estimated output error variance is small [91]. Usually, a ratio higher than 1:1 is favorable since it indicates more signal than noise.

In scientific practice is good to state multiple performance metrics. However there is a need to decide on a specific metric when it comes to automatic parameter optimization. Different metrics tend to capture different properties of the prediction performance or accuracy. Therefore it is unclear which method is overall best suited for evaluation purposes [87].

In this chapter, the methods that provide a set of indices are described. Such indices are expected to give insight of the underlying dynamics of the EEG signals during lower limb motor tasks. These insights might give discernment for the construction or usage of a proper method applied to the decodification of the lower limb kinematics. Regarding the decodification method, in this work the linear optimum filter is described, which has a correspondence with the MLR. It is expected that the indices provide the insights of another type of decodification method or improve the existing methods. On a similar approach, a genetic algorithm is also described in this chapter. Such algorithm is implemented in order to search for an optimization of the already described decodification method. The next chapter involves the description of the experimental setups, where EEG signals are registered alongside kinematic variables.

Chapter 3

Experimental Setups

This chapter describes the specifications for the experiments, which include the recording of the EEG signals for synchronous and asynchronous lower limb mobility protocols. Both protocols involve a data acquisition section describing the equipment used, and the activities performed by the test subjects. After such sections, preprocessing methods are described for each protocol.

When performing experiments for continuous trajectory reconstruction of the lower limbs, most of the literature use the task of walking, generally over a treadmill. This can be seen in the works of Fitzsimmons et al. [20] (performed by trained monkeys), Pressaco et al. [42, 61], He et al. [27], Luu et al. [60, 95], and Úbeda et al. [41]. These works show that using slow cortical potentials of the EEG, i.e., cortical information in low frequency bands, it is possible to obtain kinematic information of the gait cycle during locomotion. However, there are some time varying mechanical artifacts associated with head movements during locomotion [96].

To avoid the influence of artifacts, or to reduce them significantly, another type of experiments different than locomotion had to be taken into consideration. Úbeda et al. 2015 [62] presented an experiment where only an individual joint movement is decoded in order to reduce the influence of motion artifacts (described in Section 3.2). Based on this experimental registry, a similar registry was carried out, with tasks different than locomotion (described in Section 3.1). Furthermore, in order to compare and improve the decodification performances, a collaboration with three groups was established. The collaboration is under the project "Design of Brain Computer Interfaces for the Control of Lower Limb Assistive Technologies" from the network "Biosystems and biomechatronics," formed by the academical groups of “Biosystems” (UDG-CA-789) and “Technology and Mechantronics Innovation” (UANL-CA-272), and the investigation group of “Brain Machine Interface Lab.” The main goal of such project is to generate directives for the innovation of therapies and rehabilitation for neuromuscular pathologies, creating an impact in the medical community mainly regarding innovative tools improving the treatment to patients. The proposed tools involve the design of medical experiments, electrophysiological signal processing, modeling and control of dynamical systems (robotic systems, biomedic systems, and graph theory), and intelligent systems (with application in parametric adjustment of mathematical models).

Regarding the experimental architecture presented by Úbeda et al. 2015 [62], the subjects attempted to perform constant movements, i.e., the subjects were cued to carry out the instructed task at their own pace for a certain period of time. During the performance of the task, no further cues were used. Hence, in this work such experimental architecture is called asynchronous protocols [97]. Bradberry et al. [67] and Lv et al. [93] used this type of architecture on upper limb kinematic decodification. Where they let the subjects self-chose the movements. Kim et al. [72] and Zhang et al. [19] performed experiments that consisted of subjects following a certain predefined trajectory for the upper limbs, which in a sense made the subjects follow the pace of the trials. Nevertheless, this types of experiments behave in a similar way in concept to those of the gait cycle, i.e., when a pace is established.

However, Kim et al. [98] performed experiments similar to Bradberry et al. [67], but following a timeline of instructions, or cues. In this manner, the subjects followed the established pace of the experiment, rather than their own pace. For this reason, in this work, experiments are proposed in order for the subjects to perform tasks in a controlled manner under provided instructions. This experiments are called synchronous protocols [97] and are described next.

3.1 SYNCHRONOUS PROTOCOLS

As it was stated at the beginning of this chapter, some studies found in the literature carry out experiment registers where the test subjects perform an instructed task at their own pace after a single cue. Such cue marks the beginning of the registry. However during the acquisition of the data, there is no knowledge of the current activity performed by the requested limb. For this reason, synchronous protocols were proposed in order to have the knowledge of the current activity of the lower limb. The database of this protocol was acquired at the Mechatronics Laboratory in the Center of Innovation, Research, and Development in Engineering and Technology of the Universidad Autónoma de Nuevo León (Mexico), under the collaboration project “Design of Brain Computer Interfaces for the Control of Lower Limb Assistive Technologies.” The equipment used for the acquisition of the neural signal was the MOBITA-W-32EEG system of the Laboratory of Biomedical Signal Processing from The Center of Research and Advanced Studies (Cinvestav) at Monterrey.

For this database, eight subjects (4 male and 4 female) with no motor pathologies were asked, and gave oral consent, to perform the trials. Subjects were asked to execute two lower limb tasks, both performed while remaining seated. The first task (Task 1) consisted in raising the foot by performing an isotonic extension of the knee (Figure 3.1a). The second task (Task 2) consisted in raising the knee by realizing an isotonic flexion on the hip joint (Figure 3.1b). The trial began with the resting time, were the subject was sitting comfortably on a chair maintaining the thigh in an horizontal position and the shank around 90° with respect to the thigh. After 30 seconds, the subject was cued to raise the right limb by the isotonic movement to its maximum position, holding the limb up by performing an isometric exercise until 3 seconds had passed since the cue. Next, the subject was cued to lower the limb maintaining this position for another 3 seconds. After 10 repetitions, the subject rested for another 30 seconds. A demonstration of a trial is shown in Figure 3.2. Each subject performed 10 trials for both tasks. To have the trials controlled, the subjects were shown a video with the cues to raise or lower the limb. This video consisted of different simple illustrations that indicate the activities, such as the resting time, that helps the subject to focus on a single white dot in order to avoid getting distracted. Followed by 10 repetitions of green-upward and red-downward arrows, to indicate the raising and lowering of the limb. The video counted with a start and finish frame. A diagram of this procedure is shown in Figure 3.3.

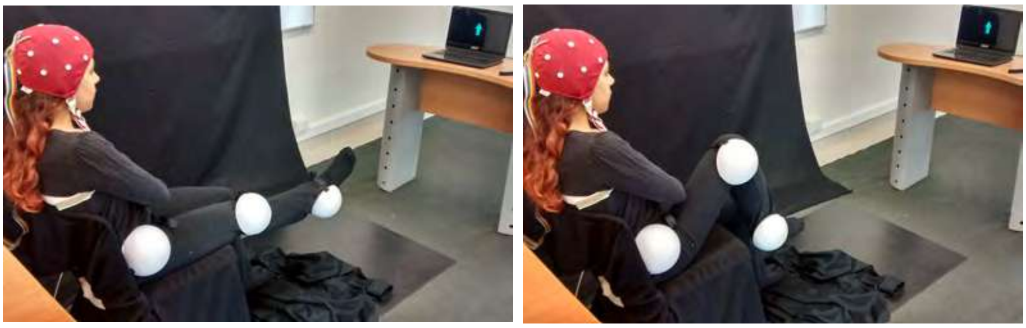

(a) Task 1.

(b) Task 2.

Figure 3.1: Tasks performed by the subjects: a) raising the foot by performing an isotonic extension of the knee, and b) raising the knee by realizing an isotonic flexion on the hip joint.

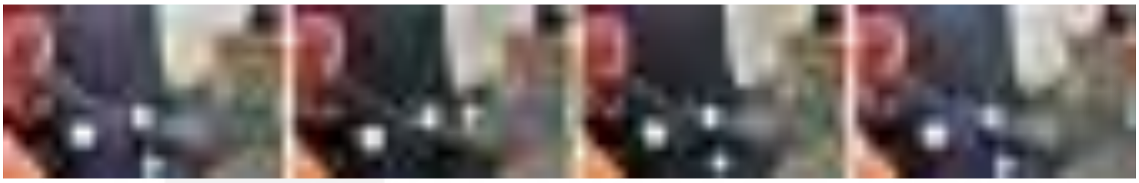

Figure 3.2: One subject using the EEG system and performing Task 1, following indications displayed on the screen. From left to right: first resting period (indicated by a white dot on the screen), raising of the right lower limb (indicated by a green upward arrow), lowering of the right lower limb (indicated by a red downward arrow), and second resting period (indicated by a white dot).

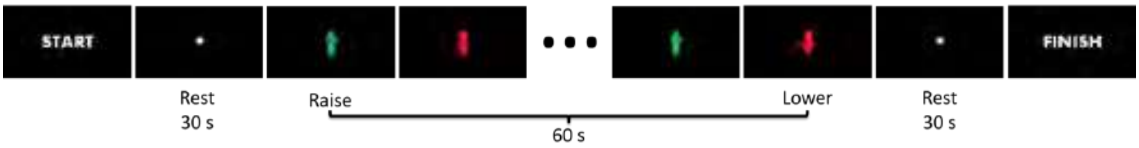

Figure 3.3: Frames of the indications presented in the video to rest (white dot, 30 s), raise or lower the limb (green and red arrow respectively, 10 repetitions, each lasted 3 s); from start to finish the entire trial lasted 120 s.

3.1.1 Data Acquisition

For the acquisition of the neural signals, the MOBITA-W-32EEG system was used. The Mobita® was adapted to a 10/20 electrode cap with 19 channels available, which are: Fp1, Fp2, F3, F4, C3, C4, P3, P4, O1, O2, F7, F8, T3, T4, T5, T6, Cz, Fz, and Pz. Figure 3.4 shows the distribution of the electrodes, which also covered the relevant surface of the scalp, particularly the regions where motor activity occurs. After placing the cap on the subjects, the impedance of the electrodes was checked using the Model 1089NP Checktrode$^{\mathrm{TM}}$. After applying conductive gel, the desired impedance range was kept at a value less than $5K\Omega$ which means a good preparation, according to the specifications of the product, or between $5K\Omega$ to $10K\Omega$ meaning it was a sufficient preparation. In these experiments, the EEG signals were registered with a sampling frequency of 1000 Hz. During the EEG recording, markers indicating the raising and lowering of the limb were added on the software in order to specify the beginning and ending of each task.

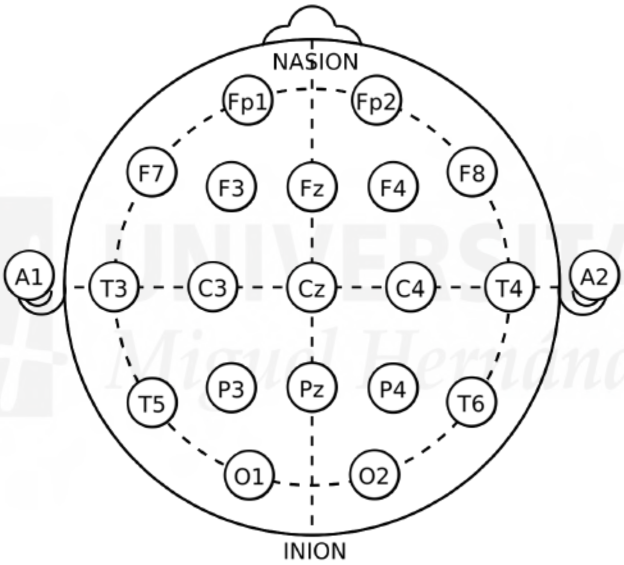

Figure 3.4: Electrode distribution of the International 10/20 System. 19 active electrodes were connected to the MOBITA-W-32EEG system. Electrodes A1 and A2 were used as references during the impedance checking.

For the acquisition of the kinematic variables, the subjects were placed in a controlled environment and wore dark clothes with three white spherical markers (Figure 3.5). The markers were located on the right hip, knee, and ankle in order to give their locations by the processing of the video taken by a NI 1752 Smart Camera running at 60 frames per second (fps). After the videos were processed, the locations of the markers served in order to obtain the joint angles of the hip and knee by trigonometric functions.

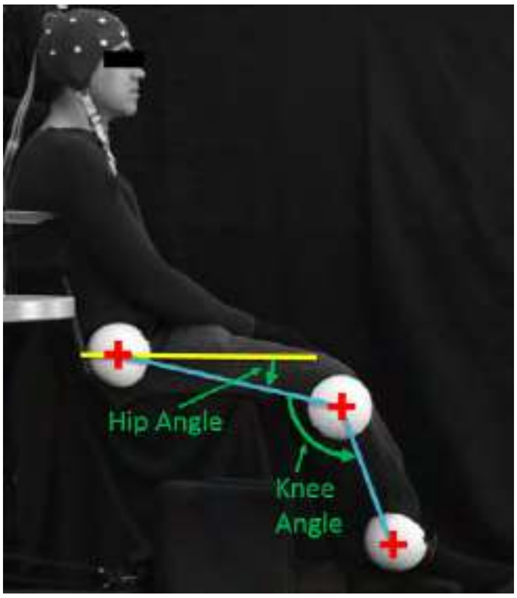

Figure 3.5: Test subject wearing three spherical markers allocated on the right hip, knee, and ankle, for video processing.

3.1.2 Signal Preprocessing

The original data acquired was preprocessed in two different data sets for this study. For the first data set, ten peripheral EEG channels were removed (namely Fp1, Fp2, F7, F8, T3, T4, T5, T6, O1, and O2), as they are more susceptible to artifacts, thus F3, Fz, F4, C3, Cz, C4, P3, Pz, and P4 were selected. For the second data set, all EEG channels were taken into consideration, including those not involved with motor regions or those that may have different types of artifacts. For both data sets, a preprocessing of the EEG signal was carried out using the computational method of fast independent component analysis (FastICA). This method was implemented solely to remove blink artifacts embedded in the data. This method is described next.

Fast independent component analysis (FastICA): The independent component analysis (ICA) is a technique to separate linearly mixed components [99], as a random vector $\mathbf{s} = (s_1, ..., s_n)^T$, by using a linear static transformation $\mathbf{W}$ (known as the unmixing matrix) to an observed data $\mathbf{x} = (x_1, ...x_m)^T$, i.e.,

$$\mathbf{s} = \mathbf{W}\mathbf{x}. \tag{3.1}$$

However, one must assume that the components are non-Gaussian signals and that they are statistically independent from each other [100]. For this reason, there are some applicable techniques that make the problem of ICA estimation simpler and better conditioned [101]. First, it is necessary for the observable variable $\mathbf{x}$ to be zero mean. When this does not apply, the process of centering takes place. This process is the subtraction of the mean vector $\mathbf{m} = E\{\mathbf{x}\}$ to the variable $\mathbf{x}$ making it a zero-mean variable. This also implies that $\mathbf{s}$ becomes zero-mean. After the observed vector $\mathbf{x}$ is centered, it is useful to whiten the variables. This indicates the observed vector $\mathbf{x}$ is transformed linearly to obtain a new white vector $\tilde{\mathbf{x}}$, i.e., its components are uncorrelated and their variances are equal to 1. This implies the covariance matrix of $\tilde{\mathbf{x}}$ equals the identity matrix, i.e.,

$$E\{\tilde{\mathbf{x}}\tilde{\mathbf{x}}^T\} = \mathbf{I}. \tag{3.2}$$

A common and popular method for whitening is by performing an eigenvalue decomposition on the covariance matrix of the centered data $\mathbf{x}$, $E\{\mathbf{x}\mathbf{x}^T\} = \mathbf{Q}\mathbf{D}\mathbf{Q}^T$, where $\mathbf{Q}$ is the matrix of eigenvectors of $E\{\mathbf{x}\mathbf{x}^T\}$ and $\mathbf{D}$ is the diagonal matrix of eigenvalues [101]. The whitened data is defined thus by

$$\tilde{\mathbf{x}} = \mathbf{Q}\mathbf{D}^{-1/2}\mathbf{Q}^T\mathbf{x}. \tag{3.3}$$

Maximizing the non-Gaussianity of $\mathbf{w}^T\mathbf{x}$ gives us one of the independent components, if vector $\mathbf{w}$ was one of the rows of $\mathbf{W}$ [99]. For ICA, the classical measure of non-Gaussianity is kurtosis or the fourth-order cumulant. A second very important measure of non-Gaussianity is given by negentropy. Negentropy is based on the information-theoretic quantity of (differential) entropy. Although these are objective functions for ICA estimation, in practice, one also needs an algorithm for maximizing the contrast function. FastICA is a very efficient method of maximization suited for this task. To measure non-Gaussianity, FastICA relies on a nonquadratic nonlinearity function $f(u)$, its first derivative $g(u)$, and its second derivative $g'(u)$ [101]. Examples of the functions are:

$$f(u) = \log\cosh(u), \quad g(u) = \tanh(u), \quad \text{and} \quad g'(u) = 1 - \tanh^2(u), \tag{3.4}$$

for general purposes, or more robust functions like

$$f(u) = -e^{\frac{-u^2}{2}}, \quad g(u) = ue^{\frac{-u^2}{2}}, \quad \text{and} \quad g'(u) = (1-u^2)e^{\frac{-u^2}{2}}. \tag{3.5}$$

The basic form of the FastICA algorithm is as follows:

1. Choose an initial (e.g., random) weight vector $\mathbf{w}$.
2. Let $\mathbf{w}^+ = E\{\mathbf{x}g(\mathbf{w}^T\mathbf{x})\} - E\{g'(\mathbf{w}^T\mathbf{x})\}\mathbf{w}$
3. Let $\mathbf{w} = \mathbf{w}^+/\|\mathbf{w}^+\|$
4. If not converged, go back to 2.

This one-unit algorithm estimates just one of the independent components, or one projection pursuit direction. To estimate several independent components, it is needed to run the one-unit FastICA algorithm using several units with weight vectors $\mathbf{w}_1, ..., \mathbf{w}_n$. To prevent different vectors from converging to the same maxima, the outputs $\mathbf{w}_1^T\mathbf{x}, ..., \mathbf{w}_n^T\mathbf{x}$ need to be decorrelated after every iteration. The Gram-Schmidt-like decorrelation is a simple way to achieve decorrelation, which is a deflation scheme [101]. This is based on the estimation of the independent components one by one. When p independent components, or p vectors $\mathbf{w}_1, ..., \mathbf{w}_p$, have been estimated, the one-unit fixed-point algorithm is run for $\mathbf{w}_{p+1}$, and after every iteration step the projections $\mathbf{w}_{p+1}^T\mathbf{w}_j\mathbf{w}_j,\ j = 1, ..., p$ are subtracted from $\mathbf{w}_{p+1}$ of the previously estimated p vectors, and then renormalize $\mathbf{w}_{p+1}$:

1. Let $\mathbf{w}_{p+1} = \mathbf{w}_{p+1} - \sum_{j=1}^{p} \mathbf{w}_{p+1}^T\mathbf{w}_j\mathbf{w}_j$;
2. Let $\mathbf{w}_{p+1} = \mathbf{w}_{p+1}/\sqrt{\mathbf{w}_{p+1}^T\mathbf{w}_{p+1}}$.

The preprocessing performed by the ICA (or FastICA) is usually used in the literature to separate brain activity from artifacts of several types, e.g., eye movements, blinks, anatomical or physiological processes [102, 103, 104, 105]. In this work, the FastICA was used to remove the blinking artifacts of the EEG signal.

Other steps were considered for preprocessing after the FastICA was applied. First the signals were filtered with two elliptic filters, a 5th order low-pass filter with a cutoff frequency of 2 Hz, followed by a 3rd order high-pass filter with a cutoff frequency of 0.1 Hz. Afterwards, the EEG data of each electrode was standardized with the following equation:

$$\mathrm{EV}[t] = \frac{V[t] - \bar{V}}{SD_V}, \tag{3.6}$$

where the signal is $V[t]$, the standardized value is EV$[t]$, for each time sample $[t]$, the mean of the signal is $\bar{V}$, and the standard deviation of the signal is SD_V. Regarding the kinematic variables, after the videos were processed to obtain the joint angles, they were upsampled to match the sampling frequency of the EEG signal.

3.2 Asynchronous protocols

As mentioned at the beginning of this chapter, there are studies found in the literature that carry out experiments where the test subjects perform an instructed task at their own pace after a single cue. During the acquisition of the data, the task performed by the test subjects is asynchronous, i.e., without cues. In this study, a database provided by the Brain Machine Interface System Lab was used with their permission. This database was taken into consideration because it has data from people that are healthy and people who have a spinal cord injury (SCI). Furthermore, since the experiments involve flexion/extension of the knee, the database can be compared to the protocol described in Section 3.1.

The database is part of the BioMot project-Smart Wearable Robots with Bioinspired Sensory-Motor Skills, whose main goal is to analyze dynamic sensorimotor interactions in realistic human locomotion and design an artificial cognitive system for embodiment into bioinspired wearable assistive devices [106] (grant agreement number IFP7-ICT-2013-10-611695). The complete database consisted on experimental trials performed by five individuals with incomplete SCI from the inpatients services at the National Hospital for Spinal Cord Injury in Toledo, Spain, and four healthy users. All participants signed the corresponding informed consent.

Subjects were asked to performed five types of simple movements divided in two sequences. However, in this work only one of the movements of sequence 1 was taken into consideration. The movement consisted on a continuous isotonic flexion/extension of a knee joint as shown in Figure 3.6. Subjects performed six runs consisting of 30 seconds of continuous movements. However, since the movements of the subjects were self-paced without cues for the flexions and extensions, these were considered asynchronous protocols.

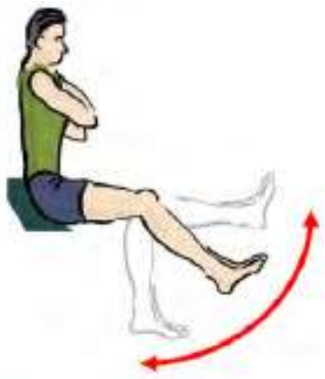

Figure 3.6: Type of movement performed by the subjects with a self imposed pace, i.e., an asynchronous movement.

3.2.1 Data Acquisition

EEG signals were recorded using two g.USBamp amplifiers (g.tec medical engineering GmbH, Schiedlberg, Austria), interconnected through a g.INTERsync module for correct synchronization. A total of 32 g.LADYbird active electrodes, composed of a sintered Ag/AgCl crown with a 2-pin safety connector, were placed on the scalp of the subjects using the g.GAMMAcap. Such active electrodes increase or improve the signal-to-noise ratio. The application of conductive gel was necessary to obtain more suitable signals from the active electrodes. Additionally, an antistatic wrist strap was used to remove external noises during the experiments. The configuration of the electrodes according to the international 10/10 system [107], follows the next distribution: Fz, FC5, FC3, FC1, FCz, FC2, FC4, FC6, C5, C3, C1, Cz, C2, C4, C6, CP5, CP3, CP1, CPz, CP2, CP4, CP6, P3, P1, Pz, P2, P4, PO7, PO3, POz, PO4, and PO8. In addition to the 32 mentioned electrodes, the ground electrode was placed in AFz and the reference was place on the right earlobe. Figure 3.7 shows the distribution of the electrodes, which covered the relevant surface of the scalp, particularly the regions where motor activity occurs. EEG signals were registered with a sampling frequency of 1200 Hz. The g.USBamp amplifiers internally filter the signals with two filters: one low-pass filter with a cutoff frequency of 100 Hz, and a notch filter at 50 Hz to remove the power line interference.

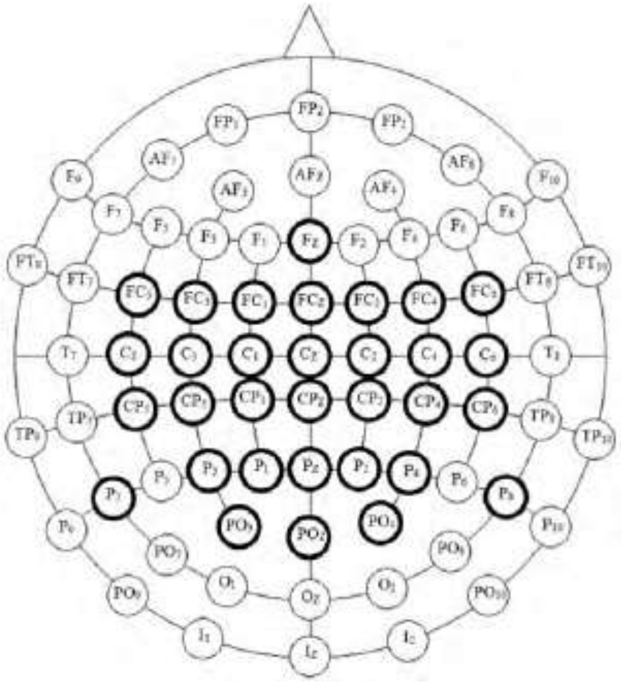

Figure 3.7: Electrode distribution of the international 10/10 system. Highlighted are 32 g.LADYbird active electrodes, which were connected to two g.USBamp amplifiers (g.tec medical engineering Gmbh, Schiedlberg, Austria) interconnected through a g.INTERsync module.

To obtain the kinematics of the lower limbs, seven inertial measurement units (IMUs) were used in the experiments. The IMUs were from the motion capture system Tech MCS (Technaid, Arganda del Rey, Spain), which integrate three types of sensors: accelerometers, a gyroscope, and a magnetometer. The data registered by the IMUs had a sampling frequency of 30 Hz. The placement of the IMUs can be seen in Figure 3.8. One IMU was placed on the back and six were placed on both legs over the thighs, shanks, and feet. Using the information of the seven IMUs, the angular velocity of the hip, knee, and ankle joints can be obtained. However, as previously stated, only the movement of the knee joint from this database was considered in this study.

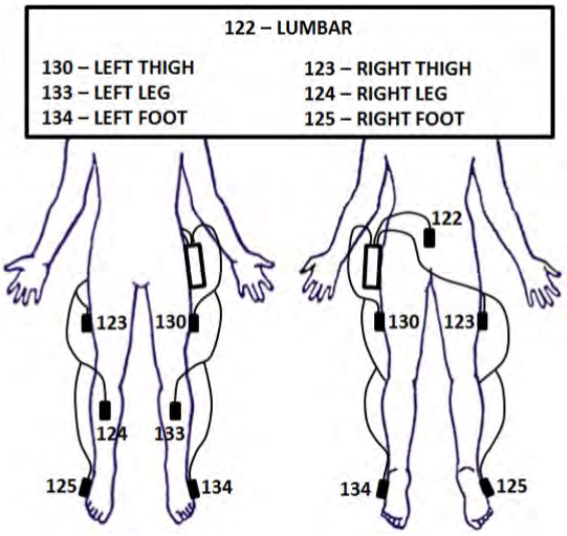
122 – LUMBAR
130 – LEFT THIGH
133 – LEFT LEG
134 – LEFT FOOT
123 – RIGHT THIGH
124 – RIGHT LEG
125 – RIGHT FOOT
123
130
124
133
125
134
122
130
123
134
125

Figure 3.8: Tag numbers of the seven IMUs connected to the TechHub with the following placement: one in the lumbar area, and the remaining six placed on both thighs, shanks, and feet. This distribution allowed to obtain the angular velocities of the hip, knee, and ankle joints of each leg. (Image taken with permission from [106]).

Figure 3.9 shows both equipments placed on the users. The lumbar IMU and TechHub are shown on the left, the g.USBamp amplifiers in the middle, and the IMUs of the right leg are shown on the right. Both the g.USBamp amplifiers and the TechHub have input/output trigger connections used to synchronize the recordings between the equipments.

3.2.2 Signal Preprocessing

The same filtering process described in Section 3.1.2 was used. Where two elliptic filters were used: a 5th order elliptic low-pass filter with a cutoff frequency of 2 Hz, followed by a 3rd order elliptic high-pass filter with a cutoff frequency of 0.1 Hz. Then, the EEG data of each electrode was also standardized with (3.6). As for the kinematic variables, the IMUs data were upsampled to match the sampling frequency of the EEG signal.

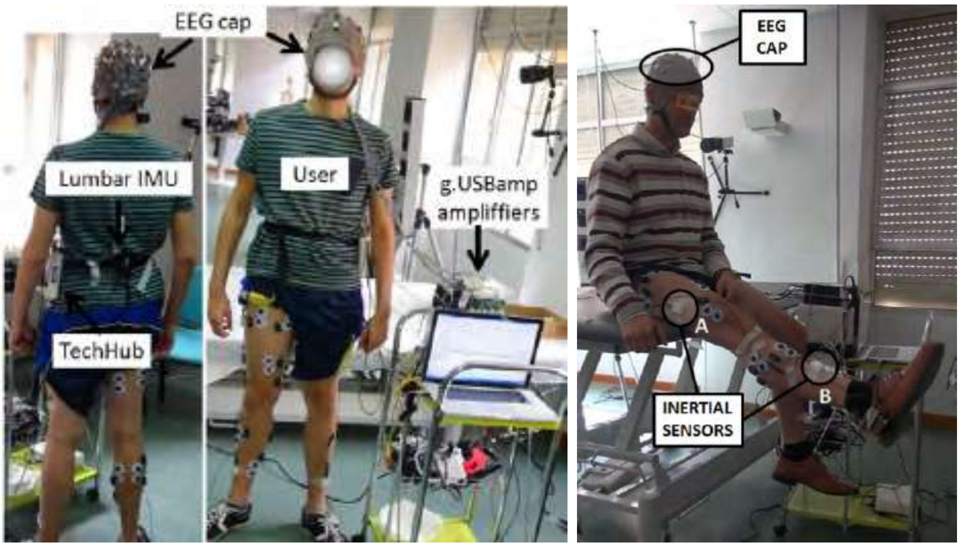

Figure 3.9: Environment of the experiment showing both equipments and two users. From left to right: the TechHub, the lumbar IMU, the EEG cap, the g.USBamp amplifiers, the inertial sensor A over the thigh, and the inertial sensor B over the shank.

The described experimental setups differ in that the first set is meant to be designed for the user to perform simple movements of lower limb. However, with the pre-established pace, the users were under a controlled process, i.e., synchronous. Additionally, the subjects alternated between isotonic and isometric exercises. The latter set of experiments were comprised of self-paced movements, i.e., asynchronous. The users established a certain constant velocity in a free isotonic movement. The EEG signals that were analyzed in this work came from the brain signals registered during the experimental setups described in this chapter. The next chapter involves the results obtained from using these data and using the methods described in Chapter 2.

Chapter 4

Results

This chapter shows the results of the procedures and simulations done for this research, which includes: the nonlinear dynamical analysis of the EEG neural signals for the synchronous protocols, the decodification of the EEG neural signals of the asynchronous protocols comparing different cortical regions and time intervals, the decodification of the synchronous protocols by segmentation of the data regarding the activity performed, the decodification of the synchronous protocols comparing different cortical regions, time delays, and gaps for such delays, and the optimization of the decodification with the implementation of a genetic algorithm. The first section displays the results for the Hurst exponent, correlation dimension, and the largest Lyapunov exponent of the synchronous protocols. The decodification results are divided in four sections, starting with the parametric adjustments for the decodification of the asynchronous protocols. Then the synchronous protocols are used for the decodification by segmentation. Afterwards this segmentation is further used to find a parametric adjustment for the synchronous protocols. Finally, the decodification by segmentation was used by the genetic algorithm, which uses transformations to the EEG signals.

4.1 Randomness & nonlinear dynamical analysis

It was stated in Section 3.1.2 that two data sets were considered for the synchronous protocols described in Section 3.1. The first data set, which consisted of nine electrodes, was considered for the nonlinear dynamical analyses mentioned in Section 2.1. Only the FastICA preprocessing was applied to this data set before these analyses, i.e., frequency filtering and standarization of the data were not yet applied. As it was stated, markers indicating the raising and lowering of the limb were added on the software in order to specify the beginning and ending of each task during the EEG recording. Each trial included 10 repetitions, where the raise-lower periods lasted 60 s divided in 20 windows of 3 s (3000 samples) each, as it can be seen in green-red windows at the bottom of Figure 4.1. Also, both resting times were divided in 10 windows, 3 s each, which can be seen in the blue windows at the bottom part of Figure 4.1. Each of these time windows are the inputs to the methods selected here to analyze the nonlinear dynamics of the neural activity associated to lower limb movements described in the experimental setup of Section 3.1.

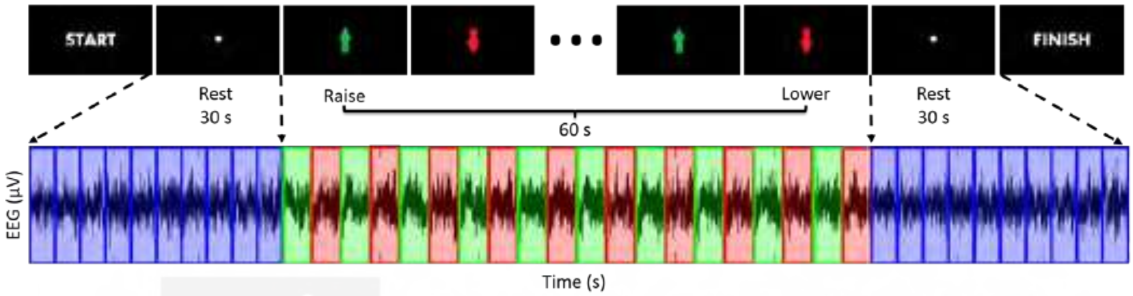

Figure 4.1: Top: frames of the indications presented in the video to rest (white dot, 30 s), raise or lower the limb (green and red arrows respectively, 10 repetitions each, lasting 3 s). The entire trial lasted, from start to finish, 120 s. Bottom: illustration of the EEG signal segmentation of a full trial into forty time windows 3 s each (3000 samples), where blue is the resting time (20 windows, 10 at the beginning and 10 at the end), green the raising time (10 windows), and red the lowering time (10 windows) of the limb. Each time window served as inputs to the nonlinear analyses.

All the procedures presented in this work were numerically implemented in Matlab® (R2015a). As it was stated in the experimental setup (Section 3.1), $N_S = 8$ subjects were enrolled in the experiment. Each subject performed two lower limb tasks (Task 1 and Task 2) consisting of $N_T = 10$ trials each. The interest is to analyze the EEG signal of the selected nine electrodes for each trial, according to the window segmentation described at the bottom of Figure 4.1. The indices H, CD, and LLE are computed from the EEG signal for each electrode (E), window (W), subject (S), and trial (T). To show the reproducibility of the results, each index is presented as averages between the subjects and trials for each window and electrode.

This is expressed as:

$$\mu_{W,E,I} = \frac{1}{N_S N_T} \sum_{S=1}^{N_S} \sum_{T=1}^{N_T} I(EEG_{T,S,W,E}), \tag{4.1}$$

where $E \in \{F3, Fz, F4, C3, Cz, C4, P3, Pz, P4\}$, $W \in \{1, ..., 40\}$, and $I \in \{H$, CD, LLE$\}$. The corresponding standard deviation is also computed by

$$\sigma_{W,E,I} = \sqrt{\frac{1}{N_S N_T} \sum_{S=1}^{N_S} \sum_{T=1}^{N_T} \left| I(EEG_{T,S,W,E}) - \mu_{W,E,I} \right|^2}. \tag{4.2}$$

4.1.1 HURST EXPONENT

The number of time spans of observations were limited to 50, since subseries of smaller length lead to a high variance of the R/S estimates. In the following graphs the mean and standard deviation of H (μ_H and σ_H, respectively) corresponding to the nine electrodes and the 40 windows are shown. Figure 4.2 presents the results of Task 1, whereas Figure 4.3 presents results of Task 2. The results show that the time series are nonrandom and persistent because the means (μ) of the nine electrodes in Figure 4.2 and Figure 4.3 are near to 1. Moreover, the mean and standard deviation of the EEG signal are computed in order to quantify the nonrandomness. As mentioned in Section 2.1.1, a stationary signal preserves constant values of mean and standard deviation. On the other hand, nonconstant values are related to nonstationary. As can be seen in Figures 4.4 and 4.5, the resting periods (windows 1-10 and 31-40) have small variations, meanwhile the raising and lowering periods (windows 11-30) have larger variations, therefore they behave nonstationarily. This behavior is more evident on electrodes Cz and Pz, which are located over the motor cortex.

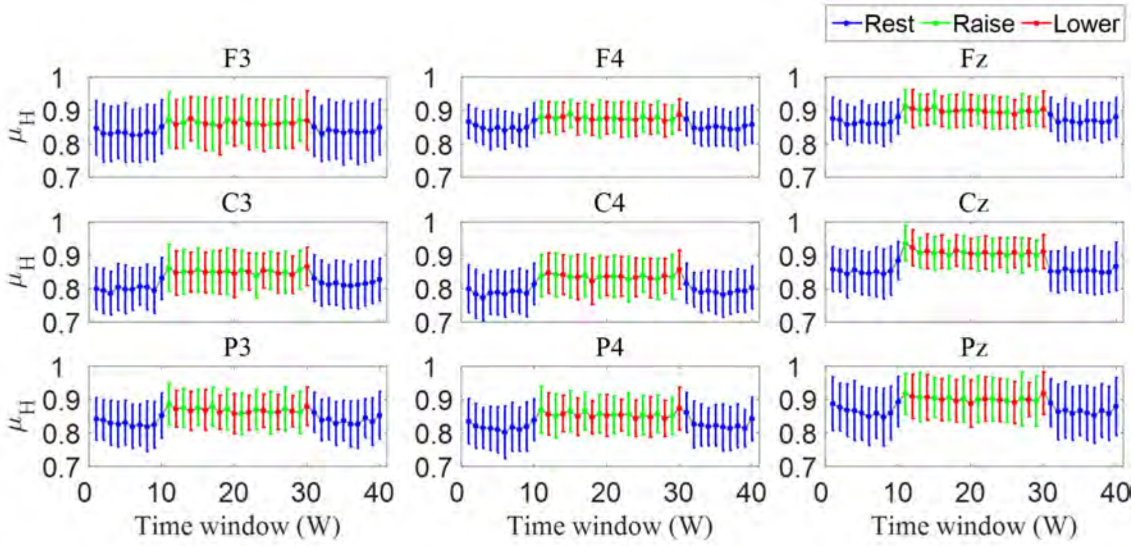

Figure 4.2: Mean and standard deviations of H calculated between eight subjects and ten trials, for nine electrodes during Task 1.

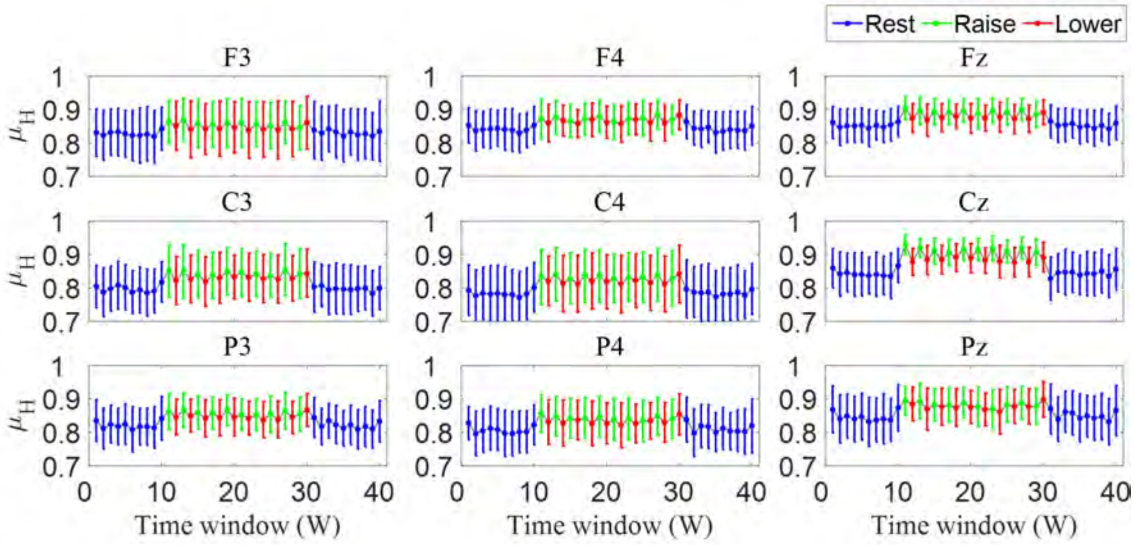

Figure 4.3: Mean and standard deviations of H calculated between eight subjects and ten trials, for nine electrodes during Task 2.

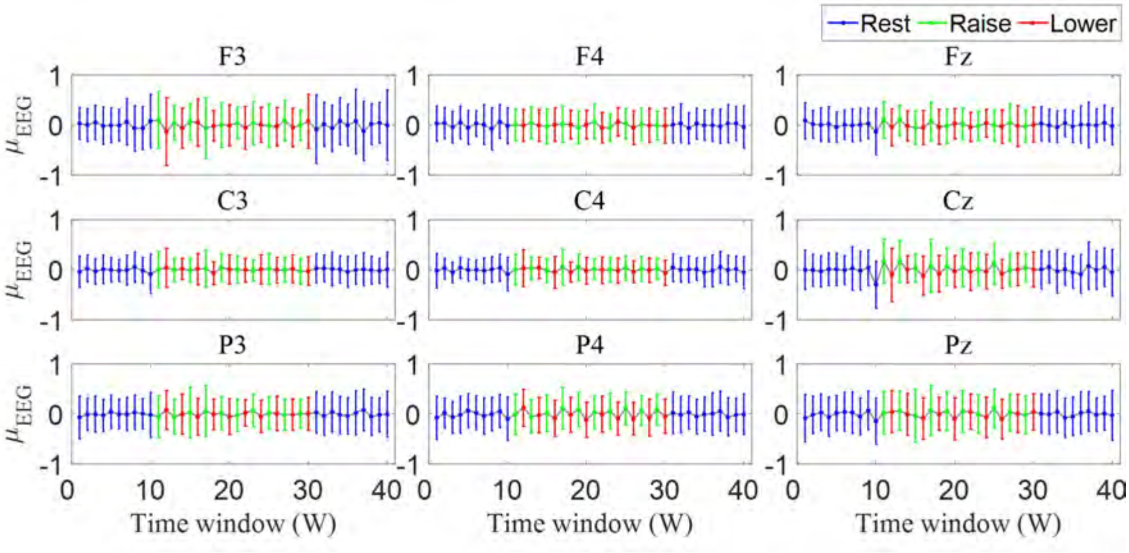

Figure 4.4: Mean and standard deviations of the EEG signal calculated between eight subjects and ten trials, for nine electrodes during Task 1.

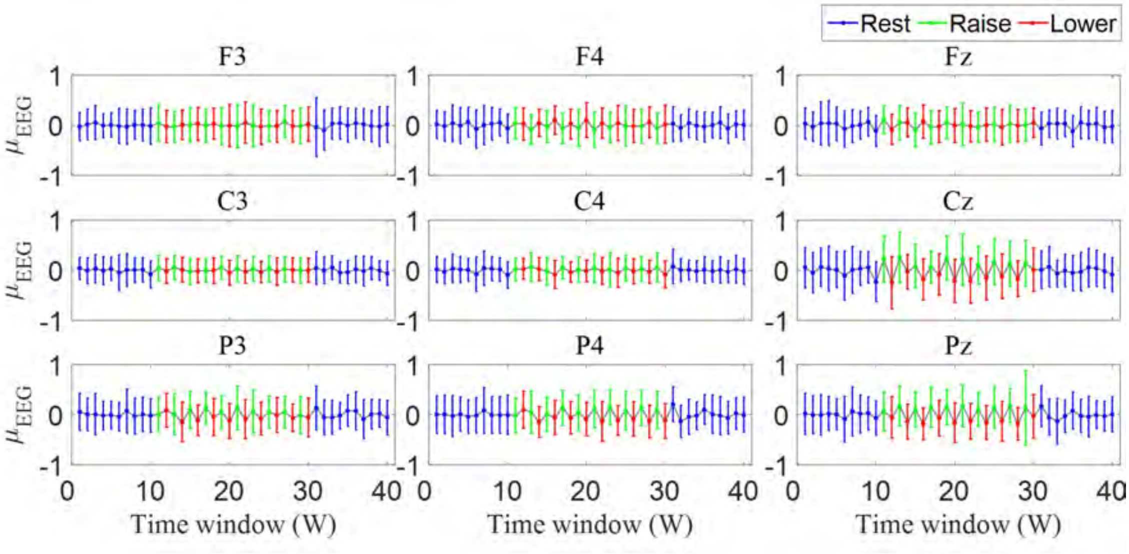

Figure 4.5: Mean and standard deviations of the EEG signal calculated between eight subjects and ten trials, for nine electrodes during Task 2.

4.1.2 Correlation dimension

For each window, an embedding dimension was calculated using the false nearest neighbor algorithm, which in the case an embedding dimension was not found, the value was limited to 10, as the saturation mentioned in [50, 51]. As for the optimal delay, the average mutual information algorithm was used with 20 bins, in order to be proportional to the simple cubic root of the number of samples. For these reasons, each window had its own parameters for the calculation of the CD. Afterwards, their mean and standard deviation (μ_{CD} and σ_{CD}) were calculated and can be seen in Figures 4.6 and 4.7 for Task 1 and Task 2, respectively.

4.1.3 Largest Lyapunov exponent

Similar to the previous indices, each time window of samples had its own LLE calculated. According to the CD results, the dimension of the underlying system lies between 4 and 6, therefore a dimension of 5 was chosen to calculate the LLE with a delay coordinate of one sample. Then, the means and standard deviations (μ_{LLE} and σ_{LLE}) between subjects and trials were calculated, for nine electrodes and 40 time windows. These can be seen in Figures 4.8 and 4.9 for Task 1 and Task 2, respectively.

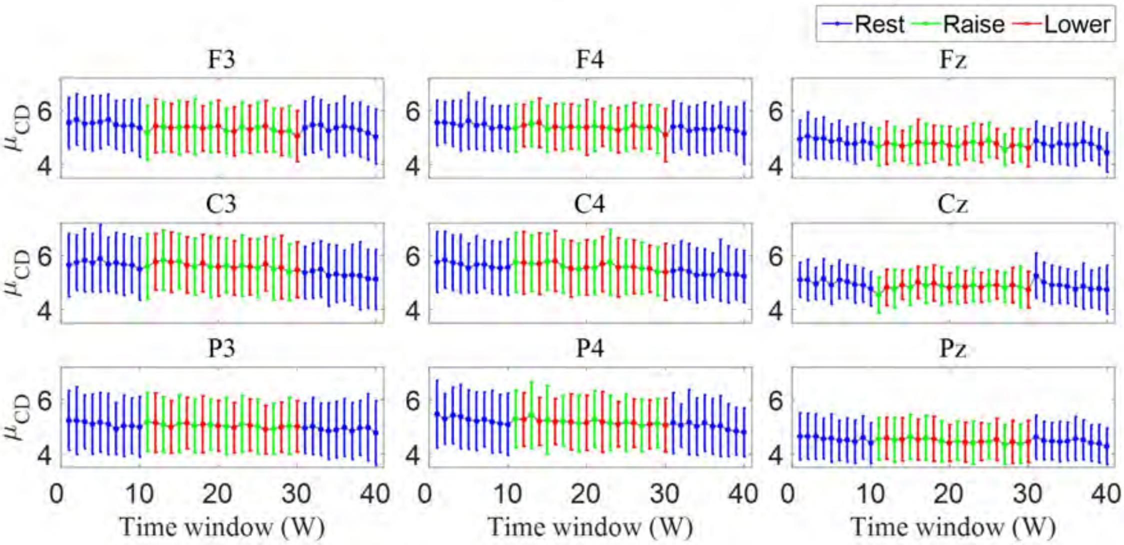

Figure 4.6: Mean and standard deviations of CD calculated between eight subjects and ten trials, for nine electrodes during Task 1.

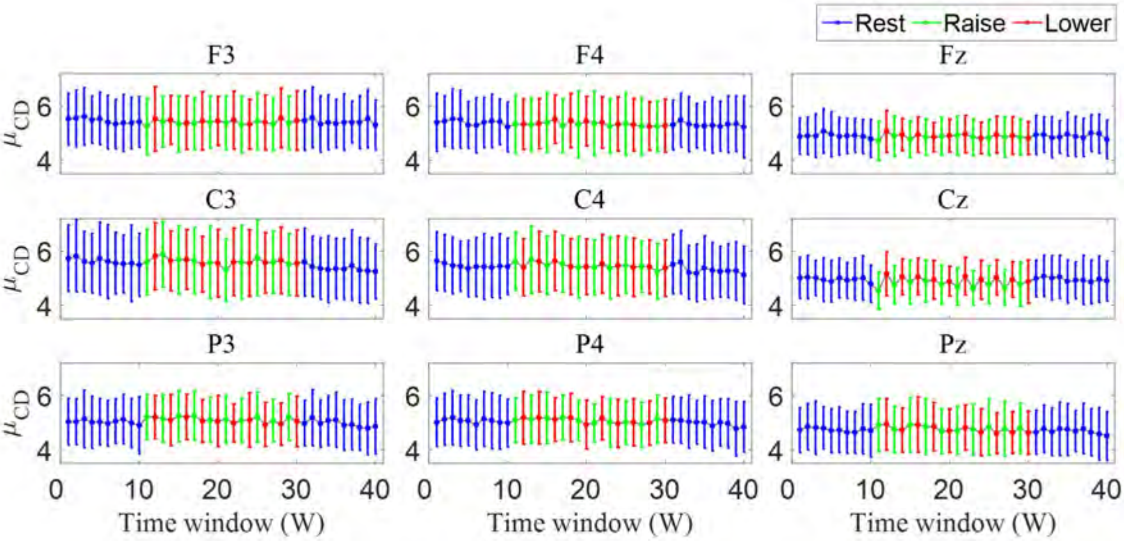

Figure 4.7: Mean and standard deviations of CD calculated between eight subjects and ten trials, for nine electrodes during Task 2.

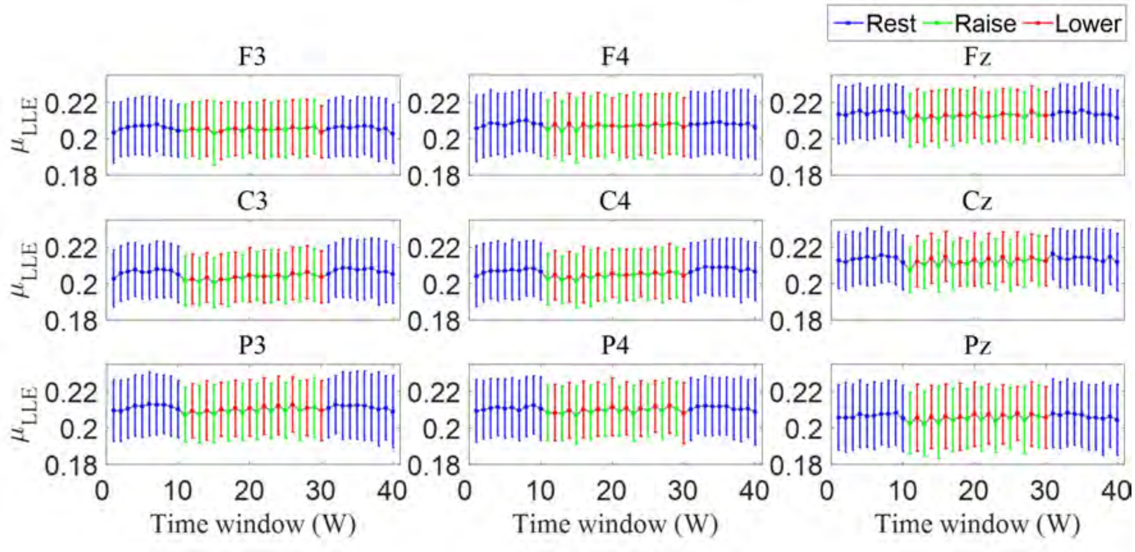

Figure 4.8: Mean and standard deviations of LLE calculated between eight subjects and ten trials, for nine electrodes during Task 1.

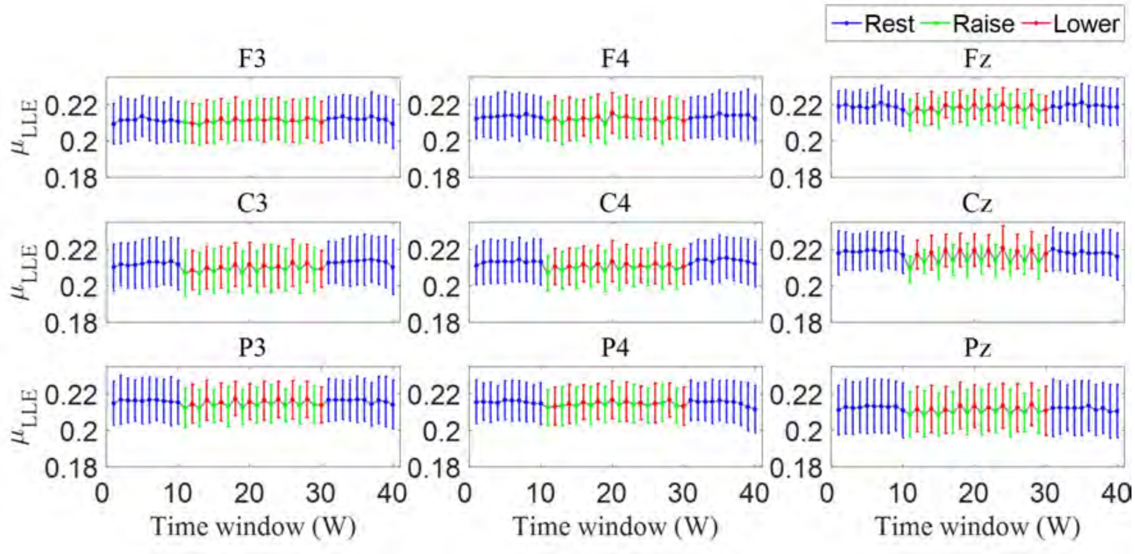

Figure 4.9: Mean and standard deviations of LLE calculated between eight subjects and ten trials, for nine electrodes during Task 2.

4.2 PARAMETRIC ADJUSTMENT FOR ASYNCHRONOUS PROTOCOLS

A parameter tuning was performed in order to obtain a better decoding of the joint angles of the asynchronous protocols. This parameter tuning consisted of three parts. One part was to analyze different cortical regions of the brain by selecting different electrode arrays from the acquired EEG signal. Another part consisted of analyzing how far in the past the number of samples should be taken in consideration. The final part for the tuning consisted of considering the mentioned evaluation metrics in Section 2.2.3 to see the different behaviors and performances of the chosen parameters.

In this work, the linear optimum filter described in Section 2.2.1 was adapted into the following MLR

$$x[t] = a + \sum_{n=1}^{N} \sum_{k=1}^{L} b_{nk} S_n[t - G * k], \tag{4.3}$$

where $x[t]$ is the decoded variable at time t, S_n is the voltage measured at electrode n, N are the number of channels, L are the number of lags, G is the gap between lags, and a and b are the weights of the linear regression. The process (4.3), for a single time sample, can also be viewed in the following matrix form:

$$x = \begin{bmatrix} S_1 & S_2 & \cdots & S_{NL} \end{bmatrix} \begin{bmatrix} b_1 \\ b_2 \\ \vdots \\ b_{NL} \end{bmatrix} + a \tag{4.4}$$

where NL is the number of electrodes times the number of lags.

To analyze the different regions of the brain during the asynchronous protocols described in Section 3.2, different electrode arrays from the EEG were evaluated, thus varying N. This led to selecting 42 arrays, that can be seen in Figure 4.10, where colors define the combinations of regions on the scalp and each color possess six sets of electrodes. Also different time windows prior to the decoded variable were analyzed. This was done by changing the gap G, since the lags were fixed to

$L = 10$. By changing gaps, the time window was limited to reach up to 5 seconds into the past, by increments of 0.5 s.

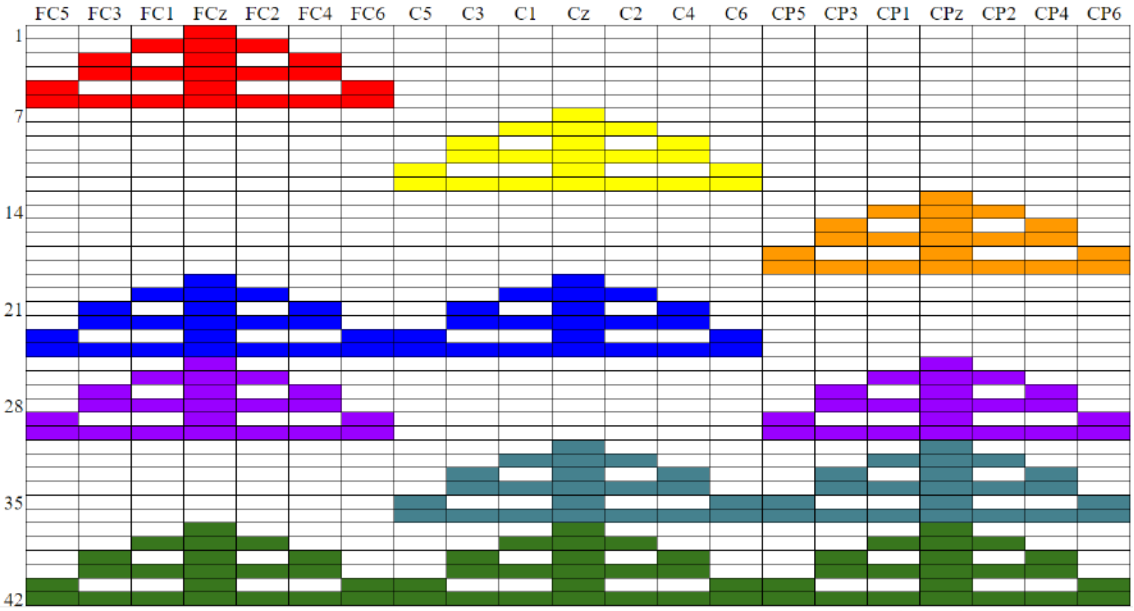

	FC5	FC3	FC1	FCz	FC2	FC4	FC6	C5	C3	C1	Cz	C2	C4	C6	CP5	CP3	CP1	CPz	CP2	CP4	CP6
1				■																	
			■	■	■																
		■		■		■															
		■	■	■	■	■															
	■			■			■														
	■	■	■	■	■	■	■														
7											■										
										■	■	■									
									■		■		■								
									■	■	■	■	■								
								■			■			■							
								■	■	■	■	■	■	■							
																		■			
14																	■	■	■		
																■		■		■	
																■	■	■	■	■	
															■			■			■
															■	■	■	■	■	■	■
				■							■										
			■	■	■					■	■	■									
21		■		■		■			■		■		■								
		■	■	■	■	■			■	■	■	■	■								
	■			■			■	■			■			■							
	■	■	■	■	■	■	■	■	■	■	■	■	■	■							
				■														■			
			■	■	■												■	■	■		
		■		■		■										■		■		■	
28		■	■	■	■	■										■	■	■	■	■	
	■			■			■								■			■			■
	■	■	■	■	■	■	■								■	■	■	■	■	■	■
											■							■			
										■	■	■					■	■	■		
									■		■		■			■		■		■	
									■	■	■	■	■			■	■	■	■	■	
35								■			■			■	■			■			■
								■	■	■	■	■	■	■	■	■	■	■	■	■	■
				■							■							■			
			■	■	■					■	■	■					■	■	■		
		■		■		■			■		■		■			■		■		■	
		■	■	■	■	■			■	■	■	■	■			■	■	■	■	■	
	■			■			■	■			■			■	■			■			■
42	■	■	■	■	■	■	■	■	■	■	■	■	■	■	■	■	■	■	■	■	■

Figure 4.10: 42 electrode array combinations used in the experimental setup from Section 3.2, represented in a binary table using 21 electrodes, namely FC5, FC3, FC1, FCz, FC2, FC4, FC6, C5, C3, C1, Cz, C2, C4, C6, CP5, CP3, CP1, CPz, CP2, CP4, and CP6. Colors define the combinations of regions on the scalp: red for FC, yellow for C, orange for CP, blue for FC-C, purple for FC-CP, and green for FC-C-CP.

To obtain the regressors values of (4.4) for the different combinations of electrodes arrays and time delays, the following matrices had to be created:

$$\mathbf{S} = \begin{bmatrix} 1 & S_{1,1} & S_{1,2} & \cdots & S_{1,NL} \\ 1 & S_{2,1} & S_{2,2} & \cdots & S_{2,NL} \\ \vdots & \vdots & \vdots & \ddots & \vdots \\ 1 & S_{\mathrm{TS},1} & S_{\mathrm{TS},2} & \cdots & S_{\mathrm{TS},NL} \end{bmatrix}, \quad \text{and} \quad \mathbf{x} = \begin{bmatrix} x_1 \\ x_2 \\ \vdots \\ x_{\mathrm{TS}} \end{bmatrix}, \tag{4.5}$$

where the first column of $\mathbf{S}$ is the constant value to obtain the intercept regressor, i.e., value a for (4.3) and (4.4), and TS are the different values of training samples, which depend on the quantity of samples available after varying the G values. To obtain the regressors, such matrices can be used as in (2.36) as follows:

$$\beta = [\mathbf{S}^T\mathbf{S}]^{-1}\mathbf{S}^T\mathbf{x}, \tag{4.6}$$

where β is the weight vector $[a,\ b_1,\ ...,\ b_{NL}]$.

Out of the nine subjects stated in Section 3.2, four healthy (A05, A06, B11, and B12) and five with SCI (C06, C07, C08, C09, and C10), only eight of the data sets were chosen to perform the decodification, since subject C10 reported to had felt tired during the sessions [106]. Each test subject performed six runs, where the first five runs were concatenated to create the corresponding training models of $\mathbf{S}$ and $\mathbf{x}$. The run number six was used as the testing model. The training models counted with $180,000$ samples (1200 Hz for 30 s for 5 trials) by electrode. However, as was previously mentioned, the matrices (4.5) varied in size, from using one electrode ($N = 1$) with a delay of 0.5 s (600 samples) ($NL = 10$ and $\mathrm{TS} = 179,400$) to using 21 electrodes ($N = 21$) with a delay of 5 s (6000 samples) ($NL = 210$ and $\mathrm{TS} = 174,000$). The performances of the 42 electrode arrays, and 10 delays can be seen in Figure 4.11 for the CC values. Figure 4.12 has the performance of the NRMSE values, and Figure 4.13 for the SNR values.

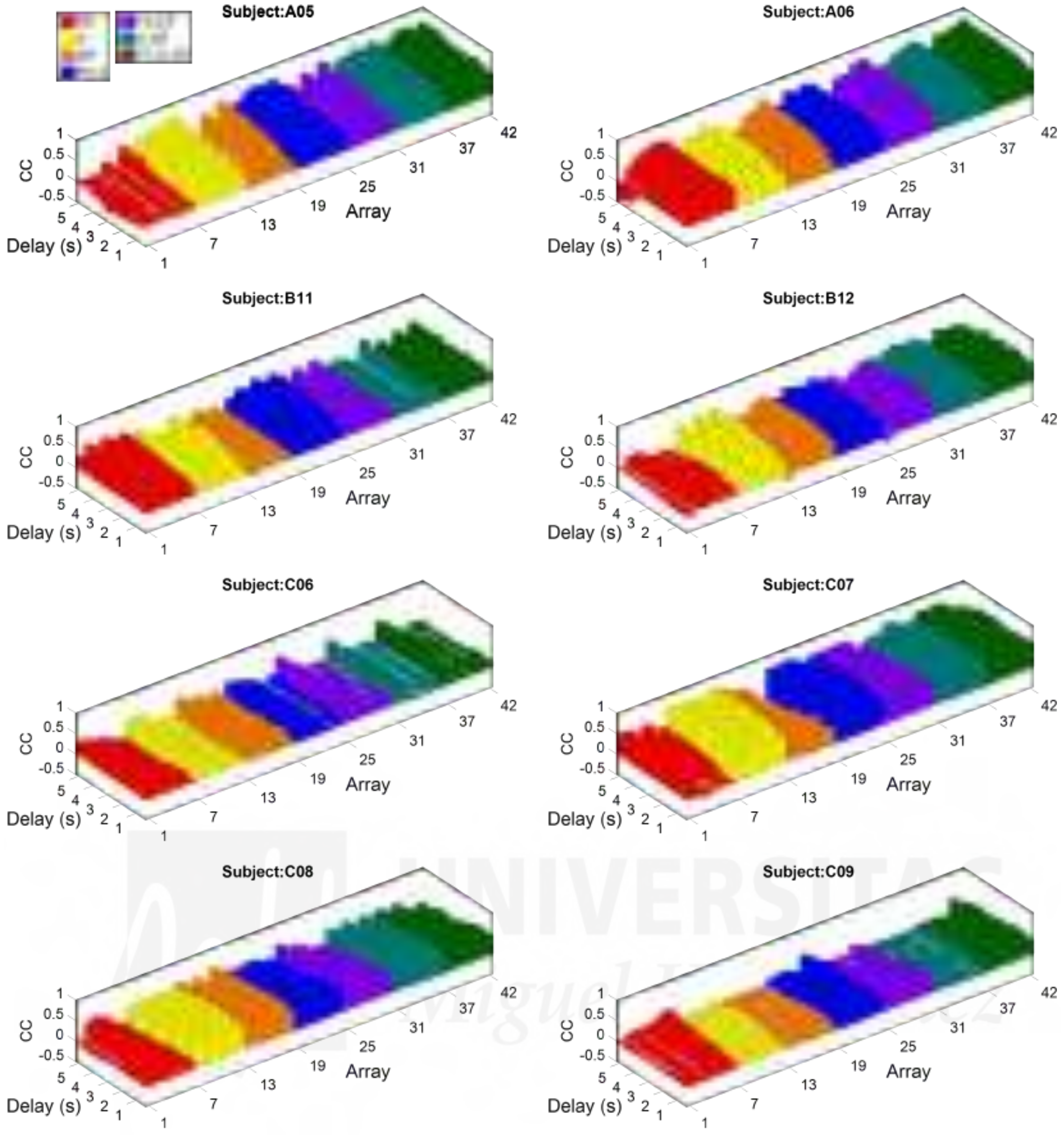

Figure 4.11: Correlation coefficient (CC) values for eight subjects, arranged in 42 arrays by 10 delays in the past, ranged from 0.5 s to 5 s. Colors represent the different cortical regions seen in Figure 4.10.

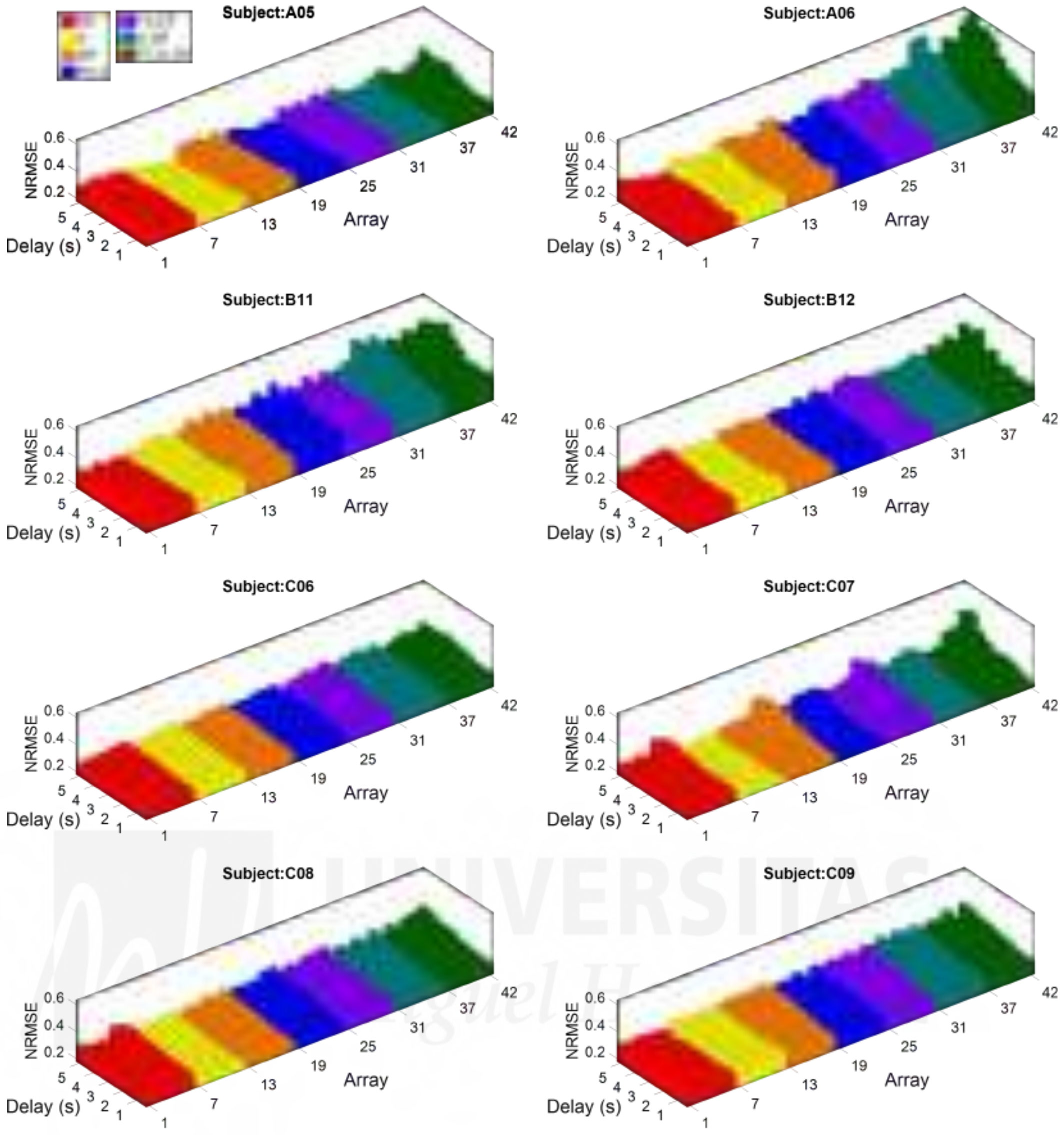

Figure 4.12: Normalized root mean square error (NRMSE) values for eight subjects, arranged in 42 arrays by 10 delays in the past, ranged from 0.5 s to 5 s. Colors represent the different cortical regions seen in Figure 4.10.

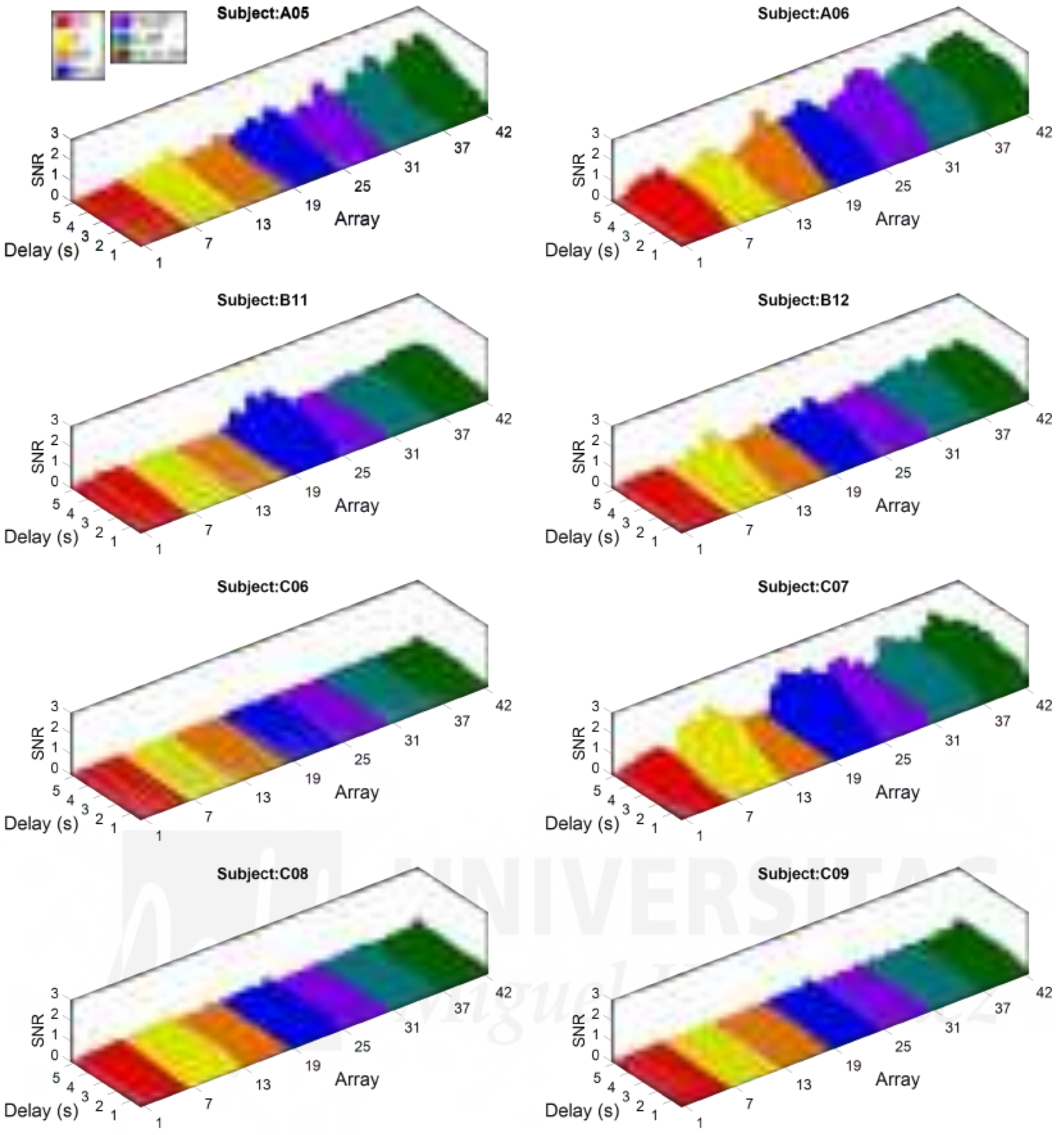

Figure 4.13: Signal-to-noise ratio (SNR) values for eight subjects, arranged in 42 arrays by 10 delays in the past, ranged from 0.5 s to 5 s. Colors represent the different cortical regions seen in Figure 4.10.

The three parts of the parametric tuning chosen for the decodification performance led to 420 sets, with the 42 electrode arrays and 10 delays, using three metrics for the eight selected subjects. In order to establish which set is the most appropriate, the metrics were arranged by subject from best to worst. When considering the best 10% of all the sets, the mode among the subjects in the CC and NRMSE values were the sets of 138, 264, and 348, which repeated for 4 subjects. As for the mode of the SNR values, they were 376 and 420, for 7 subjects. When considering the top ten best of all the sets, the mode of CC and NRMSE values

Set	Array #	Delay(s)
138	12	2
180	12	2.5
264	12	3.5
294	42	3.5
348	12	4.5
376	40	4.5
420	42	5

Table 4.1: Combinations of sets with their respective electrode array and time delay.

were the sets of 180 and 348. However, they only repeated in 3 subjects. The mode of the SNR was the set of 294, repeating 4 subjects. The corresponding electrode arrays and time delays of these mentioned sets are shown in Table 4.1.

Looking at these modes, the selected array considered to have better performance in CC and NRMSE is array number 12, i.e., all electrodes of the cortical region C. Regarding the modes of the SNR, the most appropriate array is number 42, i.e., all electrodes of the cortical regions FC, C, and CP. With respect to the time delays, it varied according to the subjects, ranging from 2 s to 4.5 s in the past. In this case, the time delay of 3.5 s in the past was considered as it represented the middle area of the time delay range.

Based on these selections, array number 12 has $N = 7$ electrodes, and the time delay of 3.5 s (4200 samples) in the past with a sampling frequency of 1200 Hz lets $\text{TS} = 175,800$ samples for training. Thus having the following matrices:

$$\mathbf{S} = \begin{bmatrix} 1 & S_{1,1} & S_{1,2} & \cdots & S_{1,70} \\ 1 & S_{2,1} & S_{2,2} & \cdots & S_{2,70} \\ \vdots & \vdots & \vdots & \ddots & \vdots \\ 1 & S_{175800,1} & S_{175800,2} & \cdots & S_{175800,70} \end{bmatrix}, \quad \text{and} \quad \mathbf{x} = \begin{bmatrix} x_1 \\ x_2 \\ \vdots \\ x_{175800} \end{bmatrix},$$

applied to (4.6). This grants the vector β with the weights $a \in \mathbb{R}$ and $b \in \mathbb{R}^{1\times 70}$. These weights are applied to (4.4) in order to obtain the variable x for the testing run, for the t samples. Figure 4.14 shows these decodifications of the asynchronous protocols, where the actual joint velocity of the knee is compared to its respective decoded variable.

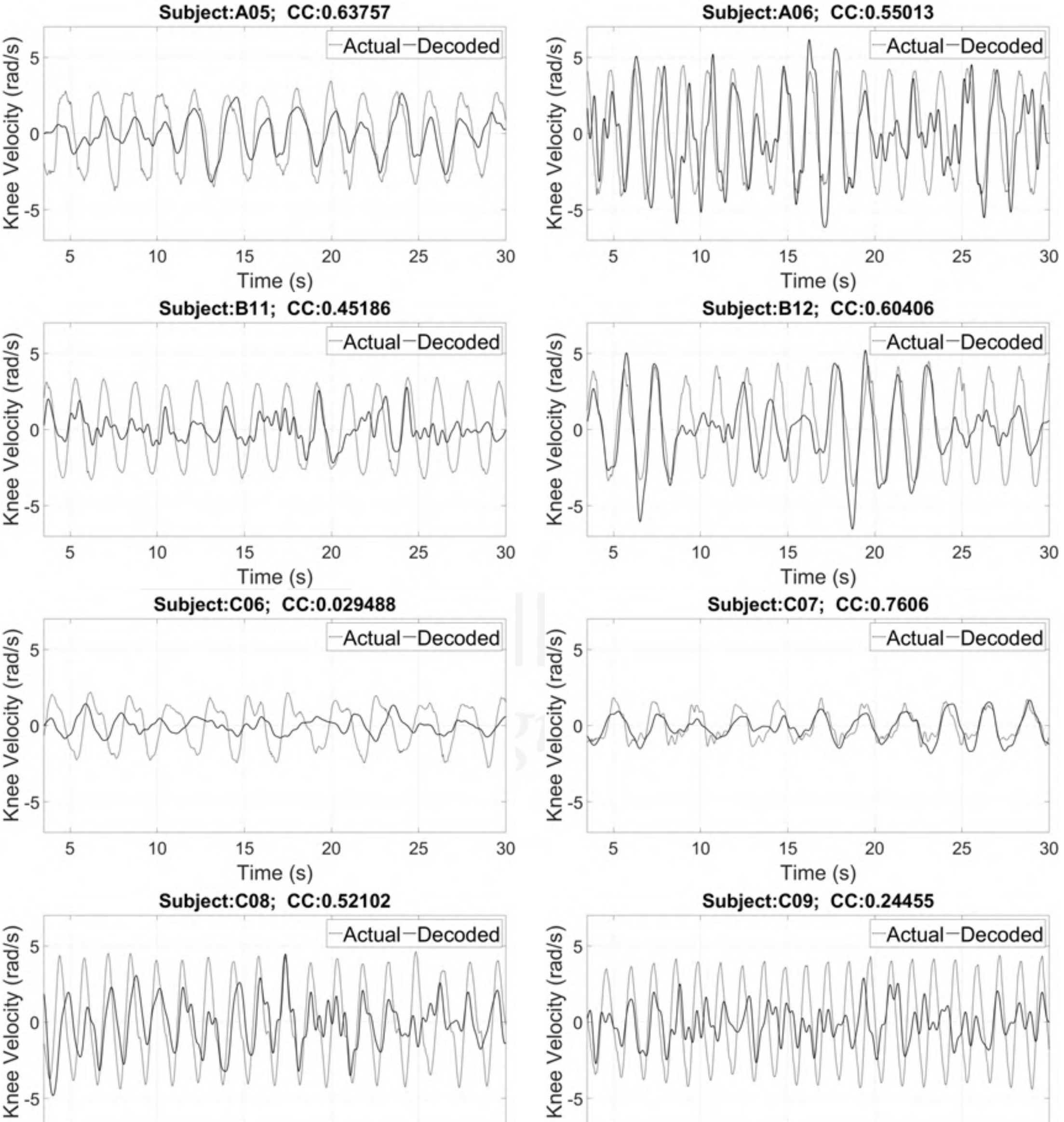

Figure 4.14: Plots of the actual joint velocity of the knee (dotted line) compared to their decodification (solid line) of eight subjects. These MLR decodifications were performed with array 12 (7 electrodes) and a time delay of 3.5 s.

4.3 Decodification by segments

As mentioned in Chapter 3, the literature has usually shown a continuous trajectory reconstruction of cycled tasks, like walking or free repetitive movement of the limbs, similar to the protocol described in Section 3.2. However, the protocol described in Section 3.1, displayed in Figures 3.2 and 3.3, has a single task divided into different activities. In this particular case the activities were rest, raise, and lower the limb. With this notion, it was proposed to perform decodifications for each activity separately, by segmentation of the data, as shown in Figure 4.1.

As stated, the subjects performed two type of tasks: raising the foot (Task 1) and the knee (Task 2) while remaining seated. In this work different decoders were created, described next. Decoder 1 (D1) used a single MLR equation to decode all the trial involving the three activities of resting, raising, and lowering. Decoder 2 (D2) used a pair of transitioning MLR equations, one for the resting periods, and another for the movement period. Decoder 3 (D3) used three MLR equations, one for the resting periods, and two separate decoders for raising and lowering of the movement periods. This can be visualized in Figure 4.15.

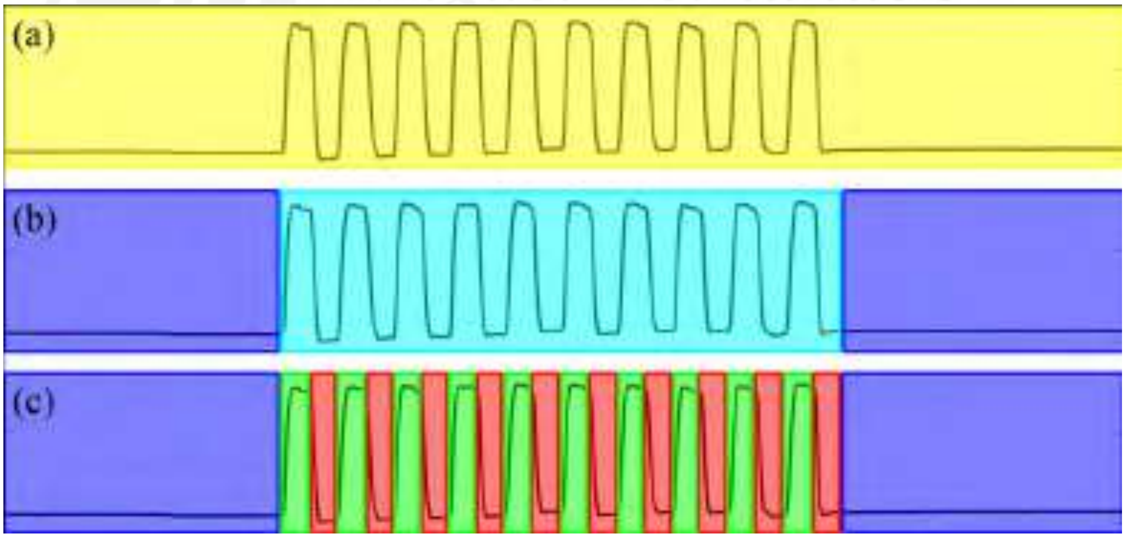

Figure 4.15: Illustrative sections for which a MLR equation was created: (a) Decoder 1 (D1) where yellow corresponds to a single MLR equation for all activities, (b) Decoder 2 (D2) where blue corresponds to resting periods, and cyan to the movement period, (c) Decoder 3 (D3) where blue corresponds to resting periods, green for the raising, and red for the lowering period.

Three trials of each test subject were used for training to obtain the decoder, and one trial was used for testing. Similar to the process described previously in Section 4.2, equation (4.3) was implemented, or equivalently its matrix form (4.4). However, since in this occasion there were two joint angles to decode, i.e., the hip and the knee angles, the training portion of the decoder was performed with the MLR equation. After the training was finished, the testing portion of this study was realized using the multivariate linear regression. As mentioned in Section 2.2.1, a multivariate linear regression is used when there are multiple correlated dependent variables predicted, rather than a single variable. Therefore, for the testing portion, (4.4) expands to:

$$\begin{bmatrix} x_1 & x_2 \end{bmatrix} = \begin{bmatrix} S_1 & S_2 & \cdots & S_{NL} \end{bmatrix} \begin{bmatrix} b_{1,1} & b_{1,2} \\ b_{2,1} & b_{2,2} \\ \vdots & \vdots \\ b_{NL,1} & b_{NL,2} \end{bmatrix} + \begin{bmatrix} a_1 & a_2 \end{bmatrix} \tag{4.7}$$

where x are the decoded variables, S is the voltage measured at electrodes N and L number of lags, and a and b are the weights of the linear regression. In the case of the synchronous protocols, it was stated in Section 3.1.2 that two data sets were considered for this study. The first data set, which consisted of nine electrodes, was considered for the first decodification by segments. Also, as the results shown in the Section 4.2, the chosen delay for the decodification was established to be 3.5 s into the past.

To obtain the regressors values of (4.7) for the two joint angles, the following matrices had to be created:

$$\mathbf{S} = \begin{bmatrix} 1 & S_{1,1} & S_{1,2} & \cdots & S_{1,NL} \\ 1 & S_{2,1} & S_{2,2} & \cdots & S_{2,NL} \\ \vdots & \vdots & \vdots & \ddots & \vdots \\ 1 & S_{\mathrm{TS},1} & S_{\mathrm{TS},2} & \cdots & S_{\mathrm{TS},NL} \end{bmatrix}, \quad \text{and} \quad \mathbf{x} = \begin{bmatrix} x_{1,1} & x_{1,2} \\ x_{2,1} & x_{2,2} \\ \vdots & \vdots \\ x_{\mathrm{TS},1} & x_{\mathrm{TS},2} \end{bmatrix}, \tag{4.8}$$

where the first column of $\mathbf{S}$ is the constant value for the intercept regressor, i.e., value a for (4.3) and (4.4), and TS are the different values of training samples, which depend on the quantity of samples available after varying the G values. Another value that affected TS, for the synchronous protocols, was a sub-sampling performed during the creation of the training model (and the testing model). Due to the high number of samples, a sub-sampling of the available data allowed to obtain a smaller matrix. Sampling by increments of 10, assisted the dimensions of the training matrices $\mathbf{S}$ and $\mathbf{x}$, reducing TS from $349,500$ to $34,950$. After the training models were created, to obtain the regressors, such matrices can be used as in (2.36) in the following manner:

$$\beta_{Knee} = [\mathbf{S}^T\mathbf{S}]^{-1}\mathbf{S}^T\mathbf{x}_1, \quad \text{and} \qquad \beta_{Hip} = [\mathbf{S}^T\mathbf{S}]^{-1}\mathbf{S}^T\mathbf{x}_2, \tag{4.9}$$

where $\mathbf{x}_1$ and $\mathbf{x}_2$ are the columns of $\mathbf{x}$, and β is composed of the weight vectors $a \in \mathbb{R}^{2\times 1}$ and $b \in \mathbb{R}^{2\times NL}$.

The selected metrics to evaluate the performance of the decodifications were the metrics mentioned in Section 2.2.3. The performance of the three decoders, i.e., D1, D2, and D3, for eight subjects can be seen in Tables 4.2 to 4.4. It can be seen that in general, the performance turns better when more decoders are applied. It can also be appreciated in the average between subjects. Figures 4.16 to 4.23 show the decodifications of Task 1 for the hip and knee joint angles of the eight subjects, and Figures 4.24 to 4.31 display the decodifications for Task 2. It is worth to mention that a different test trial of the same subject was used for further validation of each created decoder. Such additional test trials had the same improved performance when more decoders were used.

CC	Task 1					
Subject	Hip decoders			Knee decoders		
	D1	D2	D3	D1	D2	D3
1	0.2360	0.9038	0.9017	0.4003	0.8002	0.9365
2	0.5895	0.5954	0.6021	0.3493	0.7534	0.9405
3	0.2857	0.7221	0.8518	0.2883	0.7418	0.8447
4	0.3513	0.0736	0.0499	0.4777	0.8212	0.8987
5	0.1795	0.4448	0.4072	0.2252	0.6442	0.9101
6	0.3888	0.7776	0.8927	0.4089	0.7747	0.9076
7	0.2397	0.4574	0.4625	0.1951	0.7298	0.8503
8	0.0154	0.2635	0.5325	-0.0343	0.4933	0.8169
μ	0.2857	0.5298	0.5876	0.2888	0.7198	0.8882
σ	0.1674	0.2762	0.2933	0.1619	0.1059	0.0454
	Task 2					
Subject	Hip decoders			Knee decoders		
	D1	D2	D3	D1	D2	D3
1	0.2614	0.7249	0.8625	0.2483	0.7743	0.8229
2	0.5416	0.8841	0.9109	0.2664	0.4980	0.5162
3	0.4182	0.8341	0.8895	0.4164	0.8351	0.8830
4	0.4746	0.7977	0.9095	0.2830	0.4568	0.5809
5	0.3996	0.7563	0.8955	0.3879	0.7405	0.8571
6	0.4541	0.8060	0.9155	0.4134	0.7990	0.8999
7	0.2657	0.7073	0.8889	0.2689	0.7242	0.8855
8	0.5032	0.8560	0.9315	0.4872	0.8267	0.8976
μ	0.4148	0.7958	0.9005	0.3465	0.7068	0.7929
σ	0.1035	0.0626	0.0210	0.0902	0.1471	0.1538

Table 4.2: Correlation coefficient (CC) values of the decodifications of the hip and knee angles for eight subjects and their mean and standard deviations for Tasks 1 and 2. D1, D2, and D3 stand for the decoder used.

NRMSE	Task 1					
Subject	Hip decoders			Knee decoders		
	D1	D2	D3	D1	D2	D3
1	0.3002	0.1511	0.1571	0.3513	0.2313	0.1354
2	0.1400	0.1428	0.1446	0.3501	0.2422	0.1267
3	0.3352	0.2434	0.1910	0.3488	0.2441	0.2027
4	0.1444	0.1701	0.1751	0.3445	0.2250	0.1727
5	0.1251	0.1166	0.1220	0.3679	0.2882	0.1569
6	0.3346	0.2349	0.1736	0.3422	0.2404	0.1644
7	0.7408	0.7306	0.7416	0.3729	0.2731	0.2288
8	0.5766	0.5792	0.5740	0.4179	0.3485	0.2279
μ	0.3371	0.2961	0.2849	0.3619	0.2616	0.1769
σ	0.2212	0.2293	0.2354	0.0251	0.0410	0.0392
	Task 2					
Subject	Hip decoders			Knee decoders		
	D1	D2	D3	D1	D2	D3
1	0.3719	0.2761	0.2136	0.3795	0.2847	0.2740
2	0.2688	0.1488	0.1354	0.2658	0.2479	0.2594
3	0.3244	0.1980	0.1647	0.2755	0.1681	0.1517
4	0.3176	0.2278	0.1587	0.2871	0.2897	0.2740
5	0.3212	0.2374	0.1609	0.2509	0.1861	0.1431
6	0.2681	0.1814	0.1276	0.2984	0.2241	0.1921
7	0.3493	0.2561	0.1694	0.3378	0.2434	0.1691
8	0.3078	0.1841	0.1298	0.2646	0.1713	0.1332
μ	0.3161	0.2137	0.1575	0.2949	0.2269	0.1996
σ	0.0357	0.0428	0.0280	0.0434	0.0481	0.0604

Table 4.3: Normalized root mean square error (NRMSE) values of the decodifications of the hip and knee angles for eight subjects and their mean and standard deviations for Tasks 1 and 2. D1, D2, and D3 stand for the decoder used.

SNR	Task 1					
Subject	Hip decoders			Knee decoders		
	D1	D2	D3	D1	D2	D3
1	0.0980	4.8191	5.1885	0.3147	2.2031	7.8723
2	0.8171	1.0110	1.1626	0.3465	1.6110	7.9651
3	0.1486	1.3825	3.4224	0.1475	1.3757	3.2322
4	0.1388	0.3000	0.3437	0.2810	2.2336	4.2457
5	0.1165	0.5124	0.5786	0.1518	0.9493	4.8824
6	0.1488	1.6534	3.9935	0.2458	1.8538	5.4486
7	0.1332	0.6836	1.0774	0.0841	1.2675	3.4362
8	0.2792	0.6691	1.2934	0.1133	0.5976	2.2429
μ	0.2350	1.3789	2.1325	0.2106	1.5114	4.9157
σ	0.2415	1.4613	1.8063	0.0989	0.5802	2.1024
	Task 2					
Subject	Hip decoders			Knee decoders		
	D1	D2	D3	D1	D2	D3
1	0.2655	1.6725	3.7560	0.2244	1.8709	2.8454
2	0.6229	3.5816	5.6095	0.3753	0.6800	1.0456
3	0.1933	1.9889	4.0166	0.2400	2.5279	4.3702
4	0.5853	2.5493	5.7744	0.6088	1.0664	1.4345
5	0.3463	1.9669	4.9028	0.2899	1.6731	3.4213
6	0.3511	2.1779	5.4153	0.2439	1.8248	3.8605
7	0.1408	1.1869	4.4749	0.1432	1.2915	4.3675
8	0.2436	2.5197	6.5461	0.2125	1.7586	3.8268
μ	0.3436	2.2055	5.0620	0.2922	1.5867	3.1465
σ	0.1758	0.7108	0.9489	0.1441	0.5657	1.2802

Table 4.4: Signal-to-noise ratio (SNR) values of the decodifications of the hip and knee angles for eight subjects and their mean and standard deviations for Tasks 1 and 2. D1, D2, and D3 stand for the decoder used.

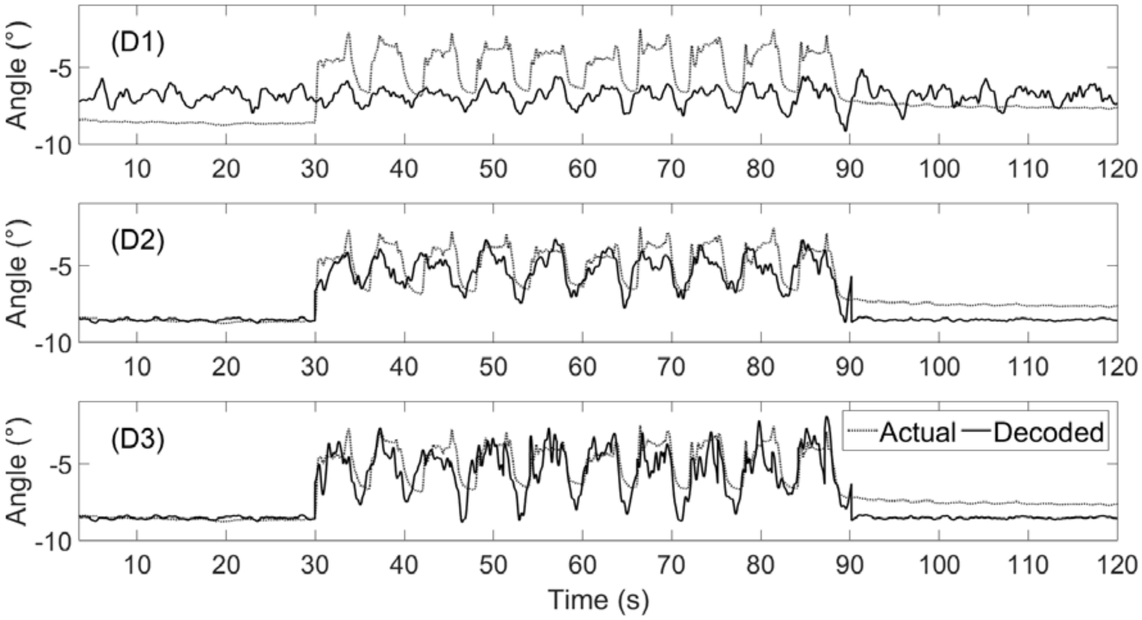

(a) Hip angles decoded using three decoders for Subject 1 during Task 1.

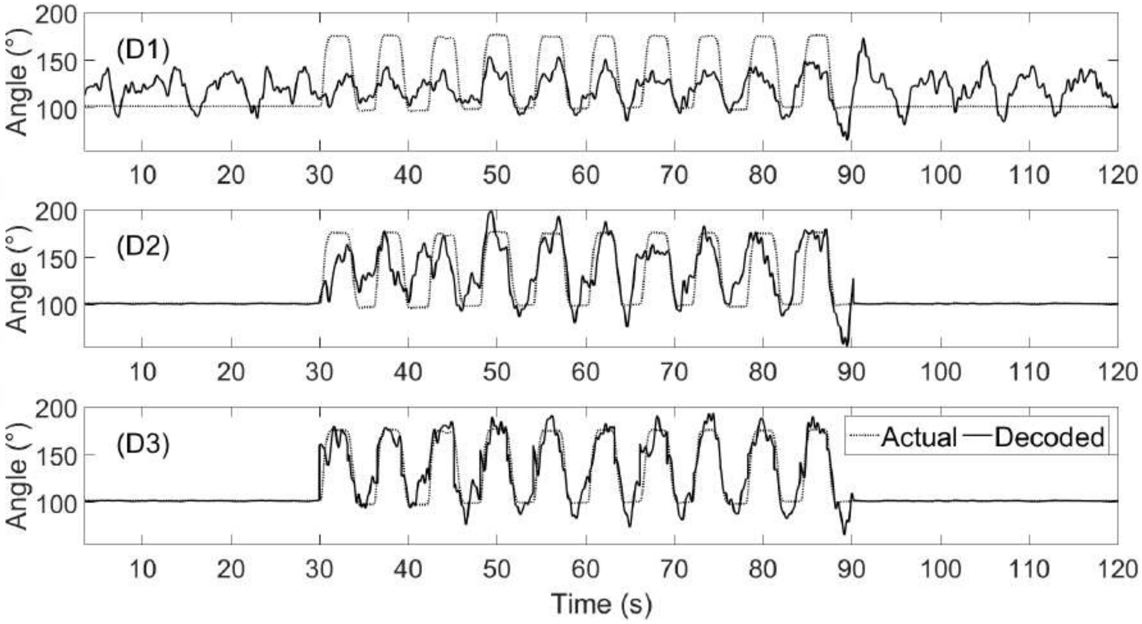

(b) Knee angles decoded using three decoders for Subject 1 during Task 1.

Figure 4.16: Graphs of the actual hip and knee joint angles (dotted line) compared to their decodification (solid line). These decodifications were performed with a time delay of 3.5 s. For each sub-figure from top to bottom: D1, D2, and D3.

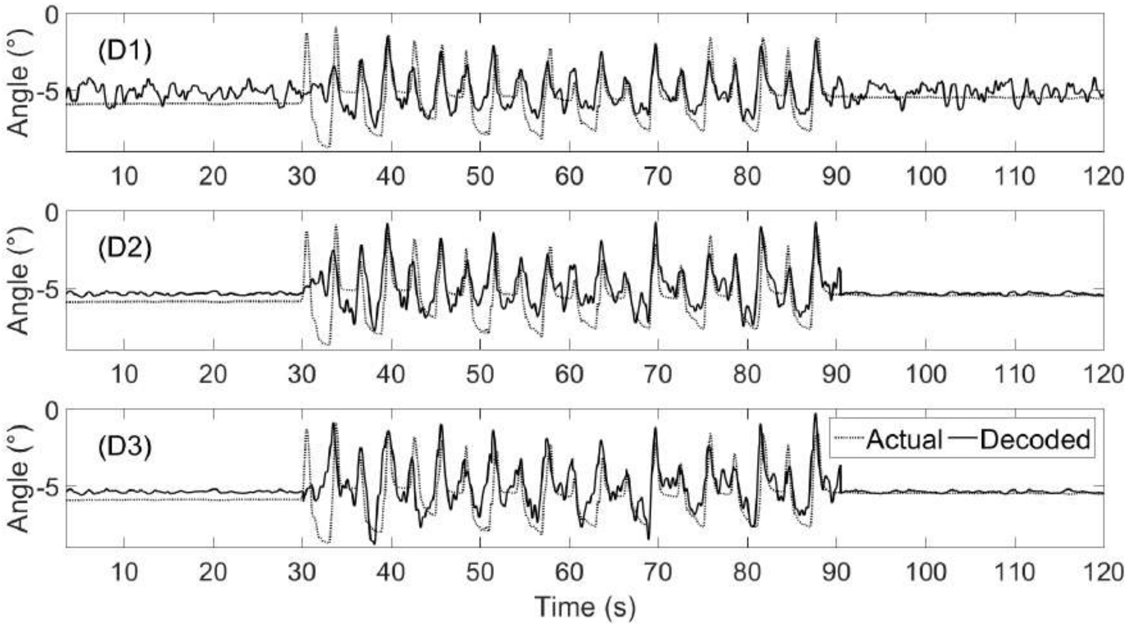

(a) Hip angles decoded using three decoders for Subject 2 during Task 1.

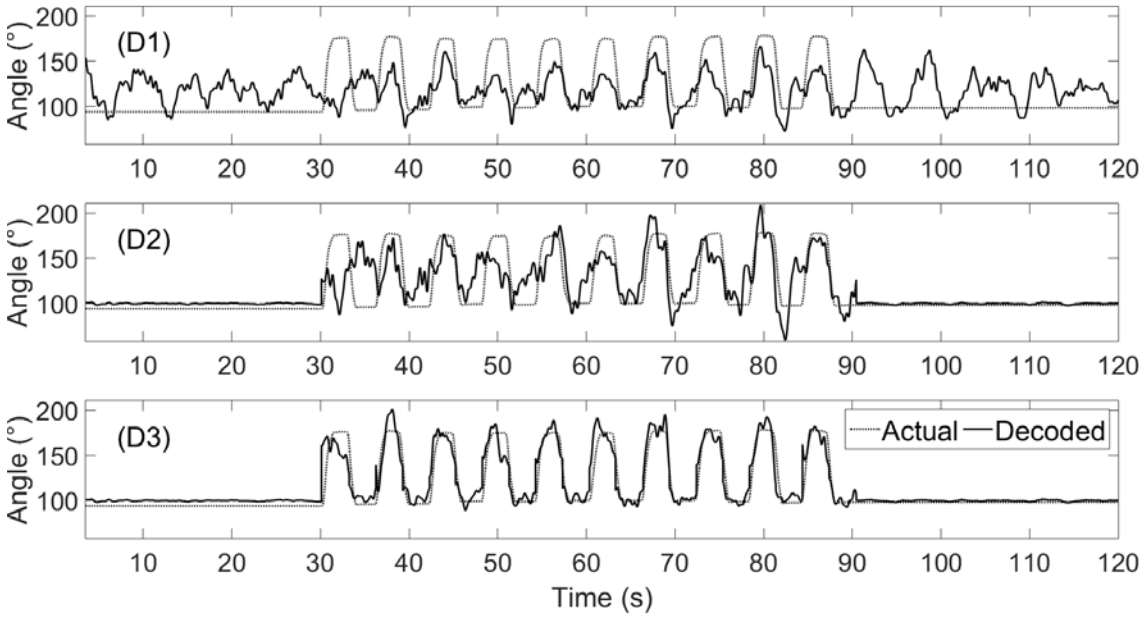

(b) Knee angles decoded using three decoders for Subject 2 during Task 1.

Figure 4.17: Graphs of the actual hip and knee joint angles (dotted line) compared to their decodification (solid line). These decodifications were performed with a time delay of 3.5 s. For each sub-figure from top to bottom: D1, D2, and D3.

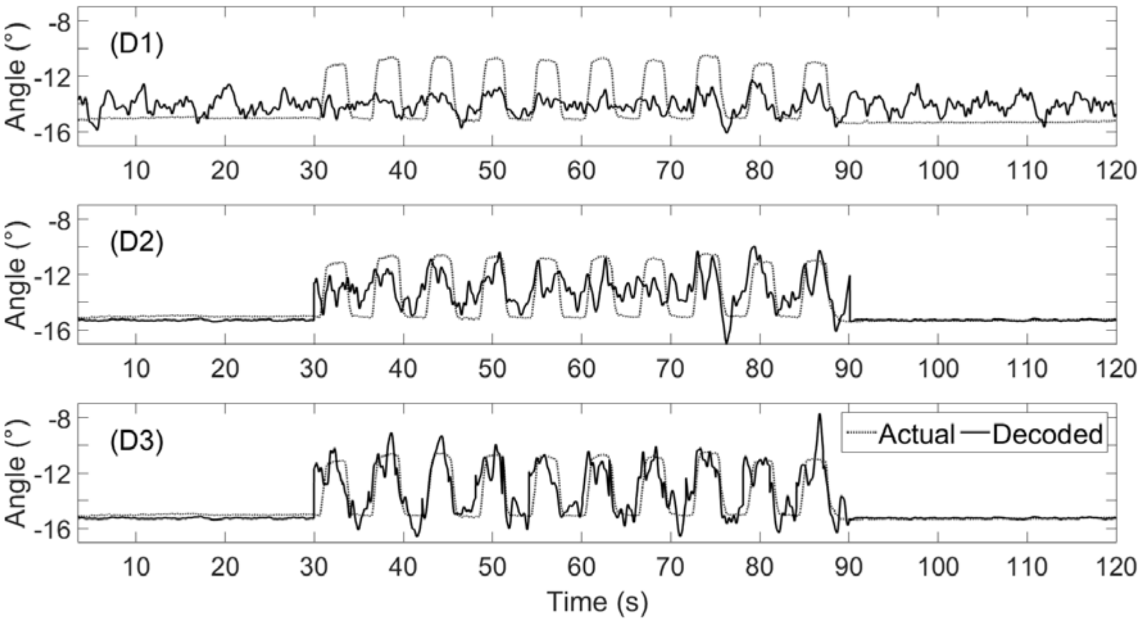

(a) Hip angles decoded using three decoders for Subject 3 during Task 1.

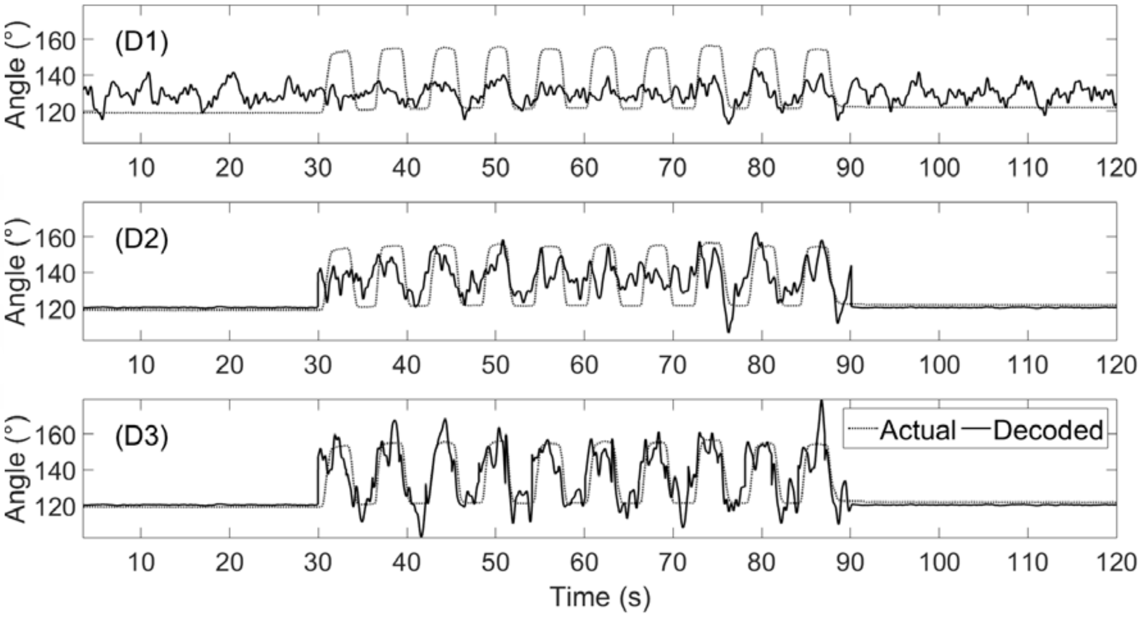

(b) Knee angles decoded using three decoders for Subject 3 during Task 1.

Figure 4.18: Graphs of the actual hip and knee joint angles (dotted line) compared to their decodification (solid line). These decodifications were performed with a time delay of 3.5 s. For each sub-figure from top to bottom: D1, D2, and D3.

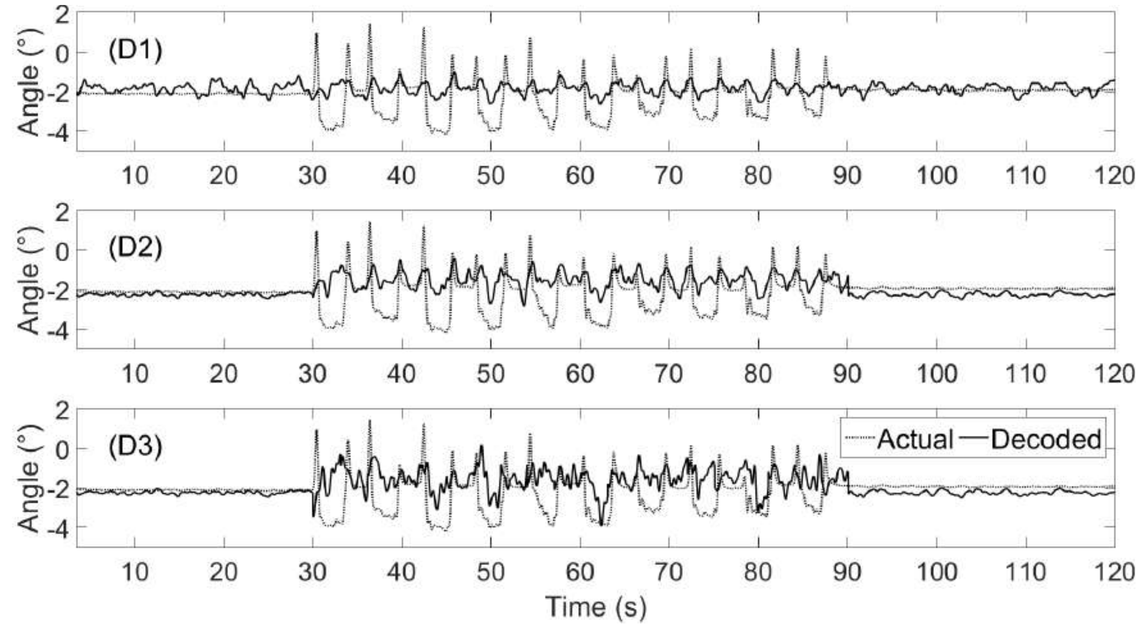

(a) Hip angles decoded using three decoders for Subject 4 during Task 1.

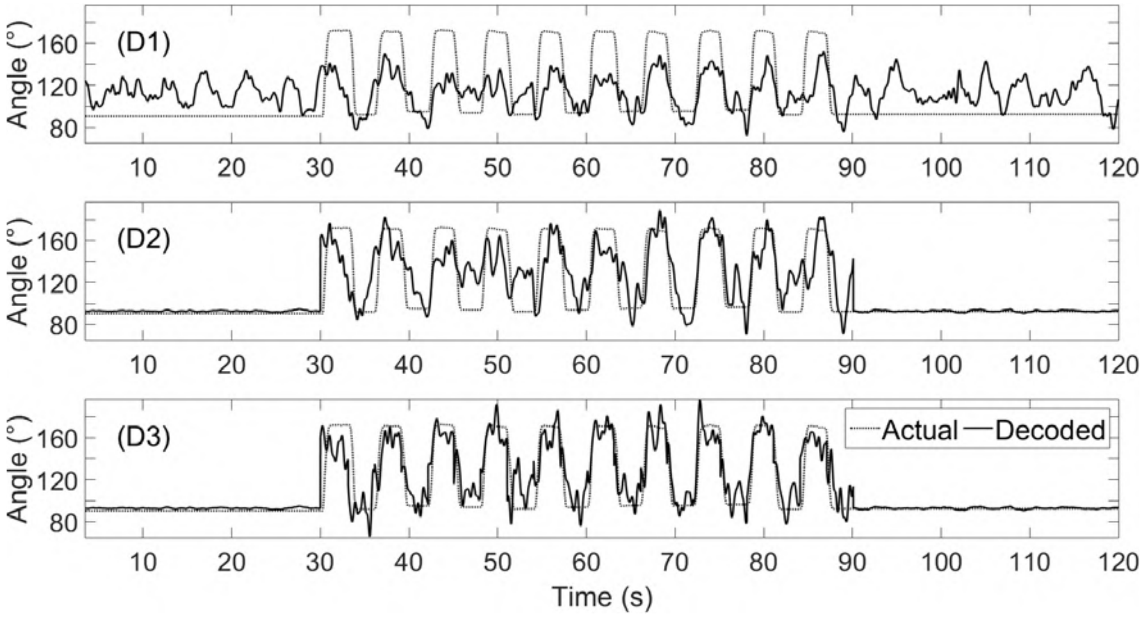

(b) Knee angles decoded using three decoders for Subject 4 during Task 1.

Figure 4.19: Graphs of the actual hip and knee joint angles (dotted line) compared to their decodification (solid line). These decodifications were performed with a time delay of 3.5 s. For each sub-figure from top to bottom: D1, D2, and D3.

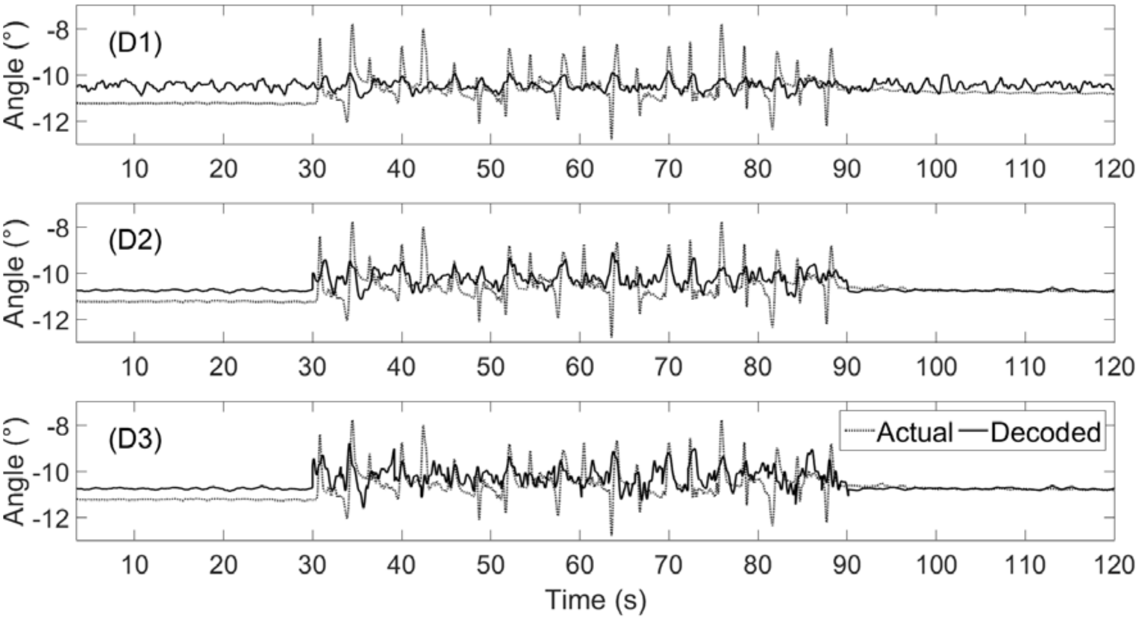

(a) Hip angles decoded using three decoders for Subject 5 during Task 1.

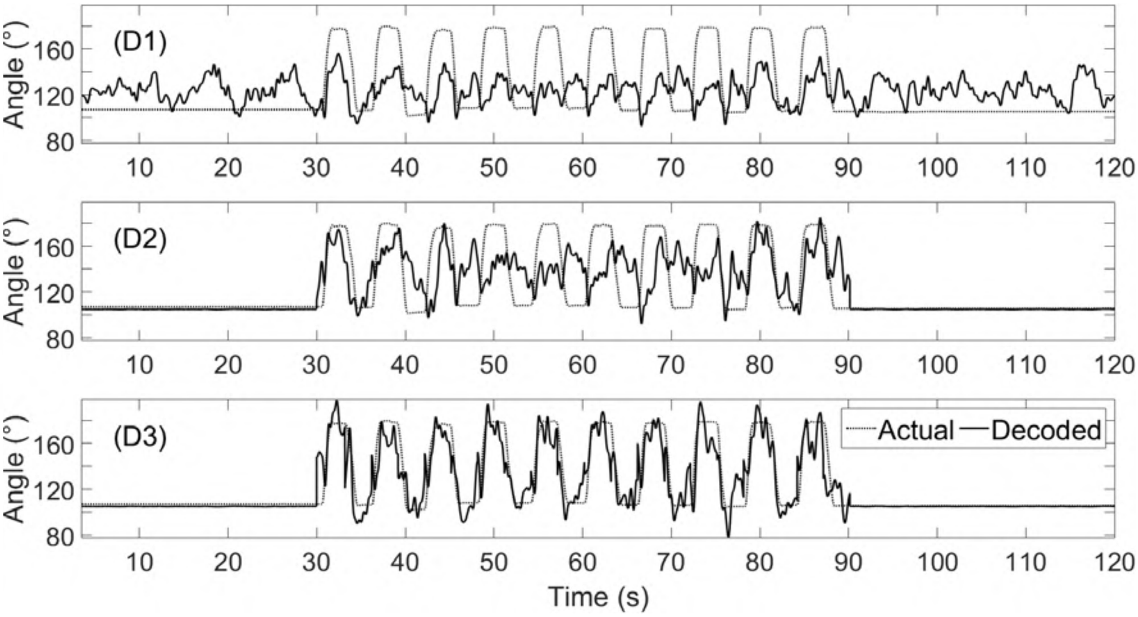

(b) Knee angles decoded using three decoders for Subject 5 during Task 1.

Figure 4.20: Graphs of the actual hip and knee joint angles (dotted line) compared to their decodification (solid line). These decodifications were performed with a time delay of 3.5 s. For each sub-figure from top to bottom: D1, D2, and D3.

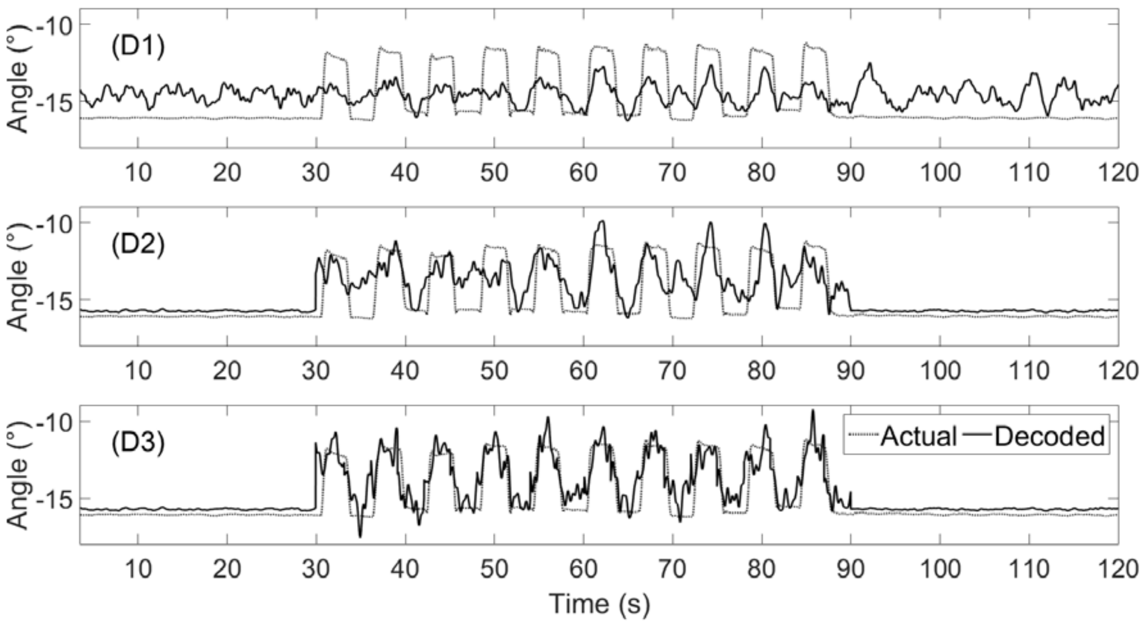

(a) Hip angles decoded using three decoders for Subject 6 during Task 1.

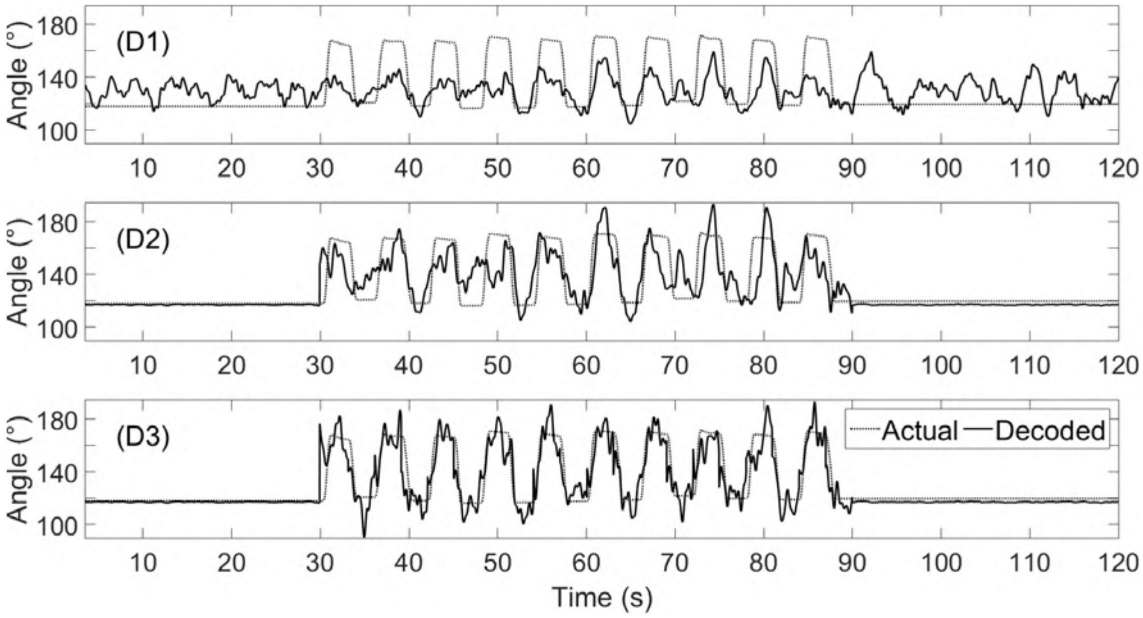

(b) Knee angles decoded using three decoders for Subject 6 during Task 1.

Figure 4.21: Graphs of the actual hip and knee joint angles (dotted line) compared to their decodification (solid line). These decodifications were performed with a time delay of 3.5 s. For each sub-figure from top to bottom: D1, D2, and D3.

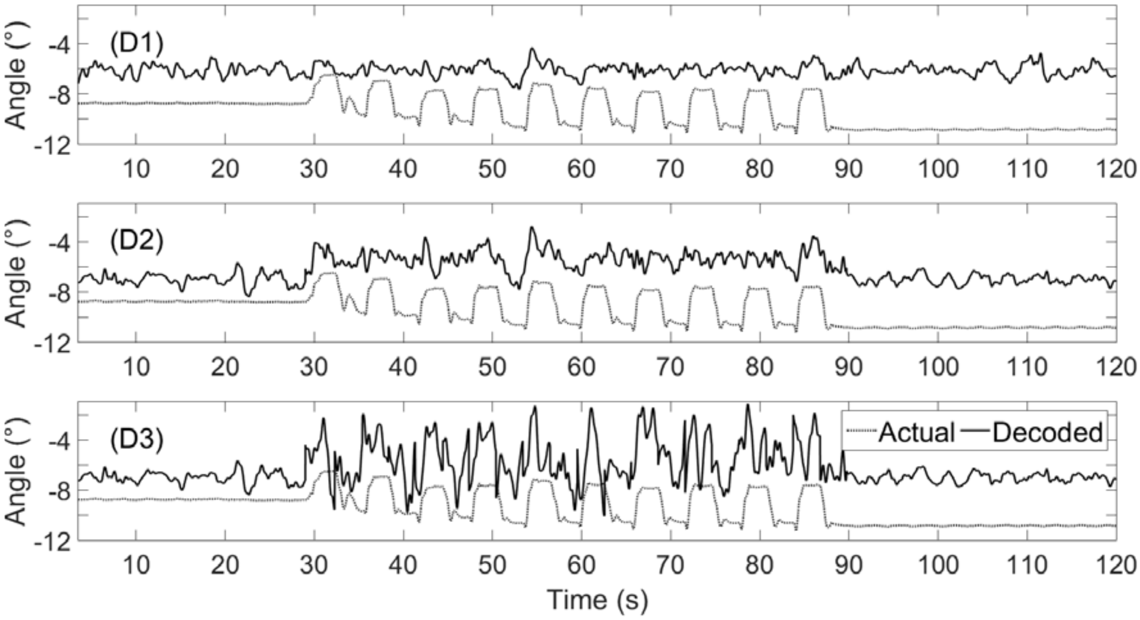

(a) Hip angles decoded using three decoders for Subject 7 during Task 1.

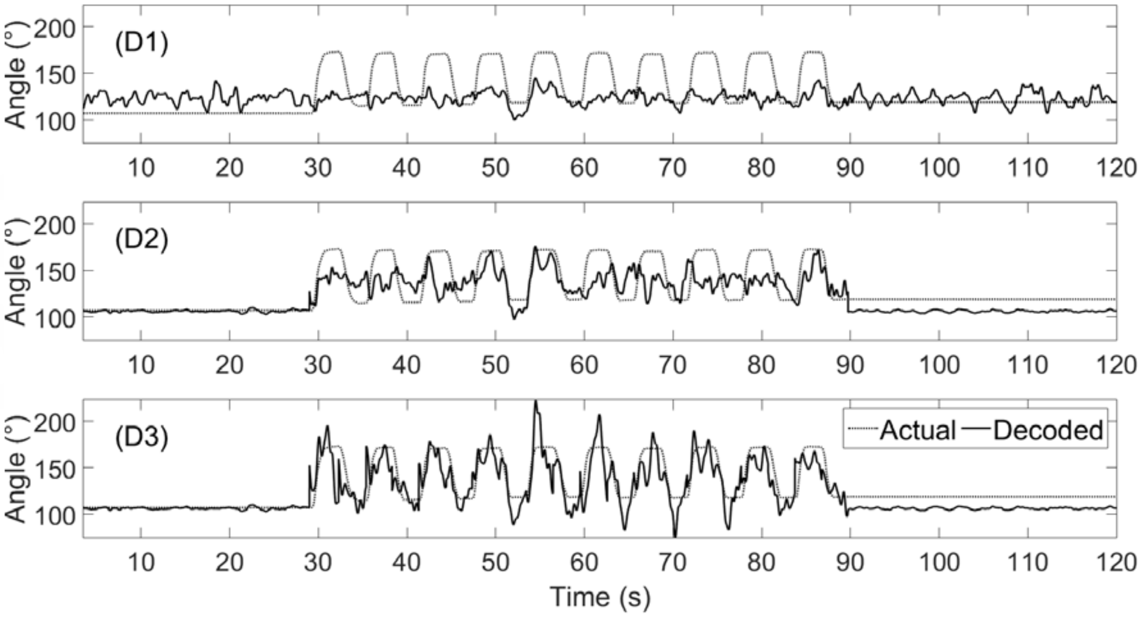

(b) Knee angles decoded using three decoders for Subject 7 during Task 1.

Figure 4.22: Graphs of the actual hip and knee joint angles (dotted line) compared to their decodification (solid line). These decodifications were performed with a time delay of 3.5 s. For each sub-figure from top to bottom: D1, D2, and D3.

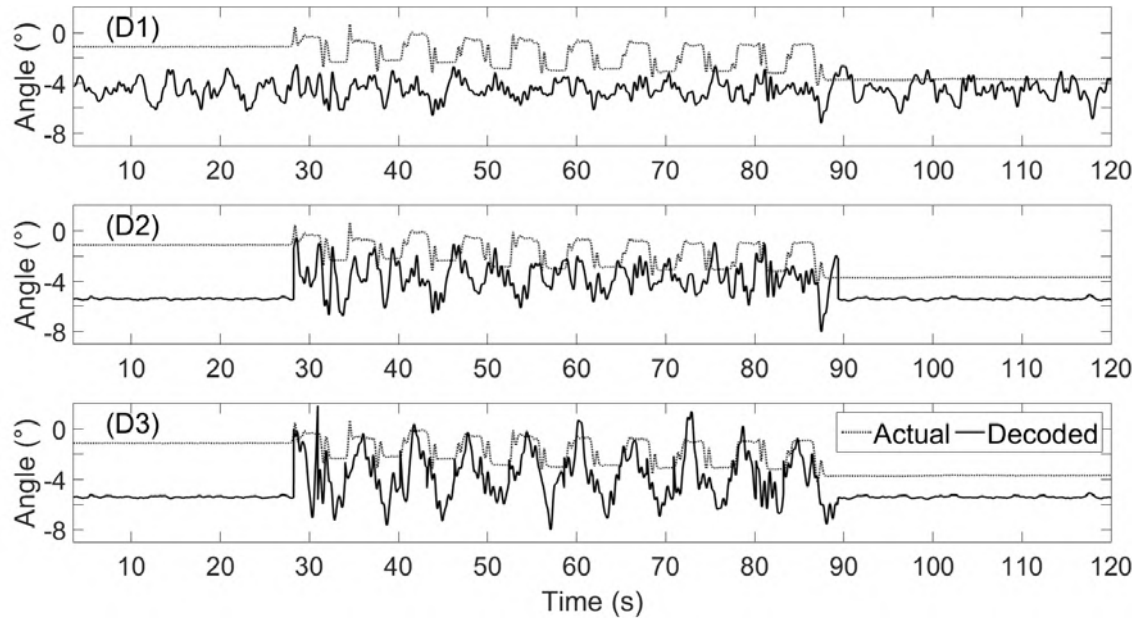

(a) Hip angles decoded using three decoders for Subject 8 during Task 1.

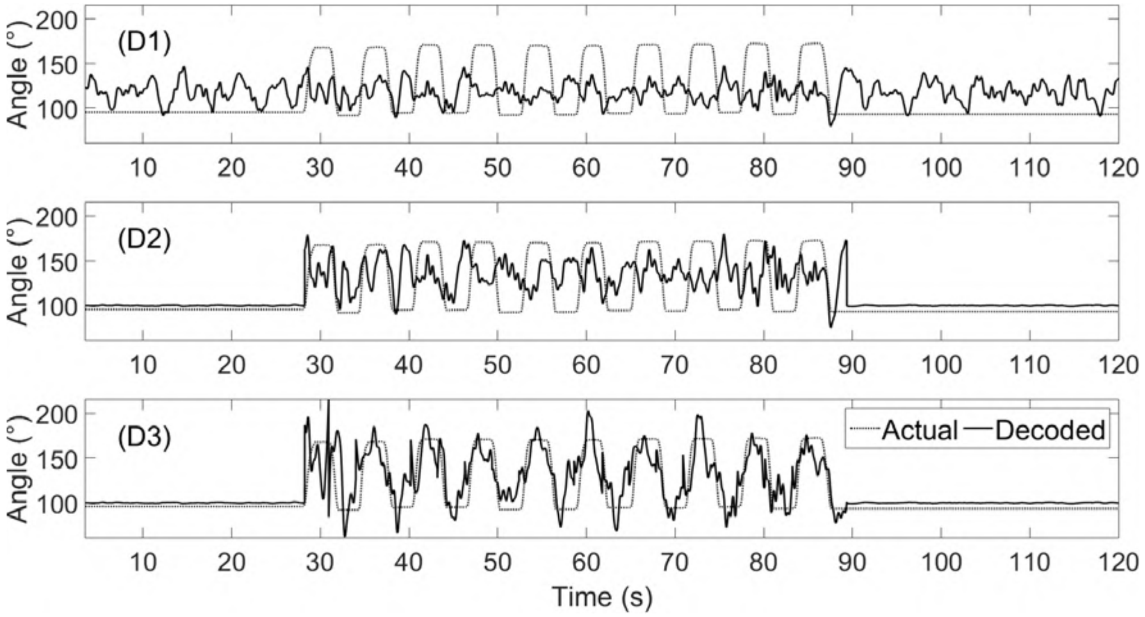

(b) Knee angles decoded using three decoders for Subject 8 during Task 1.

Figure 4.23: Graphs of the actual hip and knee joint angles (dotted line) compared to their decodification (solid line). These decodifications were performed with a time delay of 3.5 s. For each sub-figure from top to bottom: D1, D2, and D3.

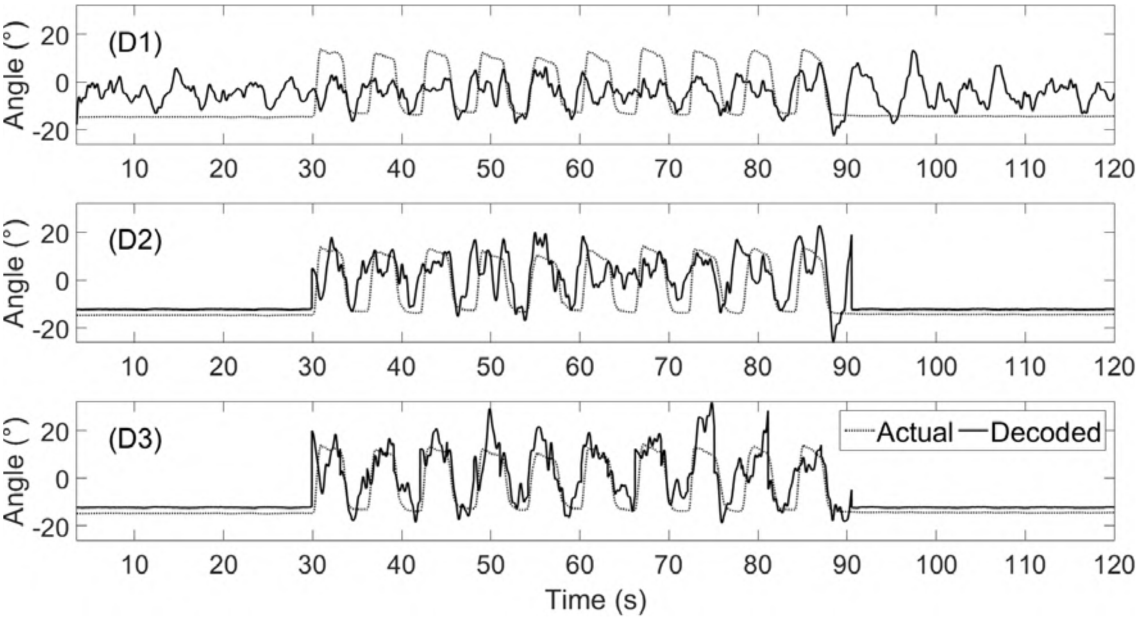

(a) Hip angles decoded using three decoders for Subject 1 during Task 2.

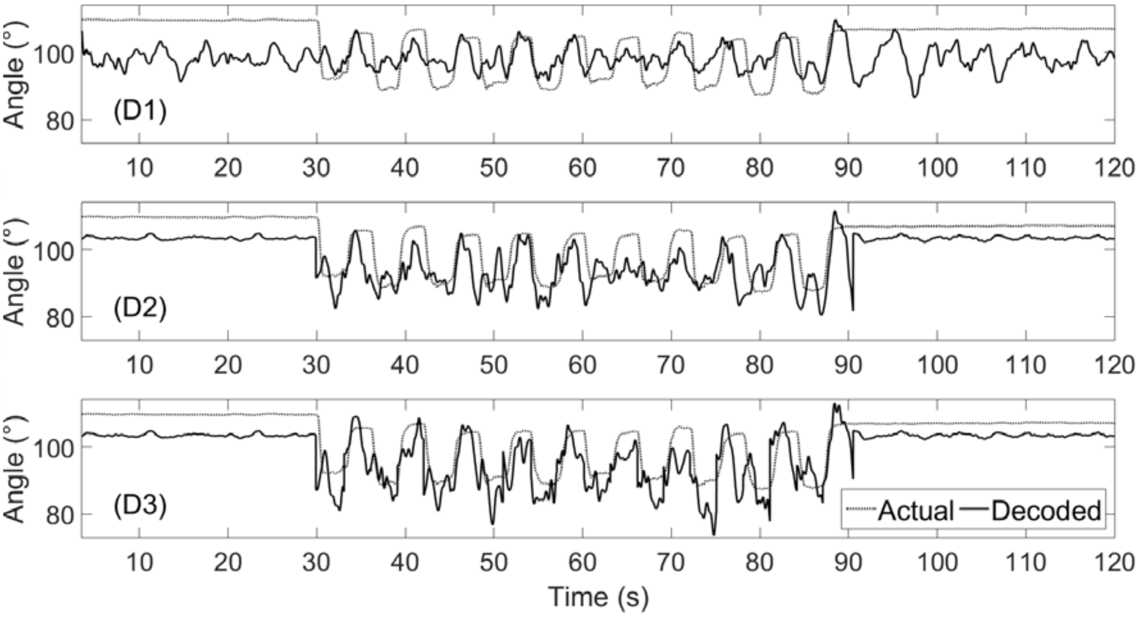

(b) Knee angles decoded using three decoders for Subject 1 during Task 2.

Figure 4.24: Graphs of the actual hip and knee joint angles (dotted line) compared to their decodification (solid line). These decodifications were performed with a time delay of 3.5 s. For each sub-figure from top to bottom: D1, D2, and D3.

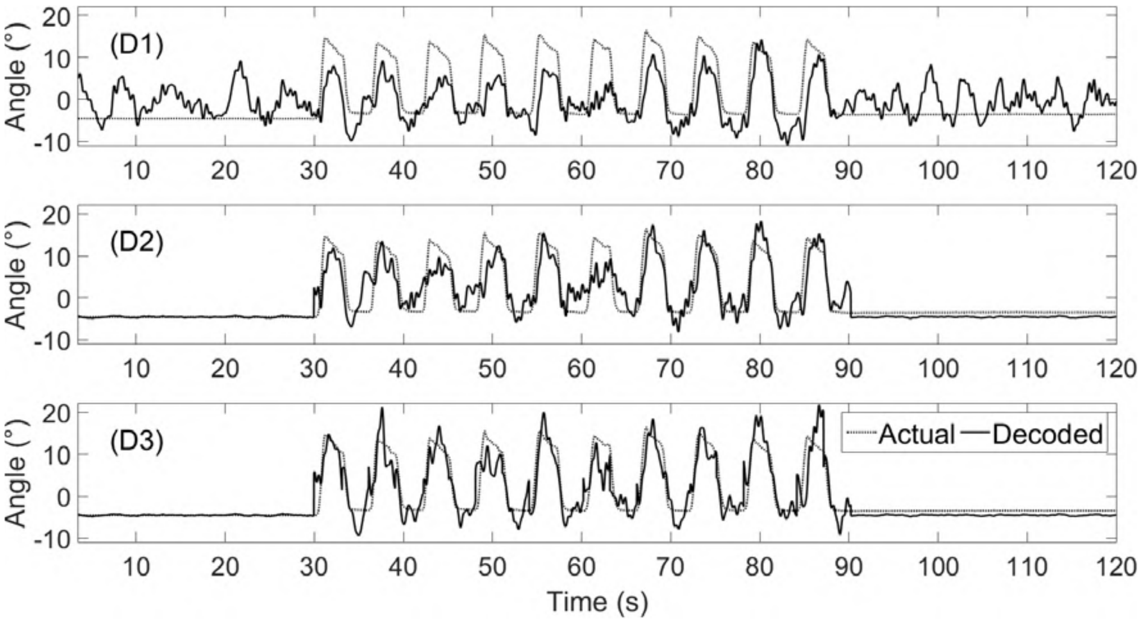

(a) Hip angles decoded using three decoders for Subject 2 during Task 2.

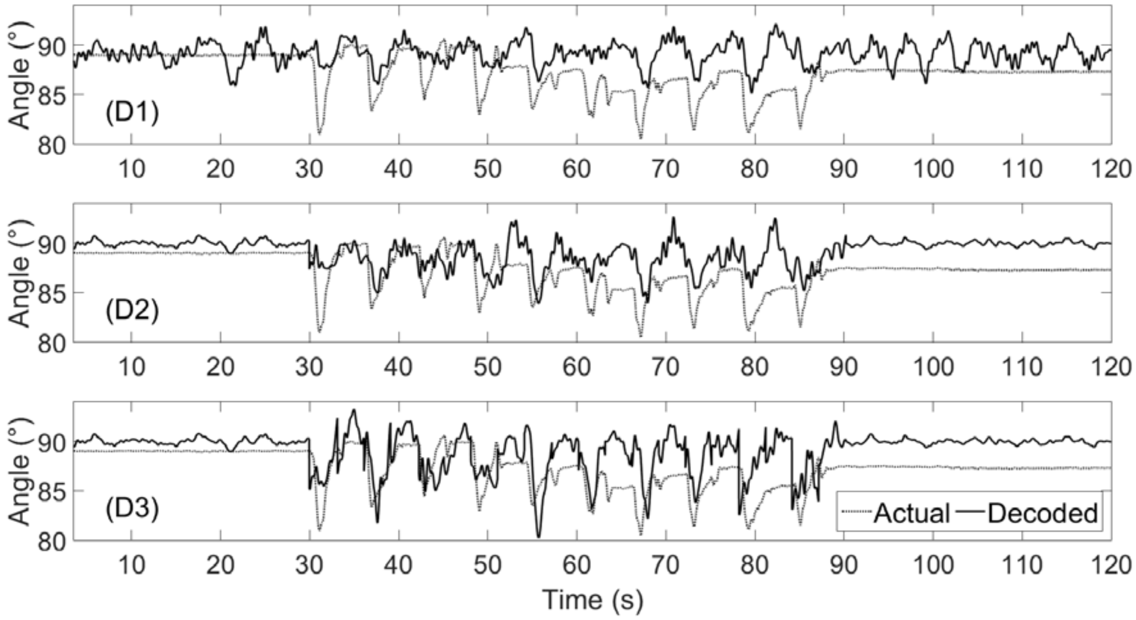

(b) Knee angles decoded using three decoders for Subject 2 during Task 2.

Figure 4.25: Graphs of the actual hip and knee joint angles (dotted line) compared to their decodification (solid line). These decodifications were performed with a time delay of 3.5 s. For each sub-figure from top to bottom: D1, D2, and D3.

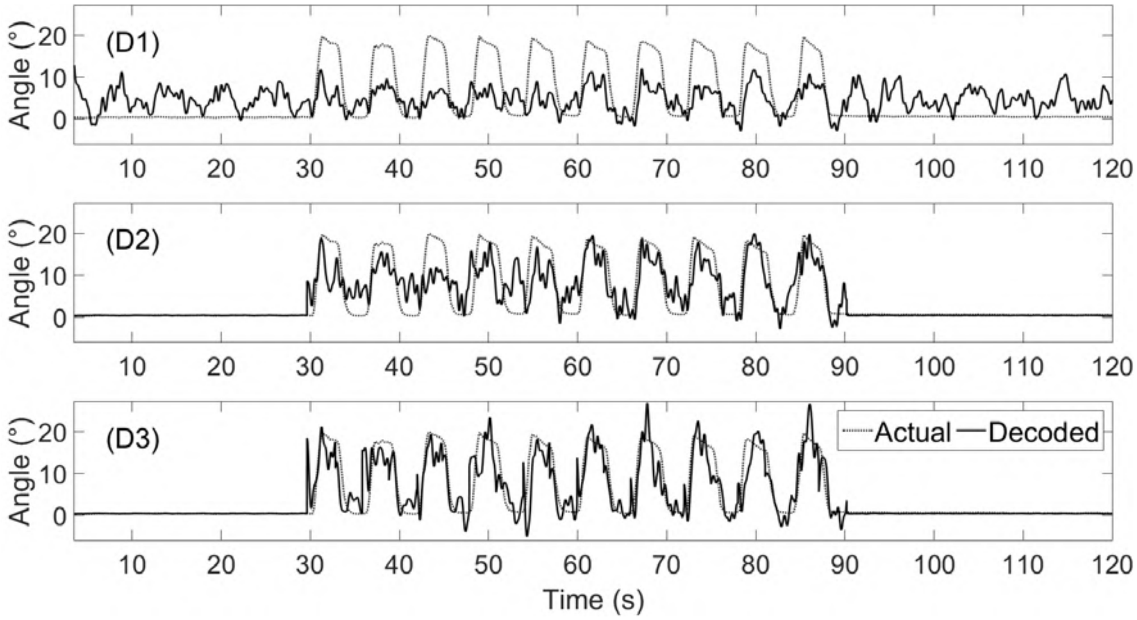

(a) Hip angles decoded using three decoders for Subject 3 during Task 2.

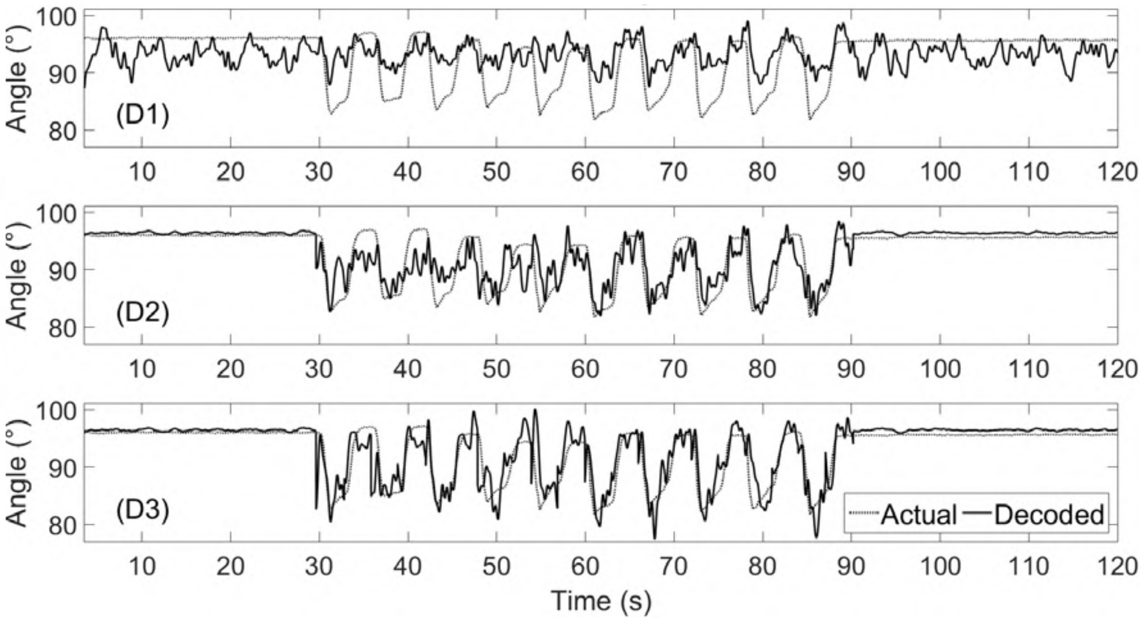

(b) Knee angles decoded using three decoders for Subject 3 during Task 2.

Figure 4.26: Graphs of the actual hip and knee joint angles (dotted line) compared to their decodification (solid line). These decodifications were performed with a time delay of 3.5 s. For each sub-figure from top to bottom: D1, D2, and D3.

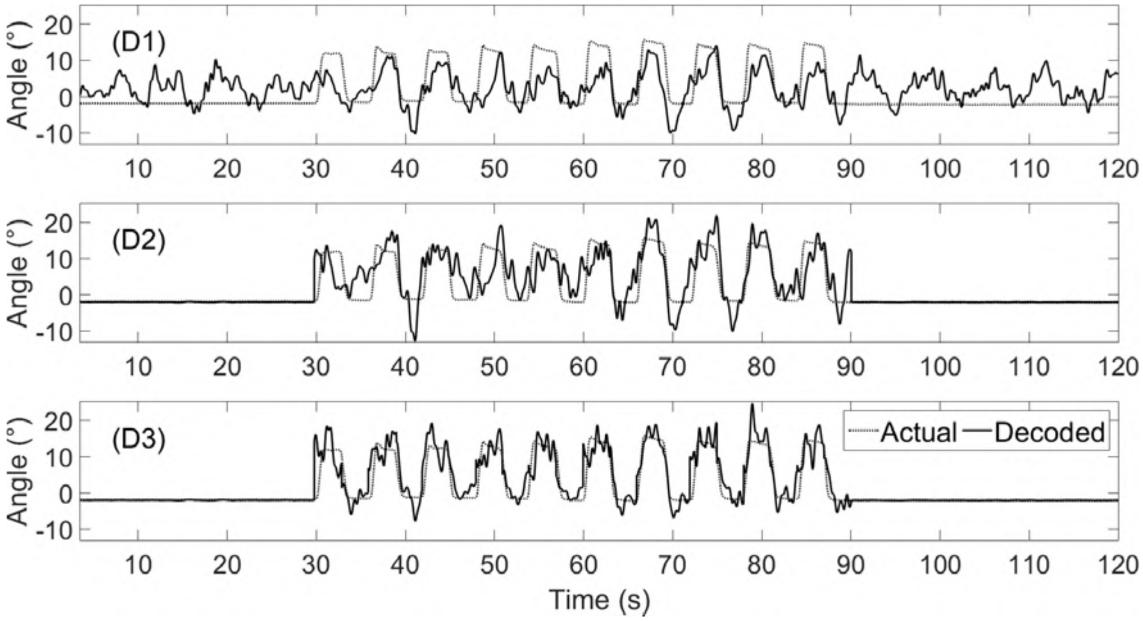

(a) Hip angles decoded using three decoders for Subject 4 during Task 2.

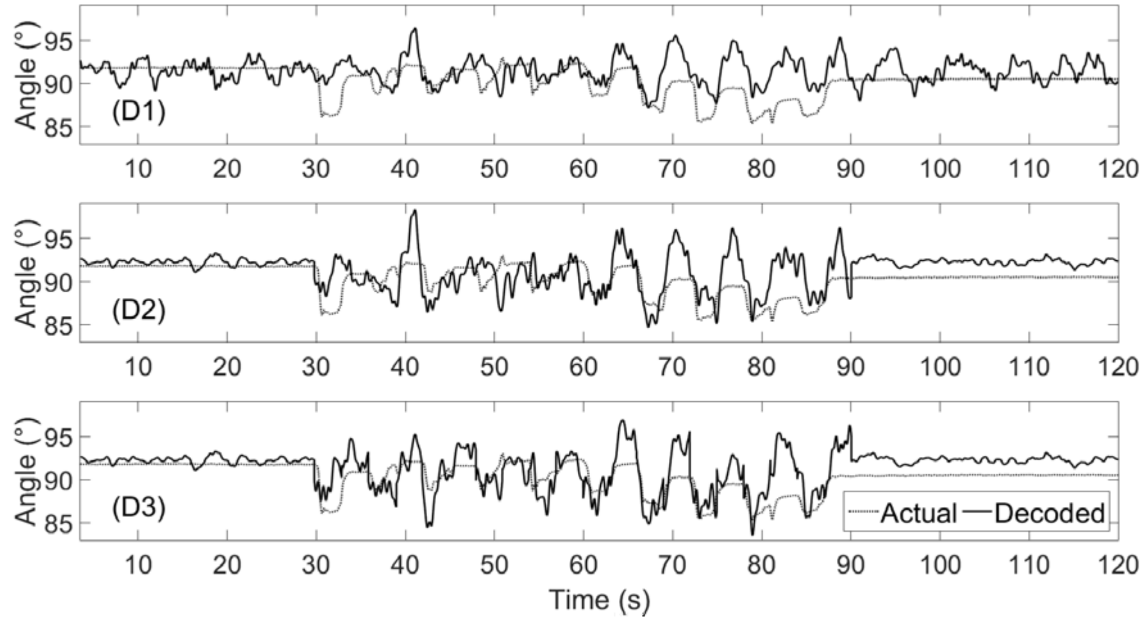

(b) Knee angles decoded using three decoders for Subject 4 during Task 2.

Figure 4.27: Graphs of the actual hip and knee joint angles (dotted line) compared to their decodification (solid line). These decodifications were performed with a time delay of 3.5 s. For each sub-figure from top to bottom: D1, D2, and D3.

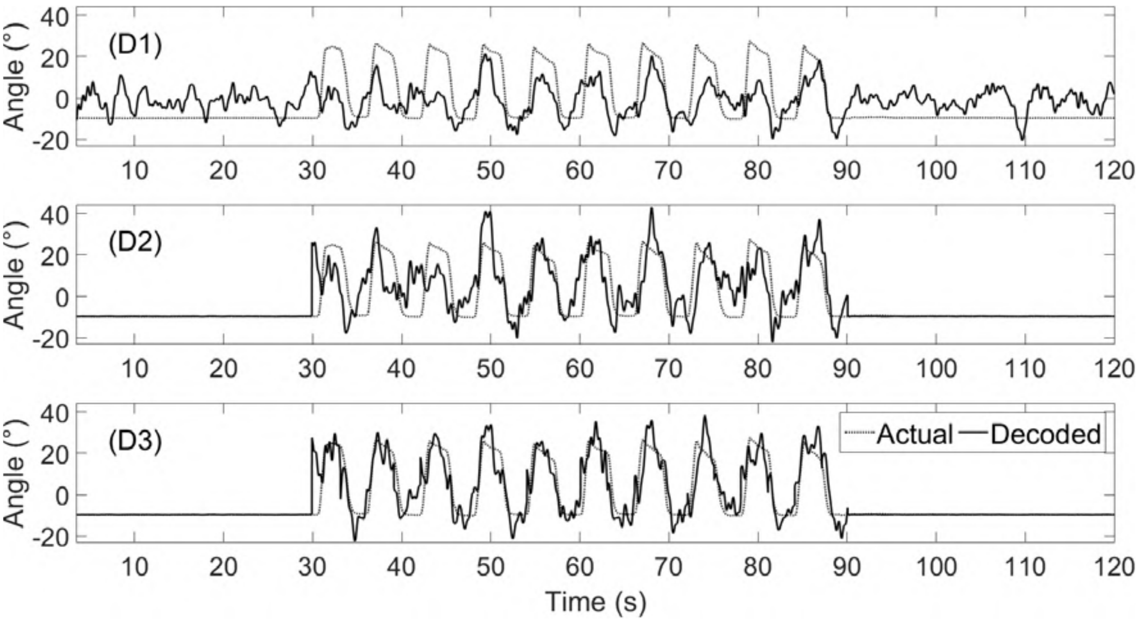

(a) Hip angles decoded using three decoders for Subject 5 during Task 2.

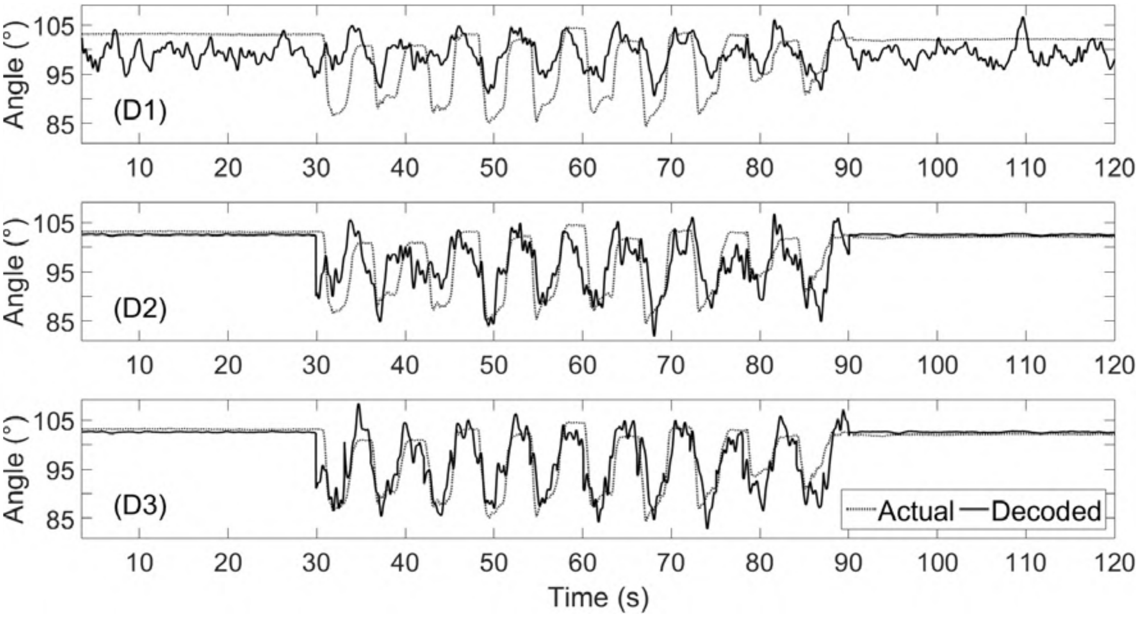

(b) Knee angles decoded using three decoders for Subject 5 during Task 2.

Figure 4.28: Graphs of the actual hip and knee joint angles (dotted line) compared to their decodification (solid line). These decodifications were performed with a time delay of 3.5 s. For each sub-figure from top to bottom: D1, D2, and D3.

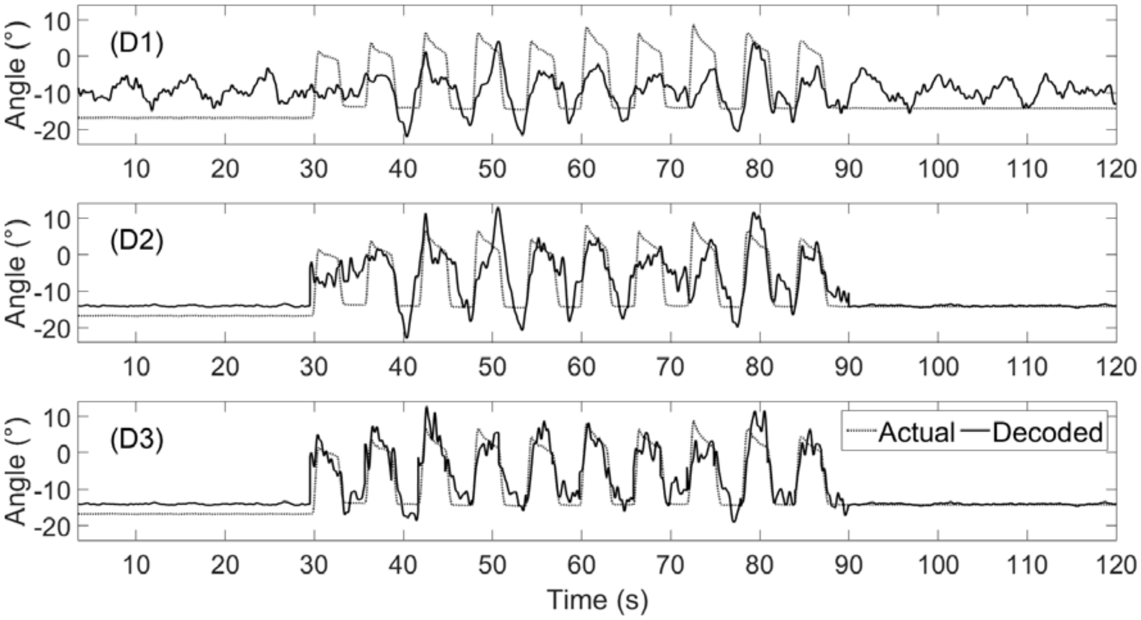

(a) Hip angles decoded using three decoders for Subject 6 during Task 2.

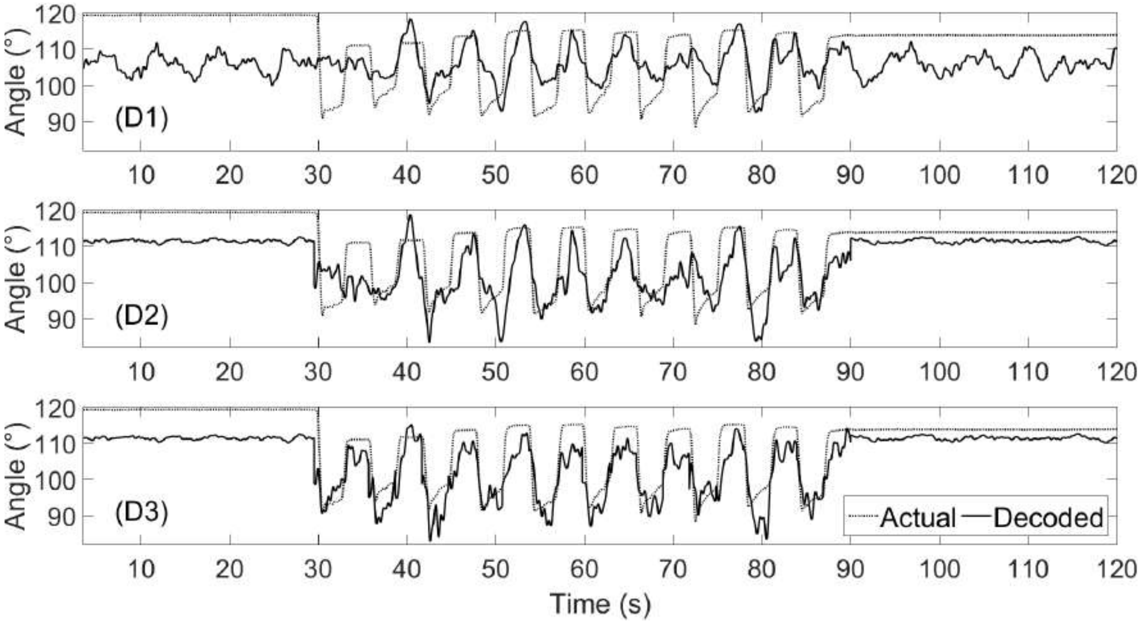

(b) Knee angles decoded using three decoders for Subject 6 during Task 2.

Figure 4.29: Graphs of the actual hip and knee joint angles (dotted line) compared to their decodification (solid line). These decodifications were performed with a time delay of 3.5 s. For each sub-figure from top to bottom: D1, D2, and D3.

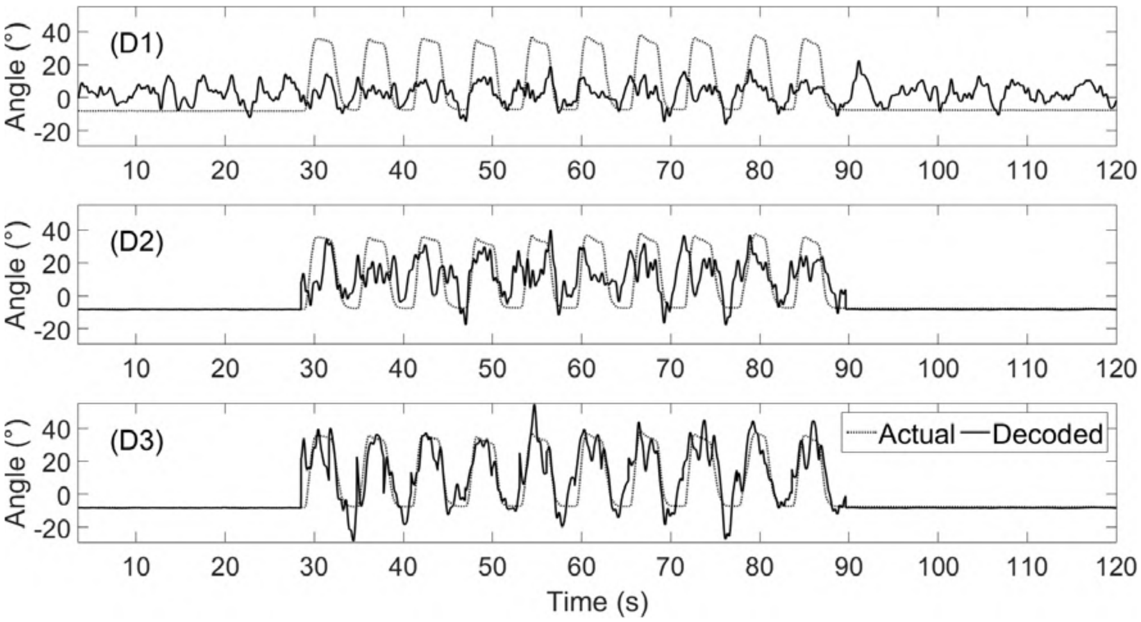

(a) Hip angles decoded using three decoders for Subject 7 during Task 2.

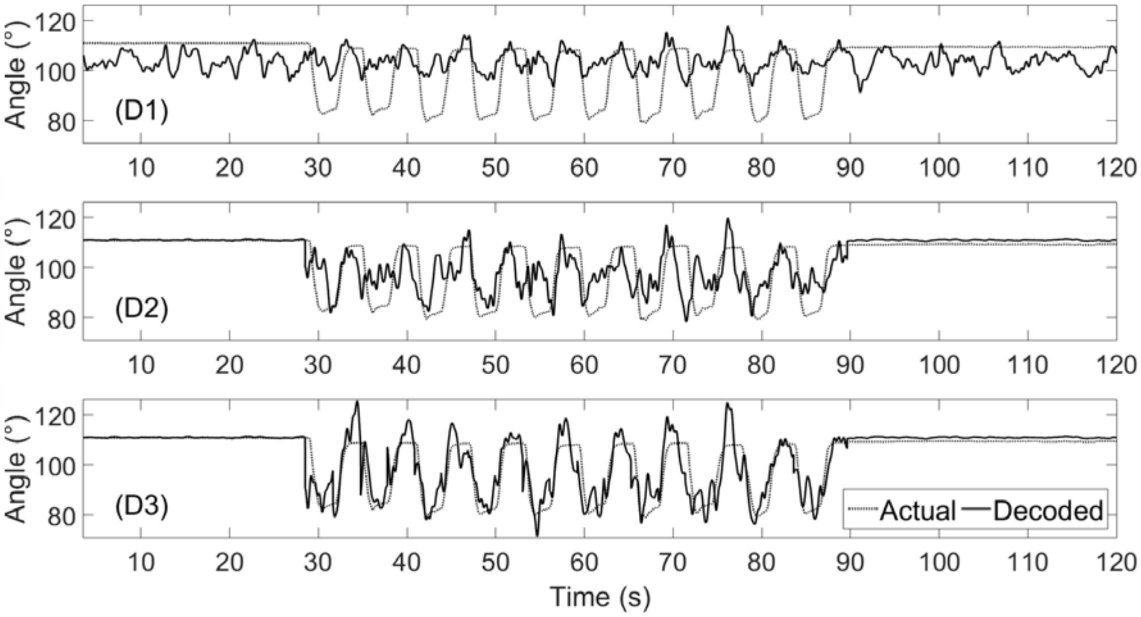

(b) Knee angles decoded using three decoders for Subject 7 during Task 2.

Figure 4.30: Graphs of the actual hip and knee joint angles (dotted line) compared to their decodification (solid line). These decodifications were performed with a time delay of 3.5 s. For each sub-figure from top to bottom: D1, D2, and D3.

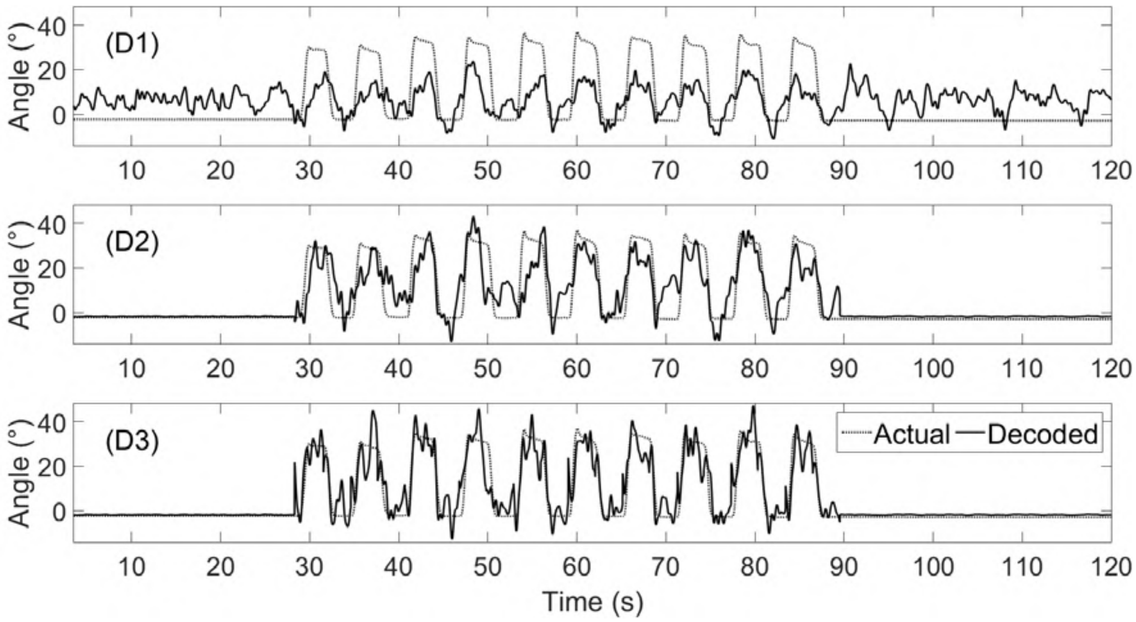

(a) Hip angles decoded using three decoders for Subject 8 during Task 2.

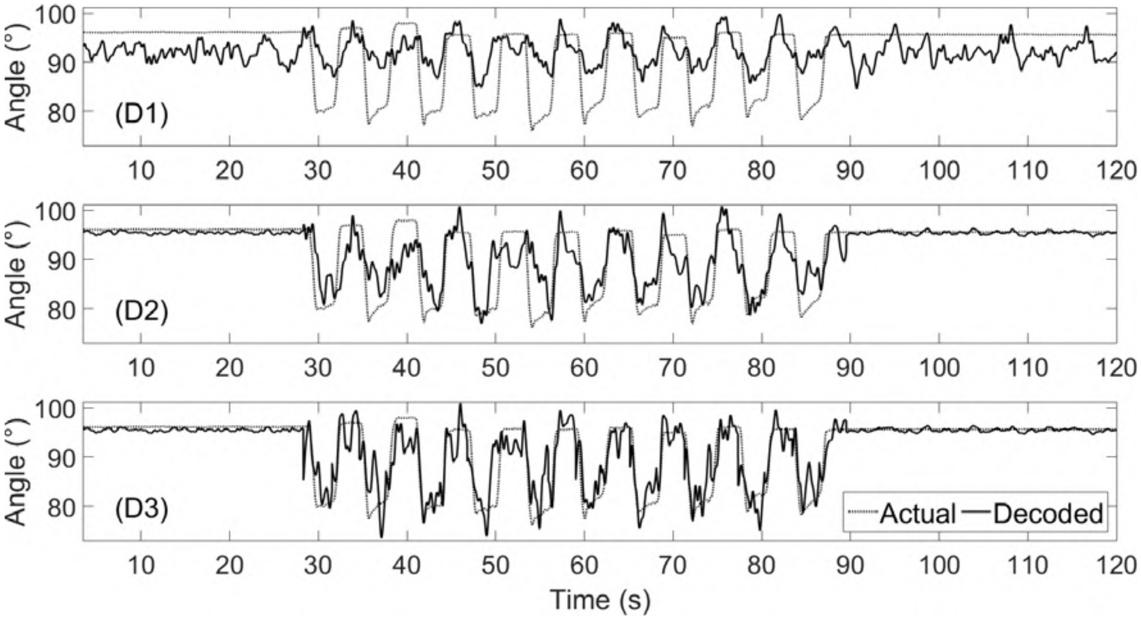

(b) Knee angles decoded using three decoders for Subject 8 during Task 2.

Figure 4.31: Graphs of the actual hip and knee joint angles (dotted line) compared to their decodification (solid line). These decodifications were performed with a time delay of 3.5 s. For each sub-figure from top to bottom: D1, D2, and D3.

4.4 Parametric adjustment for synchronous protocols

It can be appreciated that performing the decodification of kinematic variables using different decoders for specific segments of a task displays a better performance than using a single decoder. However, the parameters of these decodifications were fixed, with only nine electrodes available from the first synchronous protocol data set, and based on the results of the decodifications obtained from the asynchronous protocols, the time delay of 3.5 s. Under a more detail inspection of several studies found in the literature [42, 61, 41, 62], it can be noted that these studies have a tendency to approach the decodification with a certain sets of parameters for decoders specifically focusing on an entire task. These parameters rely on the number of sources and the number of delays of the independent variable, i.e., the brain signal. Most of these studies use 10 lags or gaps, which is the number also applied in this work for Section 4.2 and 4.3. These gaps are selected to cover different lengths of the delays, varying from 80 ms to 3 s. However, there is no basis on why delimit the length of the delay. Furthermore, the studies happen to have different number of sources of the independent variable (from 19 to 60 electrodes) based on the different equipment available on the market. Therefore, to assess the contributions of the different available electrodes and a different number of gaps, a search for a set of parameters to further improve the decodification by segments was carried out. Like in Section 4.2, this search involved different combinations of electrodes and different range of the delays. However, now the search involved a third parameter: the different number of gaps in such delays.

Similar to the process described previously in Section 4.3, the linear optimum filter described in Section 2.2.1 was adapted into the following MLR

$$x[t] = a + \sum_{n=1}^{N} \sum_{k=0}^{G} b_{nk} S_n[t - Lk], \tag{4.10}$$

where $x[t]$ is the decoded joint angle at time t, S_n is the voltage measured at electrode n, N is the number of electrodes, k is the counter of gaps, G is the number of gaps, L is the length between each gap, and a and b are the weights of the linear regression. However, in this occasion there were also two joint angles to decode, therefore for the testing portion, (4.4) similarly expands to:

$$\begin{bmatrix} x_1 & x_2 \end{bmatrix} = \begin{bmatrix} S_1 & S_2 & \cdots & S_{NG} \end{bmatrix} \begin{bmatrix} b_{1,1} & b_{1,2} \\ b_{2,1} & b_{2,2} \\ \vdots & \vdots \\ b_{NG,1} & b_{NG,2} \end{bmatrix} + \begin{bmatrix} a_1 & a_2 \end{bmatrix} \tag{4.11}$$

where x are the decoded variables, S is the voltage measured at electrodes N and G number of gaps, and a and b are the weights of the linear regression. It was stated in Section 3.1.2 that two data sets were considered for the synchornous protocols. The second data set, which consisted of 19 electrodes, was considered for the second parametric adjustment using decodification by segments.

To analyze the different regions of the brain during the synchronous protocols described in Section 3.1, different electrode arrays from the EEG were evaluated, thus varying N. This led to arrange 100 arrays to analyze the contribution of the different cortical regions to the decodification by segments. The arrays 1 to 19 were the 19 available electrodes individually. Arrays 20-100 combined the electrodes from the pre-frontal (Fp), frontal (F), central (C), parietal (P), occipital (O), and temporal (T) areas and their corresponding numerals of the international 10-20 system. These arrays are displayed in a binary manner in Figure 4.32.

Also different time windows prior to the decoded variable were analyzed. This was done by changing both the gap G and the lengths L of these gaps. By changing both parameters, delays ranging from 0.5 s to 5 s were considered, varying the number of gaps from 1 to 10 in increments of 1, and the size of the gaps. For example, if only 2 gaps were desired for a delay of 500 ms, the L value was 250 samples for each gap.

To obtain the regressors values of (4.11) for the two joint angles, the following matrices had to be created:

$$\mathbf{S} = \begin{bmatrix} 1 & S_{1,1} & S_{1,2} & \cdots & S_{1,NG} \\ 1 & S_{2,1} & S_{2,2} & \cdots & S_{2,NG} \\ \vdots & \vdots & \vdots & \ddots & \vdots \\ 1 & S_{\mathrm{TS},1} & S_{\mathrm{TS},2} & \cdots & S_{\mathrm{TS},NG} \end{bmatrix}, \quad \text{and} \quad \mathbf{x} = \begin{bmatrix} x_{1,1} & x_{1,2} \\ x_{2,1} & x_{2,2} \\ \vdots & \vdots \\ x_{\mathrm{TS},1} & x_{\mathrm{TS},2} \end{bmatrix}, \tag{4.12}$$

where the first column of $\mathbf{S}$ is the constant value for the intercept regressor, i.e., value

a for (4.10) and (4.11), and TS are the different values of training samples, which depend on the quantity of samples available after varying the G values. Another value that affected TS, for the synchronous protocols, was a sub-sampling which was mentioned in Section 4.3. After the training models were created, to obtain the regressors, such matrices can be used as in (4.9).

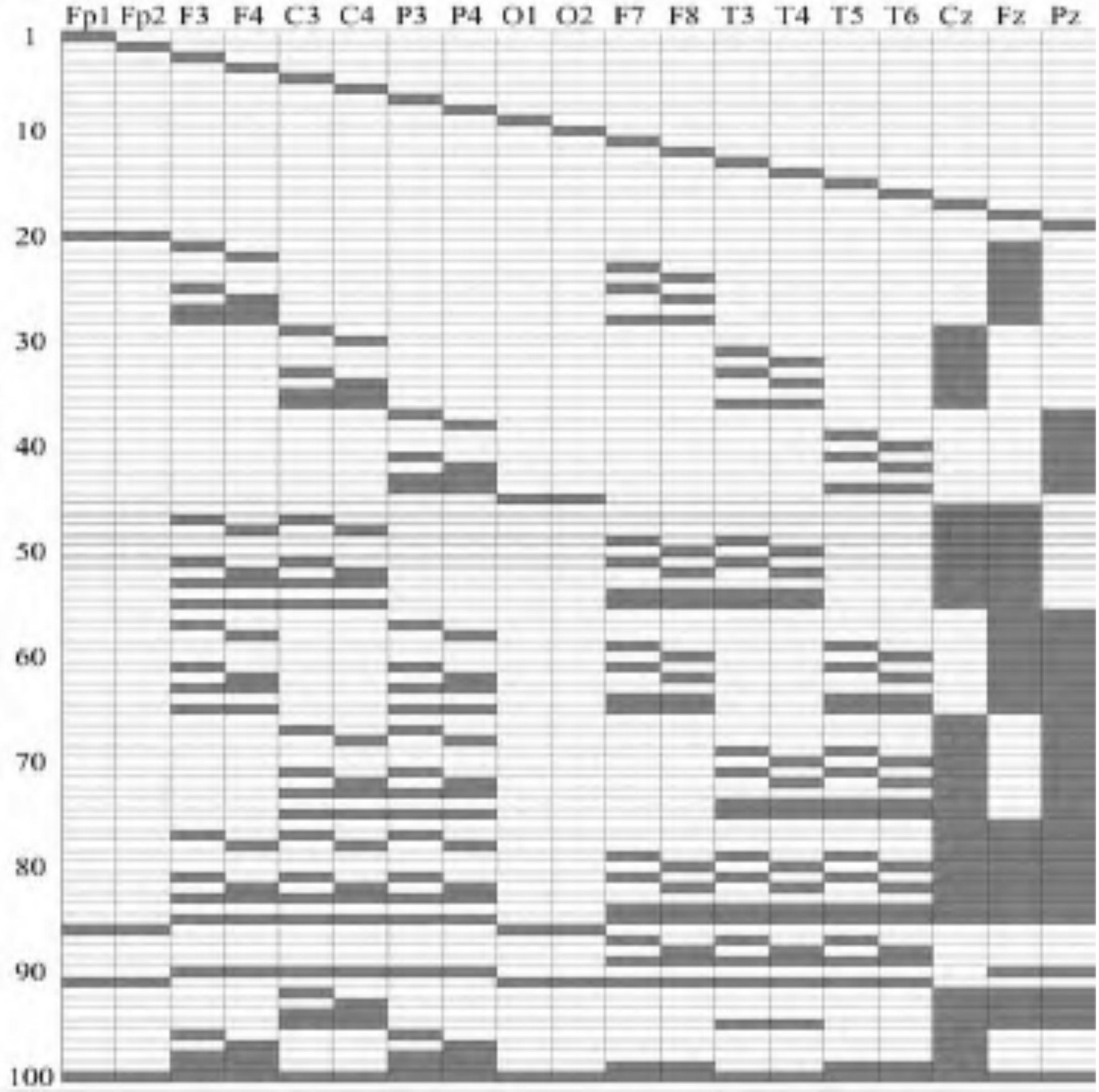
Fp1
Fp2
F3
F4
C3
C4
P3
P4
O1
O2
F7
F8
T3
T4
T5
T6
Cz
Fz
Pz
1
10
20
30
40
50
60
70
80
90
100

Figure 4.32: 100 array combinations represented in a binary table, using 19 electrodes, namely Fp1, Fp2, F3, F4, C3, C4, P3, P4, O1, O2, F7, F8, T3, T4, T5, T6, Cz, Fz, and Pz.

The search between 100 different arrays to find the electrodes that contribute better to the decodification was carried out first. These decodifications used a delay of 3.5 s with 10 gaps, based on a segmented decodifications of Section 4.3. The selected metrics to evaluate the performance of the decodifications were the same metrics used in previous sections, specifically mentioned in Section 2.2.3. To further validate the results obtained, different numbers of trials available in the second data set were used for a M-fold cross-validation, where M ranged from 4 minimum trials to a maximum of 10 for the different subjects. The number of available trials for each subject differ, based on the quality of the acquired kinematic or EEG signals; that is, trials that had the entire kinematic signals or did not had artifacts that when removed, diminished the quality of the EEG signals. The cross-validation values were then averaged for each array and metric. For Task 1, the knee performance was of interest, while Task 2 was focused to the hip. The performances of the arrays by metric were arranged from best to worst, where the electrodes of the best 10% of arrays were taken in consideration. The frequency of appearance of the electrodes in such arrays were normalized for the three metrics. These normalizations can be seen in Figure 4.33. It can be noted that the electrodes that displayed more occurrence were Fz, C3, Cz, C4, P3, Pz, and P4 between subjects. When considering subjects individually, each had their own array with the best performance, but it is important to mention that the electrode Cz is always present regardless of subject. This appears to be logical, based on the fact that Cz is the electrode located nearest to the leg area of the primary motor cortex of the brain.

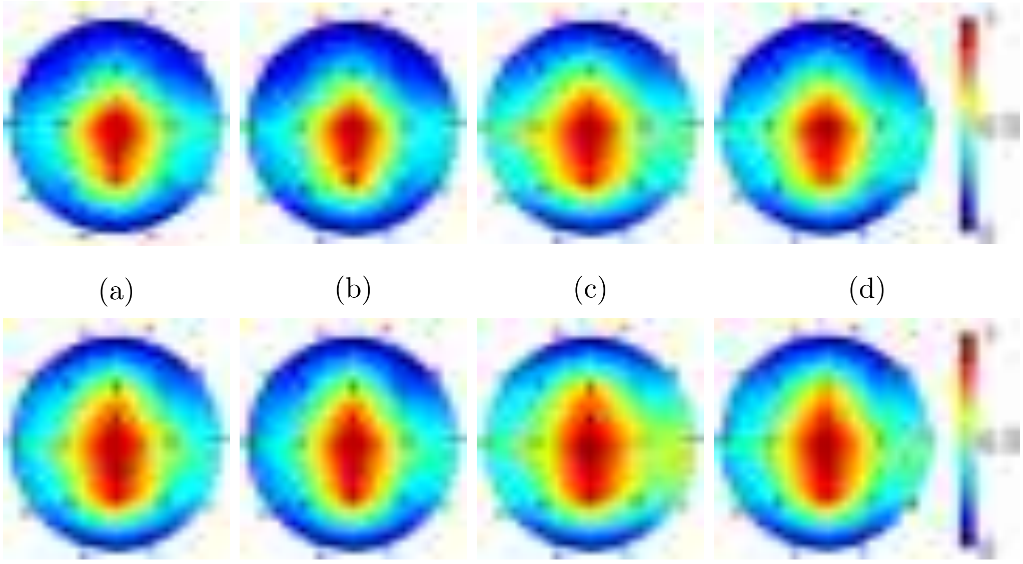

(a) (b) (c) (d)

(e) (f) (g) (h)

Figure 4.33: Normalized occurrence of each electrode of the best 10% of arrays considering the correlation coefficient (a & e), normalized root mean square error (b & f), and signal-to-noise ratio (c & g). The normalized occurrence of the electrodes combining the three metrics is depict in d & h. The first row of the image corresponds to Task 1 and the second row to Task 2.

The search for delays that gave a better performance consisted on varying the number of gaps, and their lengths, used for the linear regression. 100 combinations of delays and lengths of gaps were used. The delays covered from 0.5 s to 5 s in increments of 0.5 s. As previously mentioned, a maximum of 10 gaps in increments of 1 were used for each delay. The electrodes used for these decodings were the set of electrodes that had more occurrence from the 100 arrays search, that is, electrodes Fz, C3, Cz, C4, P3, Pz, and P4 (as seen in Figures 4.33d and 4.33h). The performances of delays and gaps by metric were also arranged similarly to the consideration of arrays. Figure 4.34 displays normalized bar graphs of occurrence of the best 10% of combinations of delays and gaps.

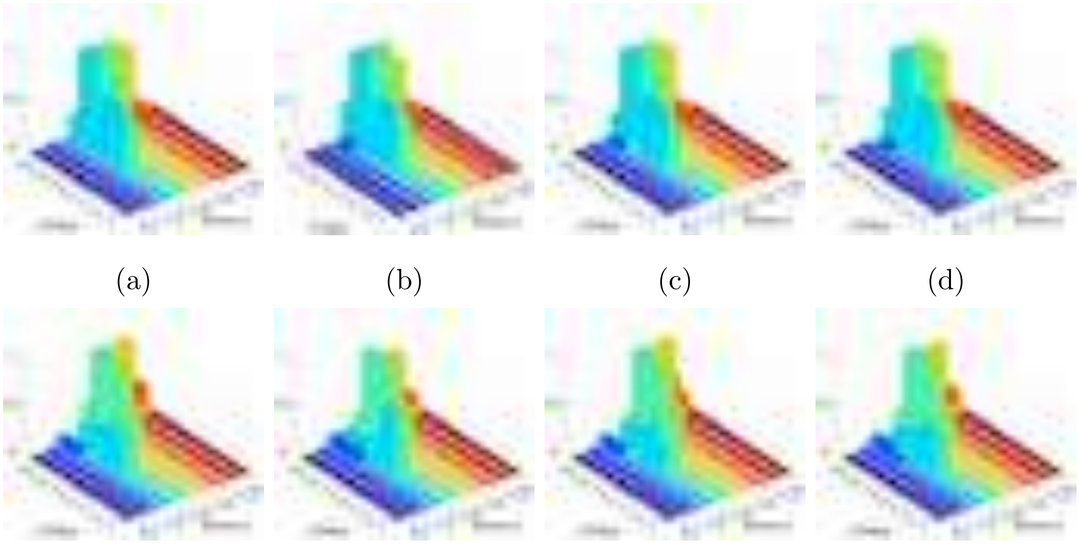

(a) (b) (c) (d)

(e) (f) (g) (h)

Figure 4.34: Normalized occurrence between subjects of each combination of gaps and delay of the best 10% considering the correlation coefficient (a & e), normalized root mean square error (b & f), and signal-to-noise ratio (c & g). The normalized occurrence of the delay and gaps combinations mixing the three metrics is depicted in d & h. The first row of the image corresponds to Task 1 and the second row to Task 2.

Based on these results displayed in Figure 4.34d, it can be seen that there was a tie for Task 1, with delays of 2 s, 2.5 s, and 3 s with 9 gaps, and 2.5 s with 8 gaps. Figure 4.34h displays the most frequent combinations between subjects for Task 2, where there is also a tie between a delay of 2.5 s with 8 and 9 gaps.

Furthermore, Table 4.5 displays the comparison between segmented decodifications of Section 4.3 and the currently adjusted decodifications. The results on Table 4.5 for the parametric adjustment were obtained using the exact same trials for training and testing as the previous section. It can be seen that CC and SNR values increase with the new configuration, while the NRMSE values decrease, thus showing improvement for the decodification.

Subject	**Task 1**					
	CC		**NRMSE**		**SNR**	
	Old	**New**	**Old**	**New**	**Old**	**New**
1	0.8965	0.9011	0.2494	0.2450	4.6705	4.8817
2	0.5955	0.6032	0.2033	0.2012	0.9766	1.0220
3	0.8542	0.8738	0.1614	0.1510	3.2055	3.7007
4	0.6008	0.6236	0.2678	0.2623	0.8965	0.9587
5	0.8345	0.8553	0.1654	0.1528	2.6459	3.1068
6	0.9097	0.9138	0.1843	0.1829	4.7519	4.9166
7	0.8812	0.8983	0.1779	0.1664	3.9568	4.6008
8	0.8841	0.9077	0.2147	0.2046	3.8589	4.5835
μ	0.8071	0.8221	0.2030	0.1958	3.1203	3.4714
σ	0.1226	0.1219	0.0364	0.0384	1.4179	1.5447
Subject	**Task 2**					
	CC		**NRMSE**		**SNR**	
	Old	**New**	**Old**	**New**	**Old**	**New**
1	0.8985	0.9045	0.1767	0.1729	4.6282	5.0488
2	0.9250	0.9405	0.1240	0.1121	6.4868	8.2643
3	0.8612	0.8824	0.1712	0.1577	3.3132	3.8328
4	0.9043	0.9148	0.1536	0.1462	4.8926	5.4236
5	0.8928	0.9031	0.1574	0.1494	4.6068	5.3189
6	0.9239	0.9290	0.1302	0.1269	6.0656	6.5168
7	0.8862	0.9008	0.1761	0.1652	4.0975	4.7262
8	0.9072	0.9236	0.1511	0.1386	5.1846	6.2241
μ	0.8999	0.9123	0.1550	0.1461	4.9094	5.6694
σ	0.0194	0.0173	0.0186	0.0187	0.9538	1.2545

Table 4.5: Comparing the configurations of previously used parameters (Old) and the parametric adjustment (New) for the segmented decodifications. Task 1 values at the top and Task 2 values at the bottom of the table. CC and SNR values increase with the new configuration, while the NRMSE values decrease.

4.5 OPTIMIZATION BY GENETIC ALGORITHM

As mentioned in Section 2.2.2, the implementation of the GA in the BMI literature are mostly used to find an optimal solution for the different methods or models used for estimation or reconstruction of one signal from another type of signal. In this work, the linear optimum filter by segmentation remained as the chosen decodification method of the EEG signal into the lower limb kinematics. As previously stated, multiple linear regression models are often used as approximating functions, i.e., the relationship between y and $x_1, x_2, ..., x_k$, is unknown, but over certain ranges of the independent variables, the linear regression model is an adequate approximation even for models complex in structure. However, the linear regression model in some occasions is inappropriate because the true regression function is nonlinear. Since the EEG was consider nonlinear and quasistationary in Section 2.1, and the results shown in Section 4.1 seem to strengthen this consideration, a suitable transformation was applied. Nonlinear models that can be transformed into a straight line are called intrinsically linear [88]. Examples of nonlinear models that are intrinsically linear are considered in functions:

$$y = \beta_0 e^{\beta_1 x}, \quad \text{and} \qquad y = \beta_0 + \beta_1 \left(\frac{1}{x}\right). \tag{4.13}$$

These functions are intrinsically linear since they can be transformed to a straight line by a logarithmic transformation and the reciprocal $z = 1/x$ respectively, linearizing the models into

$$\ln y = \ln \beta_0 + \beta_1 x, \quad \text{and} \qquad y = \beta_0 + \beta_1 z. \tag{4.14}$$

There are other types of transformations for the nonlinearities of a model, for example

$$y = \beta_0 + \beta_1 x + \beta_2 x^2 + \beta_3 x^3, \quad \text{and} \qquad y = \beta_0 + \beta_1 x_1 + \beta_2 x_2 + \beta_{12} x_1 x_2. \tag{4.15}$$

Where the cubic polynomial can be changed by $x_1 = x$, $x_2 = x^2$, $x_3 = x^3$, and the interaction effects changed by $x_3 = x_1 x_2$, and $\beta_3 = \beta_{12}$, to form the same linear regression model

$$y = \beta_0 + \beta_1 x_1 + \beta_2 x_2 + \beta_3 x_3. \tag{4.16}$$

Applying similar transformations, the GA searched for an optimal function that transformed the EEG signal used in the multiple linear regression model. Based on the results obtained in Section 4.4, it can be seen that out of the 19 electrodes, only 7 were required. For this reason, the first data set of the synchronous protocols was used in the GA search. The other 2 electrodes not included in the results of Section 4.4 were included in the GA search to assess if a transformation function applied to these electrodes contributed to the decodification.

As stated in Section 2.2.2, there is a need for a genetic representation of the candidate solutions. For this work, the chromosomes were vectors of dimension $[1 \times 9]$, where each of the 9 arrays take the values $0-5$, which represent the different transformations functions from Table 4.6. Those functions were selected for being considered simple nonlinear functions, thus not giving more load to the computational process of the GA. Each of the arrays affects individually the 9 electrodes used on the first data set of the synchronous protocols.

Value	Transformation Function $f(S_n)$
0	S_n
1	e^{S_n}
2	S_n^2
3	S_n^3
4	$\sin(S_n)$
5	$\cos(S_n)$

Table 4.6: Values of the genetic representation and their respective transformation function. S_n represents the n-th electrode of the EEG signals.

The fitness function selected for this work was the NRMSE, described in Section 2.2.3. This was the chosen function because the NRMSE value displays the difference between the actual values and the predicted or decoded ones in a percentage manner. The tournament selection was applied in this work, where each individual competed with another random individual, and the one with the best fitness value was selected for the crossover. Selection was done with replacement, i.e., the same chromosome could have been selected more than once to become a parent. In this work, the crossover between the randomly chosen pair of parents was always executed, since the crossover probability *pc* was fixed at 100%. Regarding the mutation probability *pm*, the chosen value was 40%. It was considered rather high, since the literature tends to use really small values (e.g., 0.001) [80]. These high values of *pc* and *pm* were chosen in order to have a high probability of an entire new population of individuals. Such populations consisted of 25 individuals, which participated in several runs with different number of generations. The parameters used on the GA are summarized in Table 4.7. Also it is worth mentioning that the segmented decodification was performed using the nine electrodes of the controlled mobility protocols with a time delay of 2.5 s based on the results of Section 4.4. However, to have a similar or comparable basis to the literature, 10 gaps were still used for these decodifications.

Parameter	**Information**
Individuals	25
Fitness Function	NRMSE
Selection	Tournament
Crossover probability	100%
Mutation probability	40%
Generations	Various (from 10 to 100)
Runs	Various (from 5 to 8)

Table 4.7: Parameters chosen for the genetic algorithm.

Table 4.8 shows the fitness values comparison between the segmented decodification without any transformation and the best segmented decodification obtained after running the GA for the eight subjects for Task 1, focusing on the knee joint angle. Alongside the fitness values are the respective different chromosomes for each individual test subject, additionally the other metrics are displayed. Similarly, Table 4.9 shows the values for Task 2, focusing on the hip angle.

Table 4.10 shows the test subject with the best fitness value among the eight subjects for Task 1 for the knee joint angle. This table shows the best fitting chromosome with their respective transformation function applied to the set of electrodes.

In a similar way, Table 4.11 shows the values for Task 2 for the hip joint angle.

Figures 4.36 to 4.42 display the comparison between the actual knee joint angles, the segmented decodification without transformations, and the best segmented decodification obtained with the GA, for the eight subjects. Figures 4.44 to 4.50 display in a similar way the comparison for the hip joint angles.

CC		SNR		NRMSE		Chromosome
No $f(S)$	$f(S)$	No $f(S)$	$f(S)$	No $f(S)$	$f(S)$	
0.9318	0.9374	6.9661	7.6388	0.1382	0.1324	0 0 3 5 4 0 4 0 4
0.9444	0.9545	8.3188	10.0639	0.1223	0.1115	0 4 3 3 3 0 1 2 2
0.8461	0.8624	3.3091	3.5944	0.2031	0.1891	2 2 5 1 2 0 1 1 1
0.9145	0.9163	4.8973	5.3078	0.1592	0.1566	5 4 3 3 2 4 4 0 3
0.9060	0.9060	4.7015	4.7015	0.1597	0.1597	0 0 0 0 0 0 0 0 0
0.9052	0.9099	5.2767	5.4252	0.1645	0.1600	4 5 4 4 0 0 4 1 3
0.8742	0.8742	4.0348	4.0348	0.2139	0.2139	0 0 0 0 0 0 0 0 0
0.8318	0.8772	2.4405	3.2893	0.2178	0.1903	2 2 4 1 3 0 3 1 0

Table 4.8: Comparison of the segmented decodification with and without transformation function. The last column displays the chromosome of the best performance obtained by the GA using the NRMSE fitness value for the knee joint angle decodification during Task 1. Additionally, the metrics of CC and SNR are also displayed.

CC		SNR		NRMSE		Chromosome
No $f(S)$	$f(S)$	No $f(S)$	$f(S)$	No $f(S)$	$f(S)$	
0.8479	0.9220	3.3389	6.4570	0.2234	0.1702	4 5 5 5 2 0 1 4 2
0.9142	0.9370	5.8515	7.7908	0.1332	0.1115	3 3 5 5 3 0 1 3 1
0.8723	0.8897	3.4835	3.9421	0.1755	0.1627	3 4 5 4 0 4 1 3 4
0.9093	0.9243	5.7645	6.8052	0.1588	0.1402	4 5 1 3 1 1 4 2 0
0.9077	0.9184	5.1985	5.8307	0.1462	0.1375	0 5 4 4 0 0 1 0 4
0.9206	0.9295	5.6284	6.1692	0.1232	0.1170	2 4 4 4 4 0 3 3 4
0.8897	0.9019	4.4156	4.9341	0.1671	0.1573	5 1 4 4 0 0 0 2 0
0.9279	0.9329	6.1902	6.5195	0.1334	0.1286	3 4 5 4 4 0 5 0 0

Table 4.9: Comparison of the segmented decodification with and without transformation function. The last column displays the chromosome of the best performance obtained by the GA using the NRMSE fitness value for the hip joint angle decodification during Task 2. Additionally, the metrics of CC and SNR are also displayed.

Electrode	F3	F4	Fz	C3	C4	Cz	P3	P4	Pz
Chromosome	0	4	3	3	3	0	1	2	2
Transformation function $f(S_n)$	S_1	$\sin(S_2)$	S_3^3	S_4^3	S_5^3	S_6	e^{S_7}	S_8^2	S_9^2

Table 4.10: Chromosome and its respective transformation functions of the subject with the best performance of the fitness value from Table 4.8.

Electrode	F3	F4	Fz	C3	C4	Cz	P3	P4	Pz
Chromosome	3	3	5	5	3	0	1	3	1
Transformation function $f(S_n)$	S_1^3	S_2^3	$\cos(S_3)$	$\cos(S_4)$	S_5^3	S_6	e^{S_7}	S_8^3	e^{S_9}

Table 4.11: Chromosome and its respective transformation functions of the subject with the best performance of the fitness value from Table 4.9.

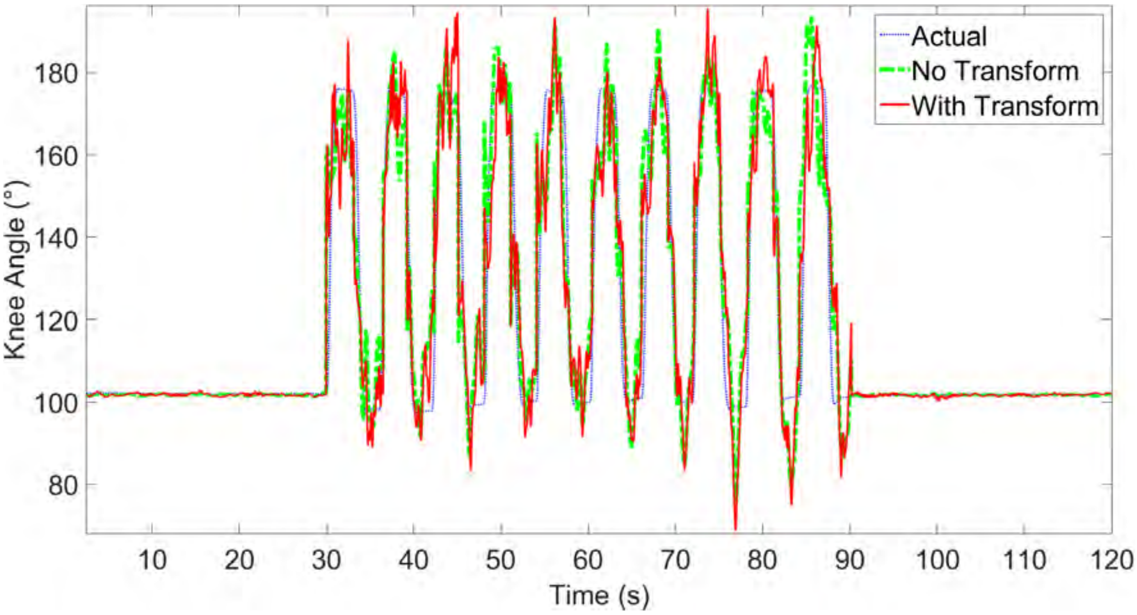

Figure 4.35: Graph of the actual knee joint angle (blue dot line) compared to the segmented decodification without transformation functions (green dash-dot line) and with transformation functions (red solid line) for Subject 1 during Task 1.

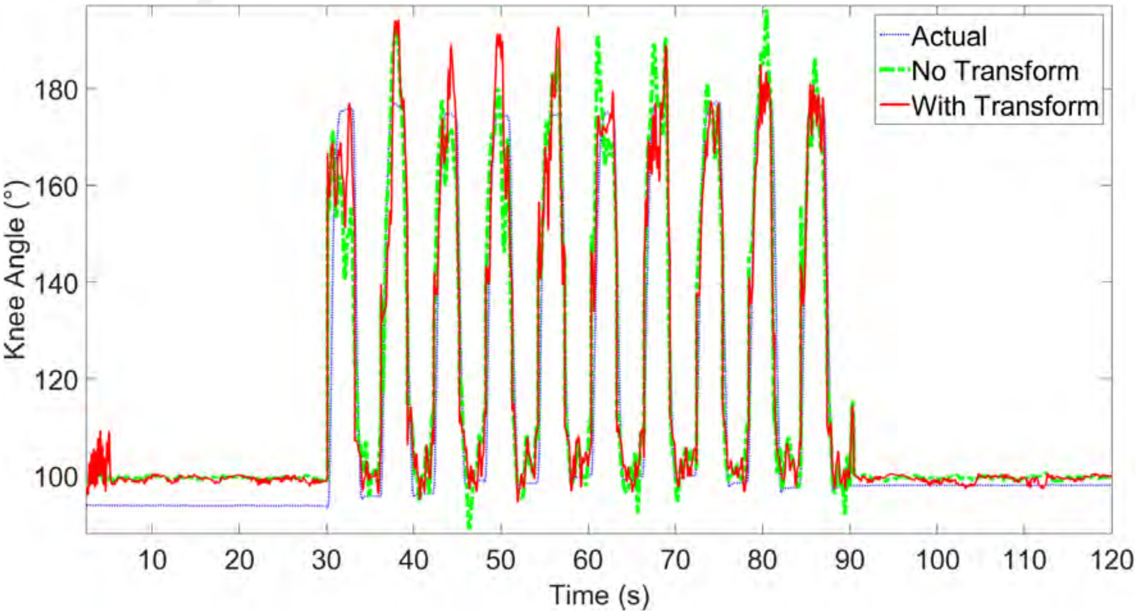

Figure 4.36: Graph of the actual knee joint angle (blue dot line) compared to the segmented decodification without transformation functions (green dash-dot line) and with transformation functions (red solid line) for Subject 2 during Task 1.

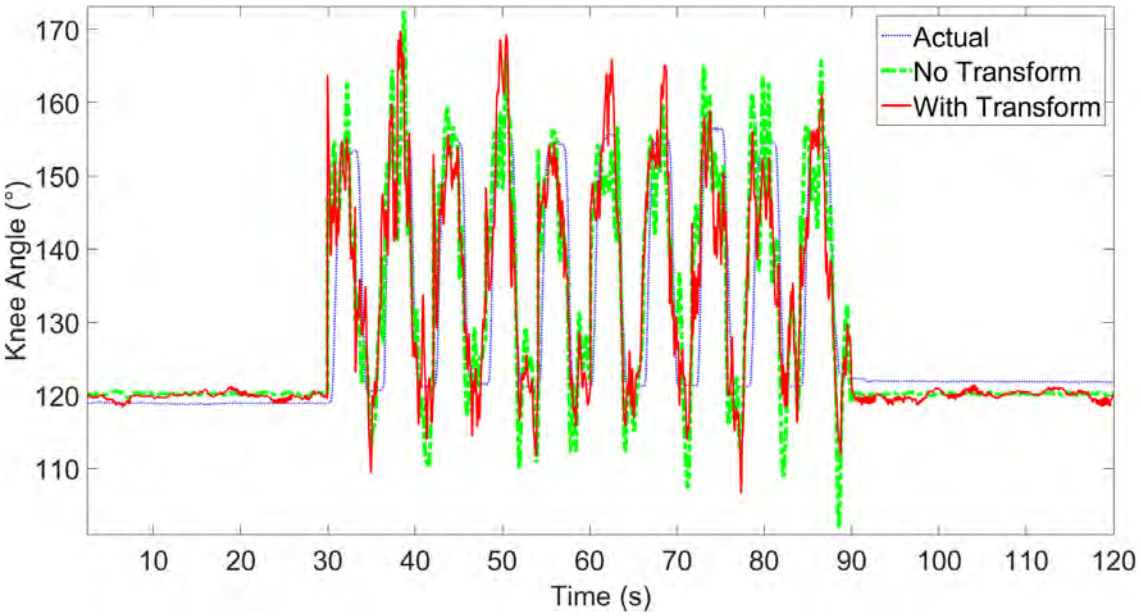

Figure 4.37: Graph of the actual knee joint angle (blue dot line) compared to the segmented decodification without transformation functions (green dash-dot line) and with transformation functions (red solid line) for Subject 3 during Task 1.

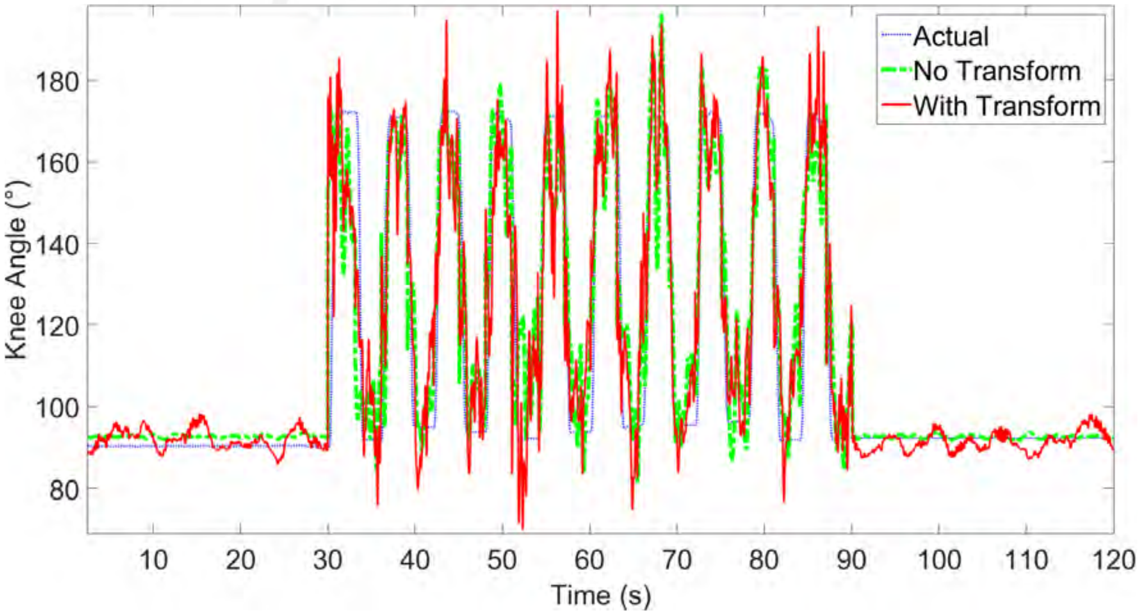

Figure 4.38: Graph of the actual knee joint angle (blue dot line) compared to the segmented decodification without transformation functions (green dash-dot line) and with transformation functions (red solid line) for Subject 4 during Task 1.

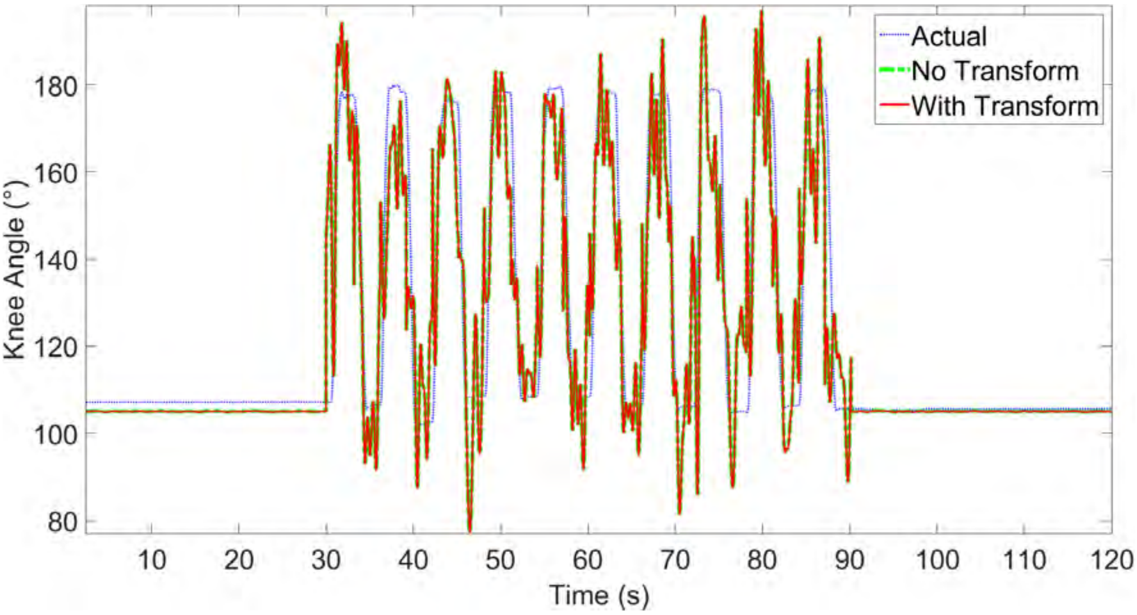

Figure 4.39: Graph of the actual knee joint angle (blue dot line) compared to the segmented decodification without transformation functions (green dash-dot line) and with transformation functions (red solid line) for Subject 5 during Task 1.

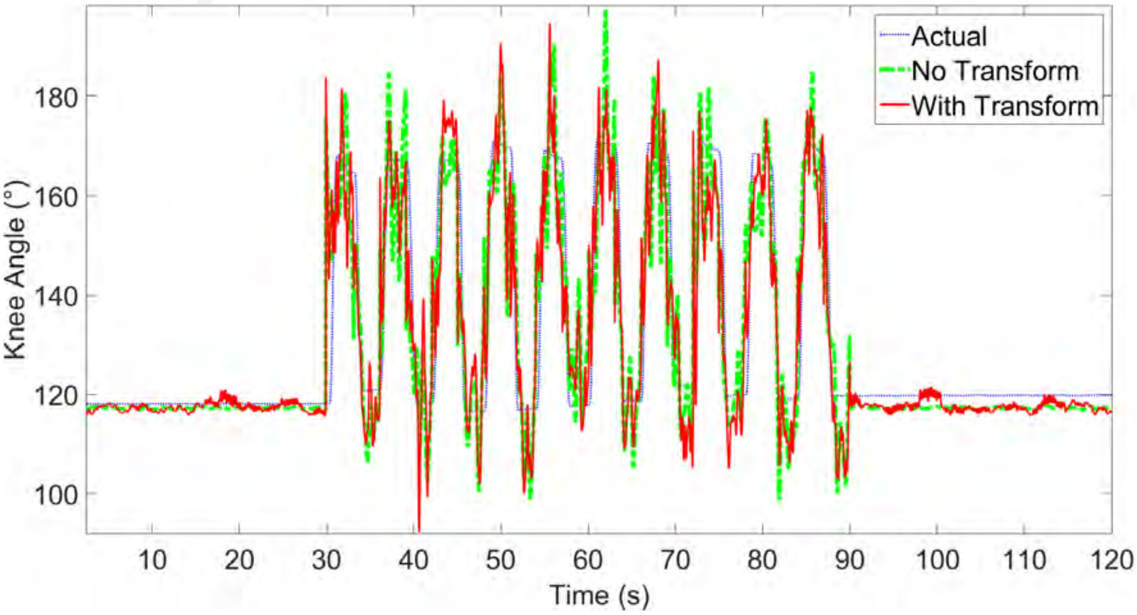

Figure 4.40: Graph of the actual knee joint angle (blue dot line) compared to the segmented decodification without transformation functions (green dash-dot line) and with transformation functions (red solid line) for Subject 6 during Task 1.

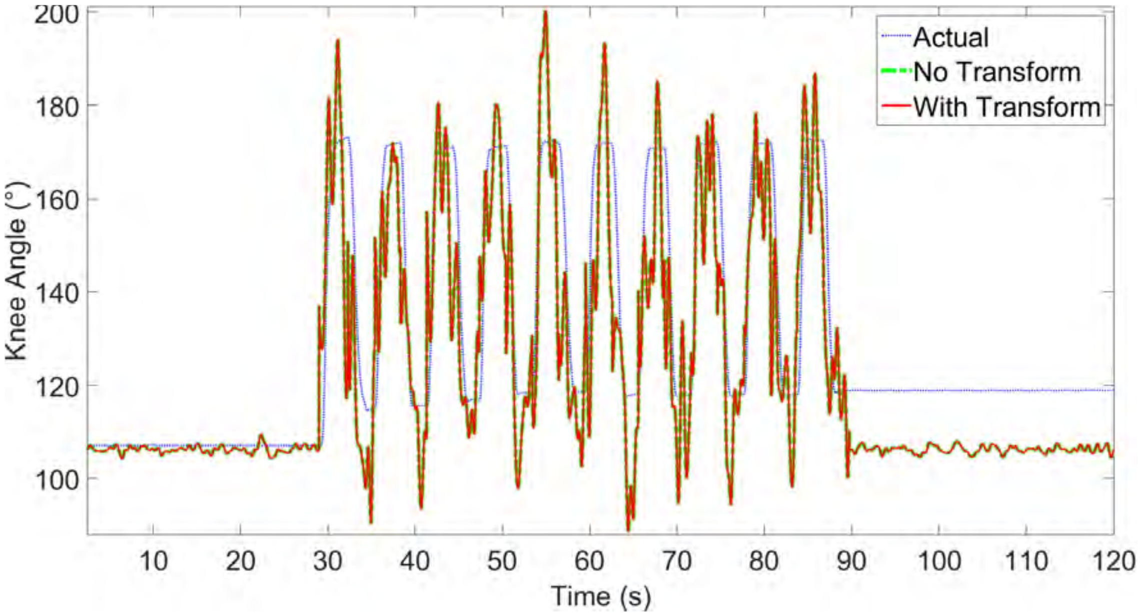

Figure 4.41: Graph of the actual knee joint angle (blue dot line) compared to the segmented decodification without transformation functions (green dash-dot line) and with transformation functions (red solid line) for Subject 7 during Task 1.

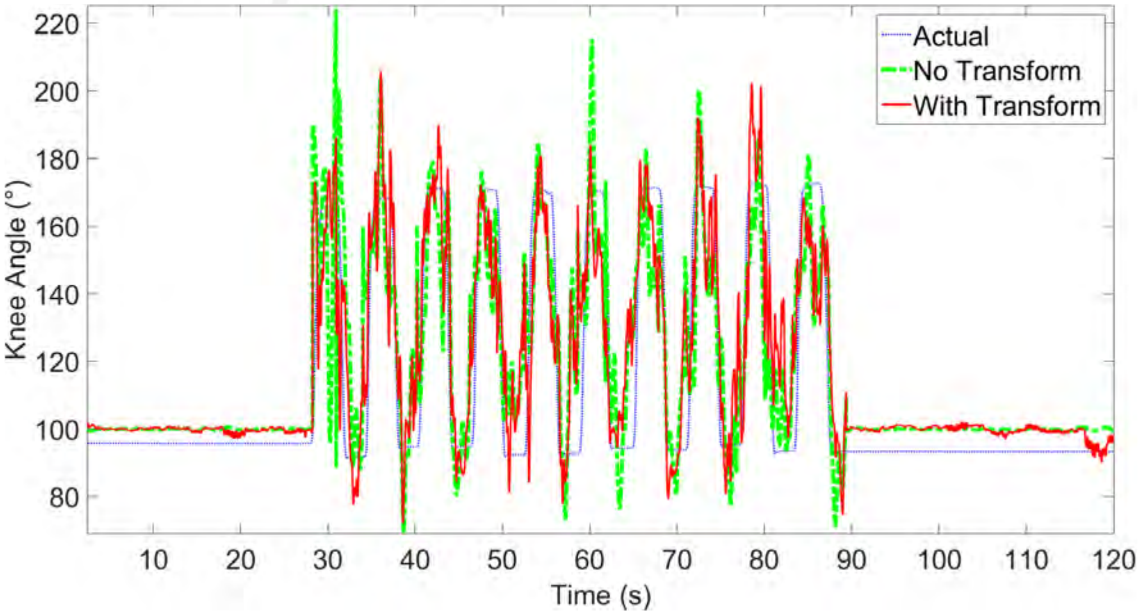

Figure 4.42: Graph of the actual knee joint angle (blue dot line) compared to the segmented decodification without transformation functions (green dash-dot line) and with transformation functions (red solid line) for Subject 8 during Task 1.

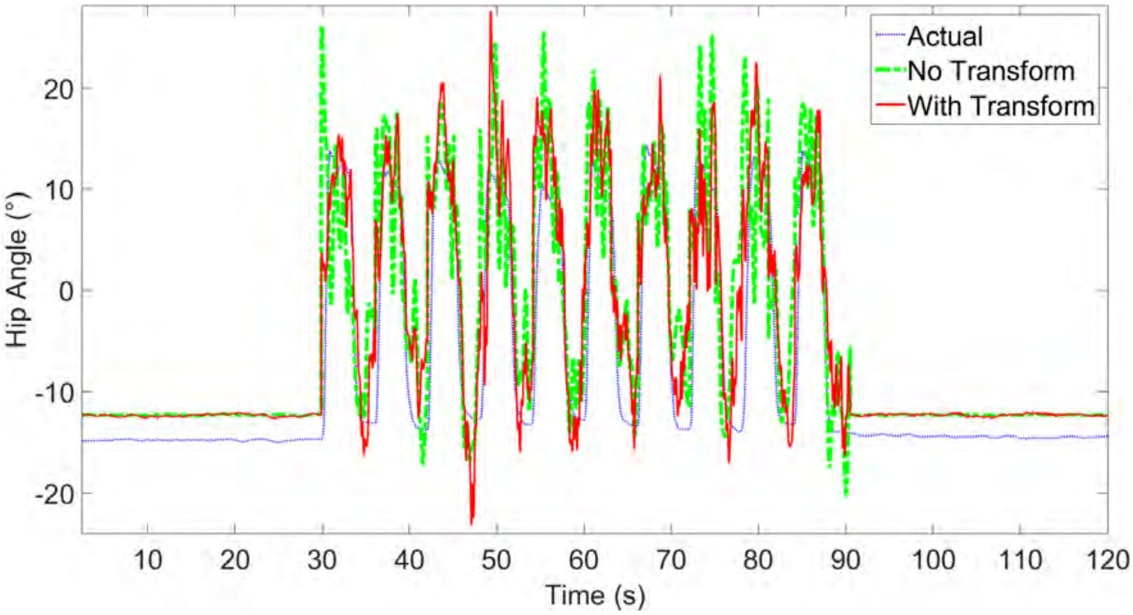

Figure 4.43: Graph of the actual hip joint angle (blue dot line) compared to the segmented decodification without transformation functions (green dash-dot line) and with transformation functions (red solid line) for Subject 1 during Task 2.

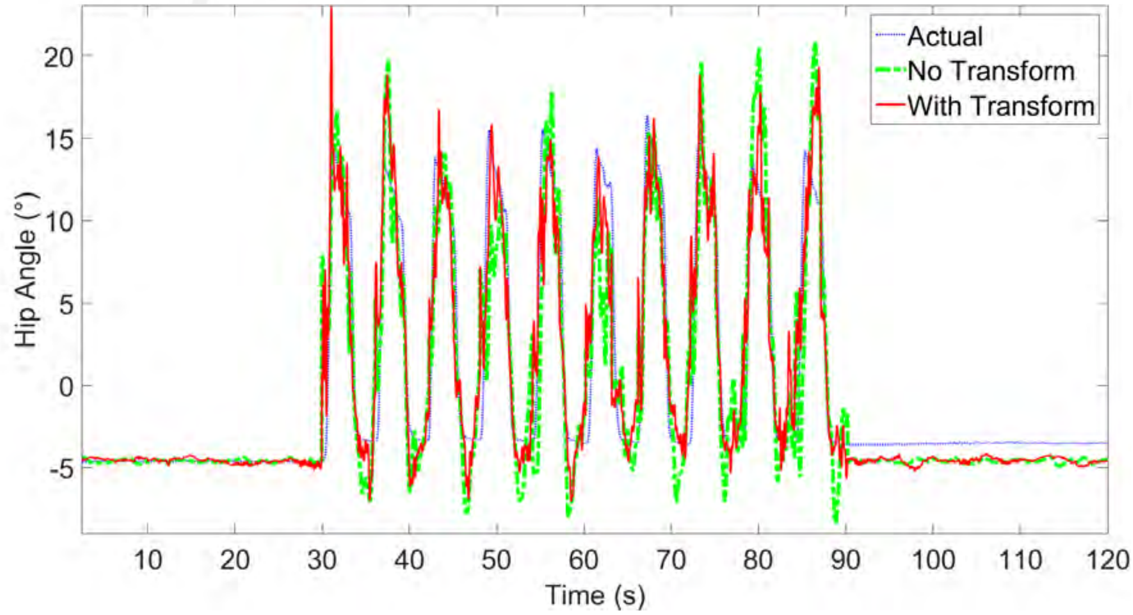

Figure 4.44: Graph of the actual hip joint angle (blue dot line) compared to the segmented decodification without transformation functions (green dash-dot line) and with transformation functions (red solid line) for Subject 2 during Task 2.

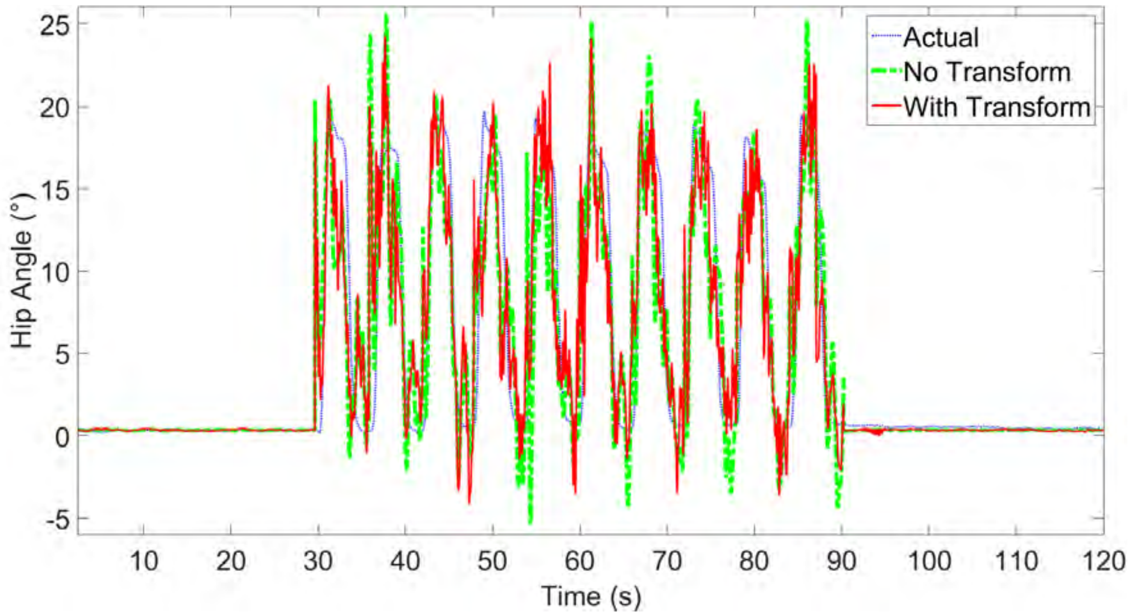

Figure 4.45: Graph of the actual hip joint angle (blue dot line) compared to the segmented decodification without transformation functions (green dash-dot line) and with transformation functions (red solid line) for Subject 3 during Task 2.

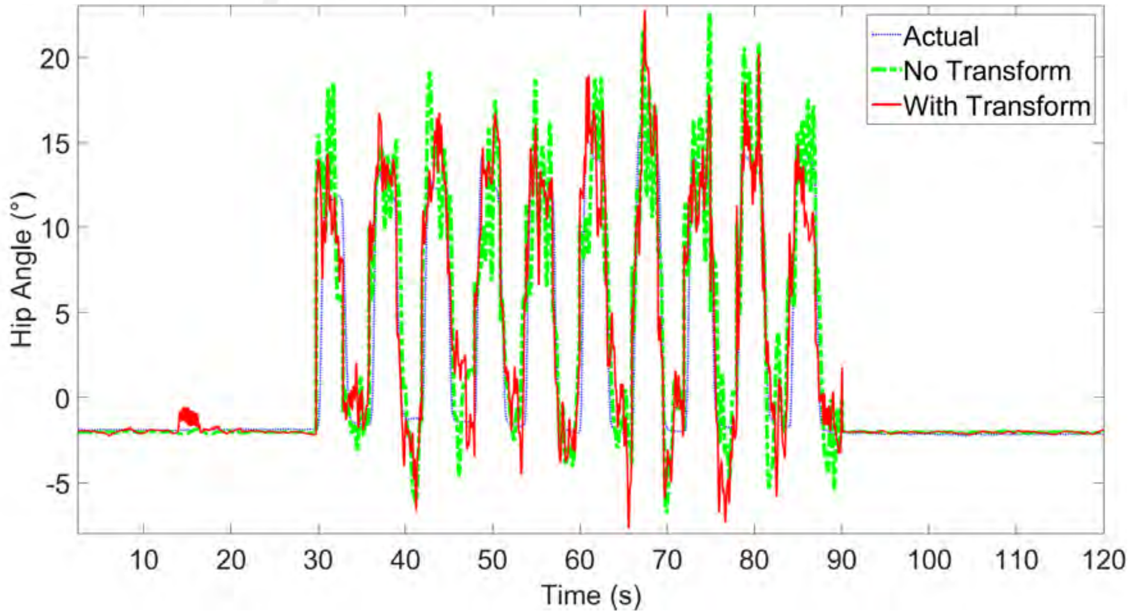

Figure 4.46: Graph of the actual hip joint angle (blue dot line) compared to the segmented decodification without transformation functions (green dash-dot line) and with transformation functions (red solid line) for Subject 4 during Task 2.

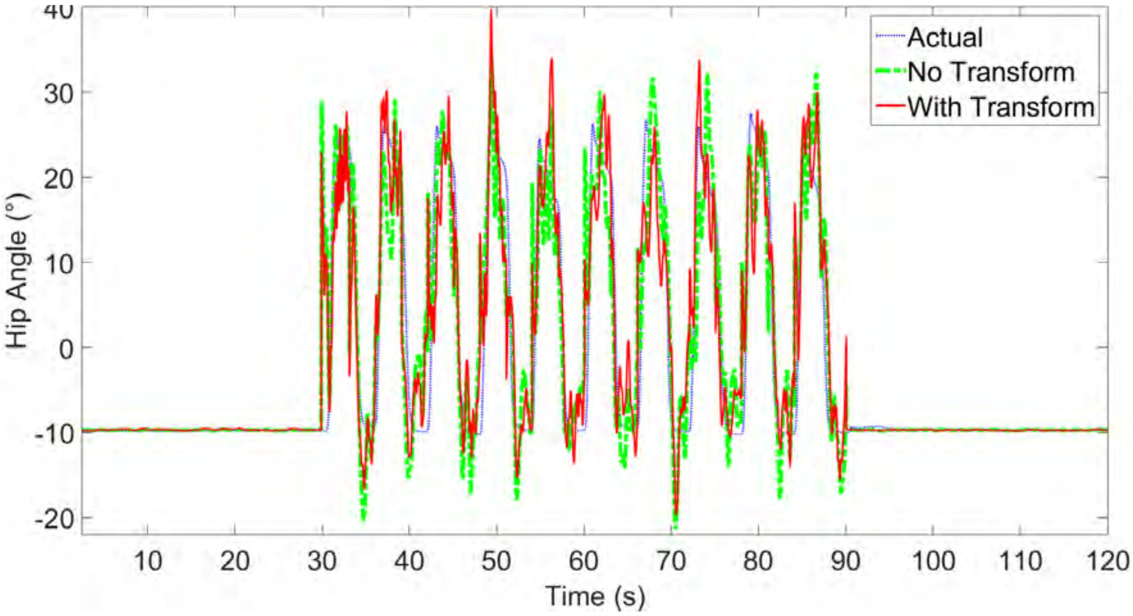

Figure 4.47: Graph of the actual hip joint angle (blue dot line) compared to the segmented decodification without transformation functions (green dash-dot line) and with transformation functions (red solid line) for Subject 5 during Task 2.

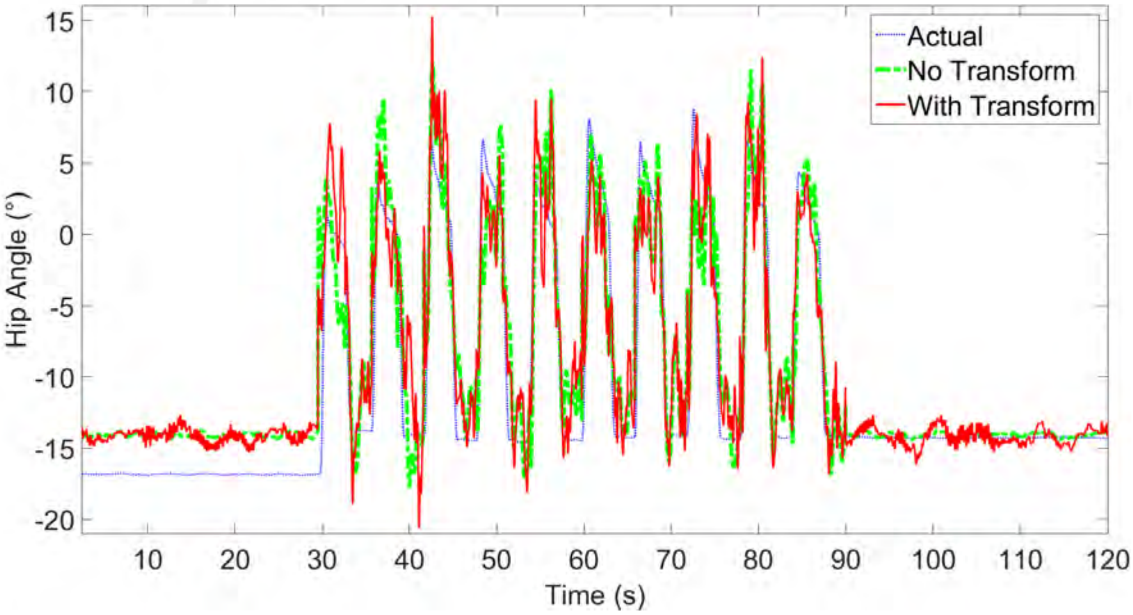

Figure 4.48: Graph of the actual hip joint angle (blue dot line) compared to the segmented decodification without transformation functions (green dash-dot line) and with transformation functions (red solid line) for Subject 6 during Task 2.

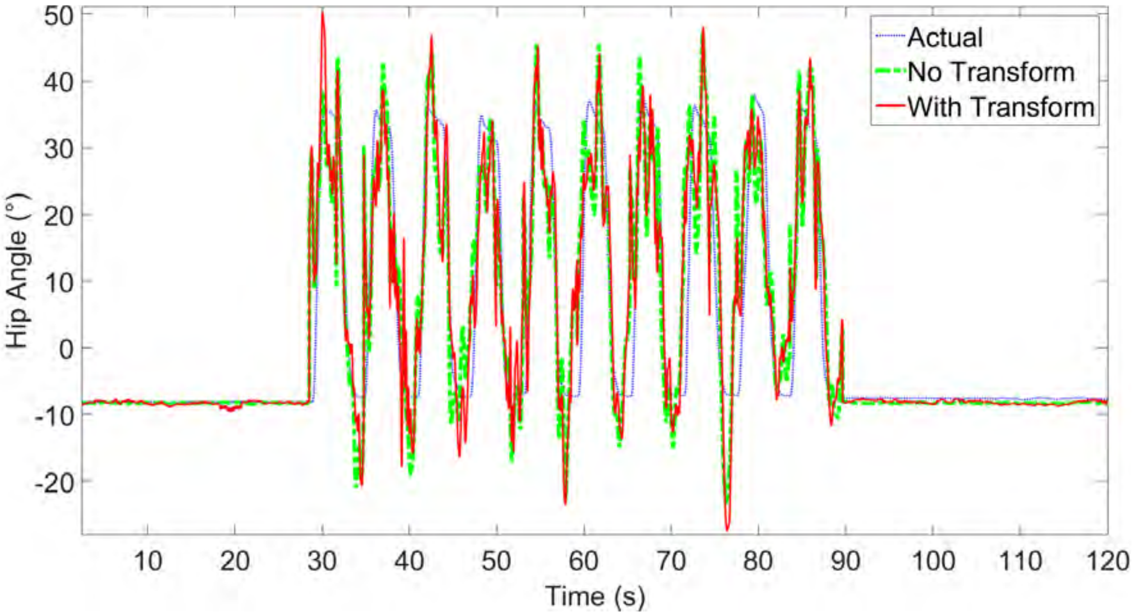

Figure 4.49: Graph of the actual hip joint angle (blue dot line) compared to the segmented decodification without transformation functions (green dash-dot line) and with transformation functions (red solid line) for Subject 7 during Task 2.

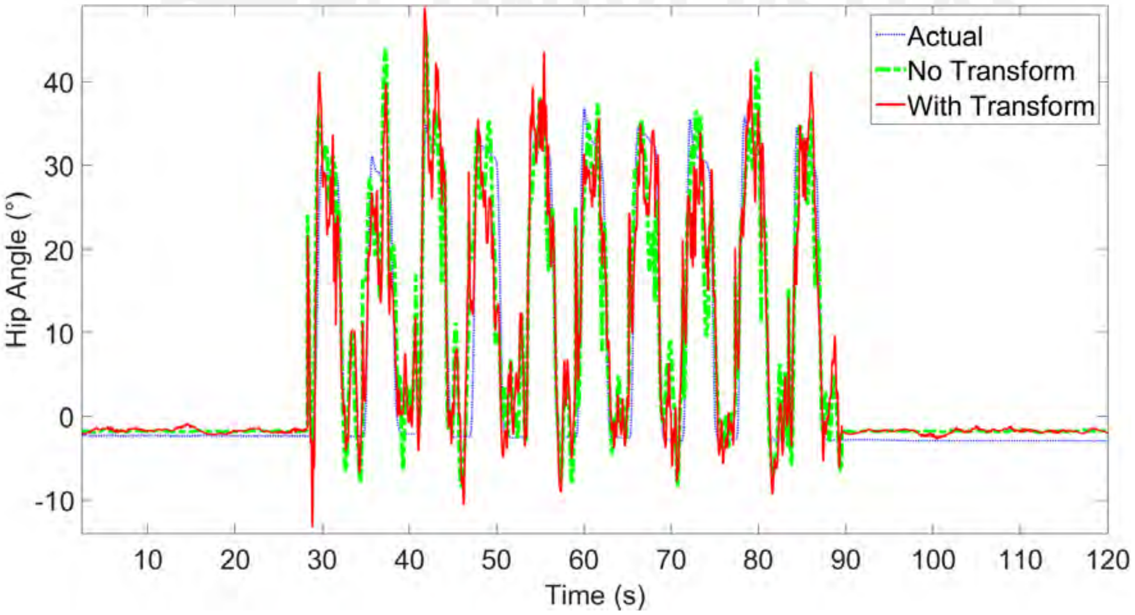

Figure 4.50: Graph of the actual hip joint angle (blue dot line) compared to the segmented decodification without transformation functions (green dash-dot line) and with transformation functions (red solid line) for Subject 8 during Task 2.

Chapter 5

Conclusions and Future Work

5.1 Conclusions

The main contribution of this thesis consists on proving that it is possible to make a continuous trajectory reconstruction, also called decodification, from slow cortical potentials, i.e., low frequencies of the EEG signals. The approach of decodification had previously been applied in the literature to periodic trajectories like the gait cycle. This work focused on comparing different sets of movements, attempting to decode the kinematics of the lower limbs during synchronous mobility protocols.

The following contributions have been led by the development of this thesis:

- One focus of this thesis was to analyze the nonlinear characteristics of the EEG signals during synchronous lower limb mobility protocols. Whereas in the literature, it has only been reported the characterization of these signals between different mental states. In order to obtain insight of the underlying dynamics of the EEG signals three indices were chosen.

  According to the obtained Hurst exponent (H) values, the EEG signal shows a nonrandom persistent behavior, when considering the selected time windows. Usually for diagnostic purposes, prolonged amounts of time are considered. However, this thesis has proven that since actions or movements are rather fast (short time windows), H reveals that the brain signals behave in a persistent manner during these short intervals. With the results here presented, it can be appreciated that on average when the subjects raise the limb, the randomness decreases since H moves away from the 0.5 value. Furthermore, on the resting periods, the average leans toward 0.5 values, showing that when the subjects rest the signal leans to randomness, as depicted in Figures 4.2 and 4.3. These results are consistent with the statistics reported in Figures 4.4 and 4.5, where it is clear that mean and standard deviation during the resting periods have small variations, in comparison to the large changes of raising and lower periods indicating a nonstationary behavior. This is more evident in the electrodes Cz and Pz, which sense the neural activity of the motor cortex above the lower limb region.

Since the correlation dimension (CD) values are related to the minimum number of variables or equations needed to model the behavior of a system in phase space, Figures 4.6 and 4.7 show that the complexity of the dynamics of the underlying system is contained in a space of dimension between 4 and 6, suggesting the order of the dynamical model constructed from observable time series. However, these results reflect that such dimensions might relate to model the behavior of a single electrode. The entire underlying system of the brain most likely possess a bigger dimensionality, considering all the cortical regions affect each other when using EEG recordings.

Based on the CD, the largest Lyapunov exponent (LLE) values were computed from reconstructed time series of dimension 5 for each electrode. The strictly positive LLE values obtained from the EEG time series suggest that the dynamics of the underlying system is nonlinear, this is based on the premise that a linear system with a positive LLE implies unstable trajectories, and with the evidence that the EEG signals are bounded and stable as it is shown in Figure 4.4 and Figure 4.5. Also as mentioned before, the cortical regions might have nonlinear interactions among each other, which could show how the underlying system of the brain tends for a higher dimensionality.

- Mainly this thesis gives additional evidence regarding the decodification of the kinematics of lower limbs in humans from low frequency EEG components. The results for the decodifications were performed with three approaches.

  An exhaustive search for the best suited parameters of decodification was held for asynchronous protocols. This was done by using the electrodes that cover the cortical regions FC, C, and CP, with different time delays ranging from

0.5 s to 5 s in the past. According to their performance, the best array to obtain good results of decodification, with the evaluation metrics of CC and NRMSE, is array number 12; which is the set of electrodes that cover specifically the cortical region C. From an electrophysiological point of view, this seems rather logical since this region is related to the motor control of the brain. Also it is considered that the most exterior C electrodes might have had the relevant information of the lower limb movement derivated from the main electrode Cz, since this electrode is allocated over the lower limb region of the motor cortex. However, the array number 42 which includes all the electrodes of regions FC, C, and CP, gives the best SNR. This is also appears to be quite a logical outcome, since the amount of desired decodification stays higher above the noise obtained. Nevertheless, more electrodes does not necessarily mean better performance, since this array did not gave good results for the CC and NRMSE values.

On the other hand, in the literature and some other works on decodification, the time range of delays reaches from 0.5 s to 1.5 s. However, the brain signal potentials related to the voluntary movements, such as the preparation potentials or premotor potential (Bereitschaftspotential, BP in German), happen approximately 2 seconds before the beginning of the movement. And in a work of Úbeda et al. [62], it is mentioned that the performance improves between 2 s and 2.5 s. This helps the assumption that longer time delays contribute to the motion planning in the brain, meanwhile immediate delays could be related to the execution of the movement. This is why in Table 4.1, the time delays have a wider range, compare to literature, from 2 s to 4.5 s.

In the case of decoding kinematics by segments, creating different MLR models according to the action performed seems to give better results than using a single one. However, as can be seen in Tables 4.2 to 4.4, the decoders gave better performance for the joint angle the subject focused on moving. That is, in Task 1 the subject focused on extending the knee and the multiple decoders improved better for that joint angle specifically; meanwhile the decodification of the other joint angle gave mixed results between subjects. Similarly during Task 2, the decoders improved for the hip decodification, giving mixed results for the knee joint angle decodification between subjects. This could mean that only the joint angle of the limb movement in which the subject is focusing is embedded in the EEG signal, and the decodification of the other joint angle is not entirely embedded in the EEG signal. Also the current results of CC, NRMSE and SNR, although good, might not reveal the desired movement accurately. This could be appreciated in the transitioning of the MLRs for each action. If there is an abrupt transition, it might lead to a bad outcome of the output signal. Also, in this work, the specific periods of each action were known for the testing of the decoder since it is a complete and strictly offline study.

Another exhaustive search for the best suited parameters was held but applied to the decodification by segments of the synchronous protocols. Following a similar procedure of combining electrodes and time delays; however, this second search involved the different number of gaps in such delays. It can be appreciated in Figure 4.33 that the electrodes that mainly contribute to the decodification are located at the center of the scalp, that is, areas F, C, and P of the international 10-20 system. It is important to mention that the electrode Cz is always present for the best decodifications. This appears to be logical, based on the fact that Cz is the electrode located nearest to the leg area of the primary motor cortex of the brain. As for Figure 4.34, it can be seen that the information of movement in the electrical activity is located around 2.5 s before the movement, and the number of data samples required to obtain a better decodification is 8 or 9.

To optimize the decodification by segments, a transformation of the EEG signals was performed using five simple nonlinear functions. However, only using nine electrodes, the possible combinations for these transformations were an enormous quantity. For this reason, a genetic algorithm (GA) was used. The GA worked in order to find the most appropriate combination of transformation functions for each test subject. As shown in Tables 4.8 and 4.9, the evaluation metrics do show improvement for most subjects. The exceptions been subjects 5 and 7 for Task 1, which remained constant on not using any transformation for the decodification. Nevertheless, although the evaluation metrics show improvement with the transformation functions, there are some unexpected noisy behaviors of the decoded joint angle. This can be appreciated on some of the Figures 4.36 to 4.50, mostly during the resting periods. With these results it can be seen that for most subjects, applying transformations to the signal of each electrode has improvements. However, in this thesis only simple transformations functions were considered.

The contributions of this thesis have provided an enhancement in the understanding of the dynamical behavior of the EEG signals, as well as opening new possibilities to apply more appropriate decodification methods.

Usually the nonlinear dynamical analysis of the EEG signals is used to characterize between mental states, rather than being applied to understand the behavior of the brain signals during common movements of an individual. With the understanding of the dimensionality and persistent behavior of the EEG signals during lower limb movement in short intervals, more appropriate preprocessing of the signal could be performed. For example, the dimensionality could be reduced for the decoders to be more simpler. Along these lines, using simpler decoders could also mean the usage of smaller sampling frequencies. This could be applied in order to avoid over-fitness of the decoder. Applying simple decoders to BCIs or BMIs, allows for the computational load to be smaller, thus allowing the interface to be more user accessible.

This thesis continues to demonstrate the feasibility of applying linear decoders in order to reconstruct the trajectories of lower limbs by noninvasively acquired brain signals. The fact that the decoder remains linear allows for the BCIs or BMIs to use multiple decoders for different tasks without overloading the computational capacity. Also the usage of several simultaneous decoders co-working, grants the user to reduce the training. Thus allowing a disabled individual to incorporate to the casual daily living in a more faster time.

5.2 Future Work

The three selected indices in this thesis provided insight of the underlying system of the brain. The H values suggest that the system is nonrandom and persistent on average for short time intervals. The CD values allowed to determine that the dimension of the dynamical system lies between 4 or 6. Furthermore, the positive LLE values suggest that the underlying dynamics is indeed nonlinear. These values apply for individual electrodes, making the assumption that if the cortical regions interact between each other the brain tends to be a nonlinear system of higher dimension. With these insights, we could define a nonarbitrary selection of a candidate model to classify motion tasks and/or to resolve the continuous trajectory reconstruction of lower limb kinematics. This selection could provide more reliable and affined methods for EEG-based BCI systems to manipulate assistive devices useful in neuromuscular rehabilitation.

The exhaustive searches for better parameters of the decodification led to find that the cortical region C, specially electrode Cz, is indispensable for lower limb kinematic decodification. However, the number of electrodes varies from the international 10/10 system to the 10/20 system. Perhaps, using more electrodes on this region provides a better performance, which could be possible to achieve using the 10/5 system. Other neighbor regions also contribute to the decodification, specifically cortical regions F and P, where the latter appear to have more relevance. With these considerations, only a limited numbers of electrodes could be needed in future works, focusing to cover the F, C, and P regions. The other parameters could be helpful in future studies, where the delay and number of data samples considered could also help to establish better experimental setups, e.g., longer periods between tasks, or different lengths of task execution.

Using different MLR models for the different actions proved to give better results in CC, NRMSE, and SNR values. However, the transitioning between MLR models should be taken into consideration. Also, since this work was strictly offline, the different action periods were known. On the other hand, the decoders seemed to give a good performance for the appointed joint angle of the task performed. This could mean that the slow cortical potentials only have embedded an specific limb movement. Further study involving different tasks simultaneously should be taken in consideration for the future. Along this lines, a better transitioning between models should be considered. Furthermore, the classification of each action could be obtained during the testing period in order to perform the appropriate decodification without prior knowledge of the action. All of these considerations should be taken into account in order to focus the study into future BCI applications, be them prosthetic, using exoskeletons, or virtual reality rehabilitation.

The transformations performed to the electrodes individually, found by the GA, proved to give a better performance for the decodification. However, only simple nonlinear functions were applied. In the future, more complex nonlinear functions could be applied for better manipulation of the EEG signals. Also, interaction effects between electrodes should be considered. This comes from the idea that somatosensory cortex could give a certain degree of information that could be used to give another type of signal in contrast to the somatomotor cortex.

5.3 SCIENTIFIC PRODUCTION

5.3.1 JOURNAL PAPERS

- L. Mercado, G. Quiroz, and J. M. Azorín. Analyzing the performance of segmented decoding of lower limb movements from EEG signals with combinations of electrodes, gaps, and delays. Biomedical Signal Processing and Control. **Status**: Evaluation.

- G. Quiroz, A. Espinoza-Valdez, R.A. Salido-Ruiz, L. Mercado. Coherence analysis of EEG in locomotion using graphs. Revista Mexicana de Ingeniería Biomédica. Vol. 38, No. 1, Jan-Apr 2017, pp 235-246
  Status: Published.

5.3.2 BOOK CHAPTER

- Andreas Wulff-Abramsson, Adam Lopez, and Luis Mercado. Paint With Brainwaves – A step towards a low brain effort active BCI painting prototype. Human-Computer Interaction Series. Springer 2019.
  Status: Published.

5.3.3 Divulgation papers

- Luis Mercado. Decoding kinematic variables from Electroencephalographic (EEG) signals during lower-limb mobility protocols. Vol. 3, Núm. 2 (2017): Revista Doctorado UMH - Ciencia y Tecnología.
  Status: Published.

5.3.4 Scientific conferences

- Luis Mercado, J.M. Azorín, Miguel Platas, A. Úbeda, and Griselda Quiroz. Offline Lower-Limb Kinematic Decodification by Segments of EEG Signals. 2018 40th Annual International Conference of the IEEE Engineering in Medicine and Biology Society (EMBC). Honolulu, Hawaii, 2018.
  Status: Published.
- L. Mercado, A. Úbeda, G. Quiroz, J.M. Azorín. Análisis de las regiones corticales y rangos de tiempos para la decodificación del movimiento de rodilla a partir de señales EEG. IX Congreso Iberoamericano de Tecnología de Apoyo a la Discapacidad (iberdiscap 2017).
  Status: Published.
- G. Quiroz, Aurora Espinoza-Valdez, Ricardo A. Salido-Ruiz, Luis Mercado. Estudio de Coherencia de Señales Electroencefalográficas en Locomoción Mediante Grafos. XXXIX Congreso Nacional de Ingeniería Biomédica (CNIB2016).
  Status: Published.
- Luis Mercado, Angel Rodriguez-Liñan, Luis M. Torres-Treviño, and G. Quiroz. Hybrid BCI Approach to Control an Artificial Tibio-Femoral Joint. 2016 38th Annual International Conference of the IEEE Engineering in Medicine and Biology Society (EMBC). Orlando, FL, 2016, pp. 2760-2763.
  doi: 10.1109/EMBC.2016.7591302
  Status: Published.

5.3.5 Research internships

- At Brain-Machine Interface Systems Lab in the Miguel Hernández University (UMH), Elche, Spain.

Time period: March 15, 2017-January 15, 2018.

Coursed: Bases de la Investigación Científica.

- At Centro Universitario de Ciencias Exactas e Ingenierías (CUCEI) in the Universidad de Guadalajara (UDG), Jalisco, México.

  Time period: September 5-16, 2016.

APPENDIX A

ARTICLE

The quality index associated to this Doctoral Thesis corresponds to the contribution named “Offline Lower-Limb Kinematic Decodification by Segments of EEG Signals” presented in the international conference “40th International Conference of the IEEE Engineering in Medicine and Biology Society” and published in the conference proceedings.

AUTHORS Luis Mercado, J.M. Azorín, *Senior Member, IEEE*, Miguel Platas, A. Úbeda, and Griselda Quiroz

ABSTRACT

In this work, hip and knee angles were decoded from low frequency EEG components recorded during the execution of two tasks. In order to compare their performance, three decoders based on multiple linear regression (MLR) models were applied under different conditions; which consisted in considering the processed data as a whole or divided into segments. Results suggest that, when the segments are related to specific tasks, the segmentation provides a better performance than applying the decoding method to unsegmented data.

Luis Mercado, Miguel Platas & Griselda Quiroz are with the Universidad Autónoma de Nuevo León, FIME, Av. Universidad S/N, Ciudad Universitaria, C.P. 66455, San Nicolás de los Garza, Nuevo León, México. Phone: +52 81 83294020 ext. 5773.

J. M. Azorín is with the Brain-Machine Interface Systems Lab, Universidad Miguel Hernández de Elche, Av. de la Universidad S/N, 03202 Elche, Spain.

A. Úbeda is with the Department of Physics, Systems Engineering and Signal Theory, University of Alicante, Carretera de San Vicente del Raspeig S/N 03690 San Vicente del Raspeig, Alicante, Spain.

I Introduction

According to the Centers for Disease Control and Prevention (CDC) in 2015, there were about 18.2 million adults in the United States unable (or had difficulty) to walk a quarter mile [108]. And the American FactFinder reported in 2016 that 21.1 million adults had an ambulatory difficulty [2]. The European Union reported in 2015 that there were around 11.8 million people with difficulty walking and around 7.2 million with difficulty sitting or standing [3]. Therefore, it comes to interest to restore the mobility of this growing population, by means of improving the technological options such as a neural machine interface (NMI). A NMI uses bioelectrical signals in order to activate or manipulate an external device. The case of using brain signals to operate a computer is called a brain-computer interface (BCI) [109]. Electroencephalography (EEG), a non-invasive technique to record the neural activity of the brain, has been used to interpret the motion intent of the user of a BCI [110]. Many BCI studies have been done in the past decade, for example, in 2013 Do et al. [29], integrated a BCI system with a robotic gait orthosis (RoGO). He et al. [27], were able to decode kinematics and kinetics of the lower-limb joints during walking using an exoskeleton. In a similar way, Úbeda et al. [41], successfully decoded angles of the knee using brain signals during treadmill walking. These limited number of studies have implemented decoding schemes; nevertheless, they just decode a single type of task. The mentioned studies show results of the decoding of the lower limb kinematics obtained with actual walking, and using conventional EEG equipment.

In this paper, several linear regression models were used to decode the hip and knee angles from low frequency EEG signals (0.1-2 Hz) [42, 62]. These models were created under different conditions, which are: treating the process data as a whole or dividing it into segments.

For the experimental tests, subjects were asked to raise the foot or knee while remaining seated, meanwhile the associated cortical information was recorded through EEG. The decoded hip and knee angles were then compared to the actual ones in order to evaluate the performance of the models. This paper is organized as follows: the experimental setup, data acquisition, signal processing, and decoding methods are in section 2. The results are shown in Section 3. Section 4 is devoted to the discussion. Finally, in Section 5 some concluding remarks are presented.

II Materials and Methods

II.a Experimental Setup

Nine subjects (4 male and 5 female) with no motor pathologies were asked, and gave consent, to perform the trials. The experimental procedures involving human subjects described in this paper were approved by the Institutional Review Board. Subjects were asked to realize two lower-limb tasks. The first task consisted in raising the foot, and the second task in raising the knee, both performed while remaining seated. The trial began with the resting period, were the subject was sitting comfortably on a chair maintaining the thigh in an horizontal position and the shank around 90° with respect to the thigh. After 30 seconds have passed, the subject raised the right foot (Trial type 1) or knee (Trial type 2) to its maximum position, holding the limb up for 3 seconds. After said period, the subject lowered the limb maintaining this position for another 3 seconds. After 10 repetitions, the subject rested for another 30 seconds. To have the trials controlled, the subjects were shown a video with indicators to perform the different activities. This video consisted of different simple illustrations that indicate the activities, such as the resting period, that helps the subject to focus on a single white dot in order to not get distracted. Followed by 10 repetitions of green-upward and red-downward arrows, to indicate the raising and lowering of the limb. And it also has start and finish frames.

II.b Data Acquisition

For the acquisition of the neural signals, the MOBITA-W-32EEG system was used. The Mobita® was adapted to the Electro-Cap to give out 19 EEG channels. After placing the cap on the subjects, the impedance of the electrodes was checked using the Model 1089NP Checktrode$^{\text{TM}}$. The desired impedance range was: less than $5K\Omega$ which means a good preparation, according to the specifications of the product, or between $5K\Omega$ to $10K\Omega$ meaning it was an OK preparation. During the EEG recording, markers indicating the raising and lowering of the limb were added on the software in order to specify the beginning and ending of the activity. For the acquisition of the kinematic variables, the subjects were placed in a controlled environment and wore dark clothes and three white spherical markers (Figure A.1). The markers were allocated on the right hip, knee and ankle, in order to give their locations by the processing of the video taken by a NI 1752 Smart Camera running at 60 frames per second (fps).

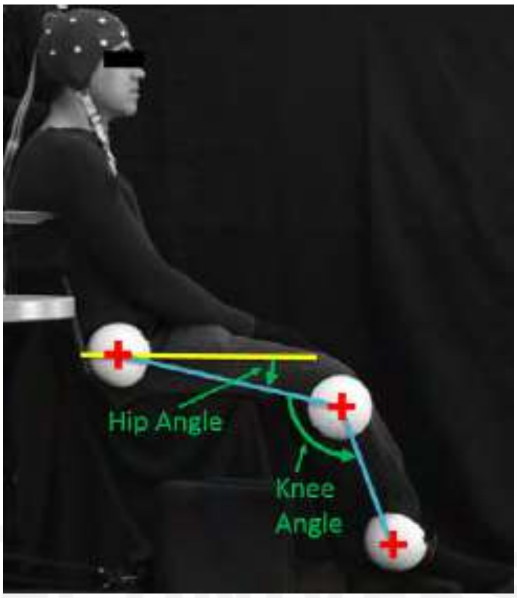

Figure A.1: Test subject wearing three spherical markers allocated on the right hip, knee and ankle, for video processing.

II.c Signal Preprocessing

To prepare any EEG signal for further processing, it was decided to use the computational method of fast independent component analysis (FastICA). This method was implemented in order to separate the artifacts (blinks) embedded in the data. Although 19 electrode locations were recorded, only 9 located in the frontal, central and parietal cortex (F3, Fz, F4, C3, Cz, C4, P3, Pz, and P4) were selected. Afterwards, these 9 channels were filtered using two elliptic filters, one 5th order low-pass below 2 Hz, and a 3rd order high-pass above 0.1 Hz. Finally, the EEG data of each electrode was standardized with the following equation ($EV[t]$) by subtracting, for each time sample (t), the mean ($\bar{V}$) of the signal, and dividing the result by the standard deviation (SD_V) as seen in Equation A.1.

$$EV[t] = \frac{V[t] - \bar{V}}{SD_V}. \tag{A.1}$$

As for the kinematic variables, the hip and knee angles were calculated using the center of each marker (as shown in Figure A.1) and upsampled to match the 1000 Hz of the EEG signal.

II.D DECODING METHOD

To decode individual joint angles from low frequency EEG components a multiple linear regression (MLR) was applied, which has the following formula:

$$x[t] = a + \sum_{n=1}^{N} \sum_{k=0}^{L} b_{nk} S_n[t - Gk] \tag{A.2}$$

where $x[t]$ is the joint angle at time t and S_n is the voltage measured at electrode n. N are the number of channels, L are the number of lags, G is the gap between lags, and a and b are the weights of the linear regression. L was limited to 10 and N corresponds to 9 of the electrodes introduced in the decoder. The gap used was of 250, which multiplied with the maximum lag reached 2500 samples ($2.5s$) in the past of the current sample.

III RESULTS

As stated, the subjects performed two type of trials: raising the foot and the knee while remaining seated, separately. In this approach different decoders were created: Decoder 1 (D1) used a single MLR to decode all the trial involving the three activities of resting, raising, and lowering. Decoder 2 (D2) used a pair of transitioning MLRs, one for the resting periods, and another for the movement period. Decoder 3 (D3) used three MLRs, one for the resting periods, and two separate decoders for raising and lowering of the movement periods. This can be visualized in Figure A.2.

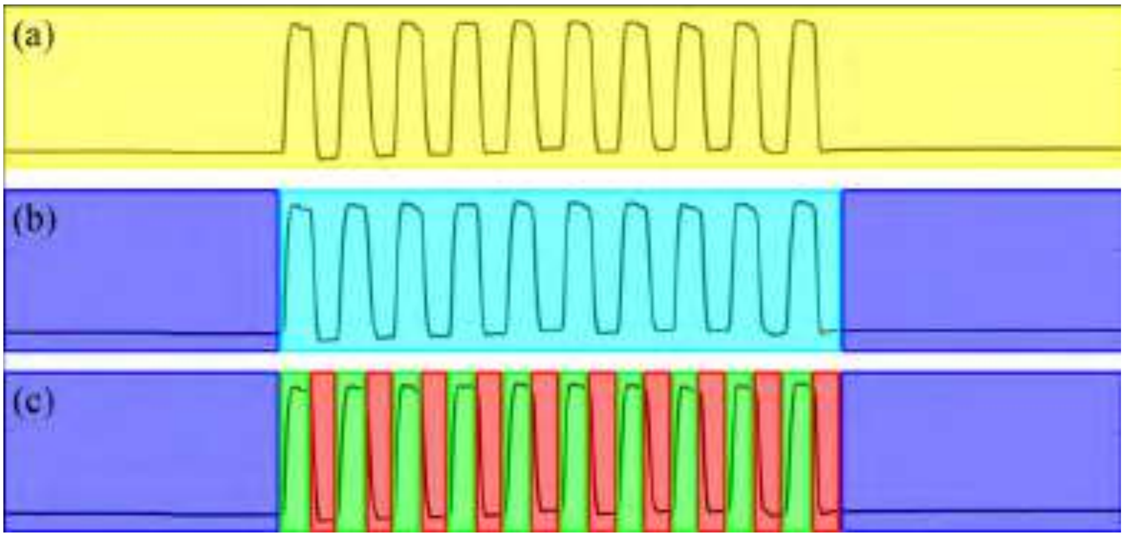

Figure A.2: Illustrative sections for which a MLR was created. The same angles are displayed in order to illustrate the sections: (a) Decoder 1 (D1) where yellow corresponds to a single MLR for all activities, (b) Decoder 2 (D2) where blue corresponds to resting periods, and cyan to the movement period, (c) Decoder 3 (D3) where blue corresponds to resting periods, green for the raising and red for the lowering period.

Three trials of each test subject were used for training to obtain the decoder, and one trial was used for testing. The selected metrics to evaluate the performance of the decodifications were the Pearson correlation coefficient (CC), Normalized Root Mean Square Error (NRMSE), and the Signal-Noise Ratio (SNR). These metrics along with their mean and standard deviations, for each subject and trial type are shown in Tables A.1-A.3. In Figure A.3 it can be seen the best decodification regarding the three metrics.

CC	Trial type 1					
Subject	Hip decoders			Knee decoders		
	D1	D2	D3	D1	D2	D3
1	0.2132	0.9106	0.9351	0.2541	0.7228	0.9318
2	0.5935	0.6134	0.6251	0.2758	0.7022	0.9444
3	0.1750	0.6557	0.8489	0.1749	0.6780	0.8461
4	0.3453	0.0433	0.0626	0.3087	0.7292	0.9145
5	-0.0043	0.0263	0.0993	-0.1068	0.3486	0.7177
6	0.2065	0.4734	0.4466	0.1560	0.5991	0.9060
7	0.3114	0.7338	0.8911	0.3305	0.7302	0.9052
8	0.1565	0.3925	0.5385	0.1385	0.7026	0.8742
9	-0.0076	0.2508	0.5160	-0.0200	0.5079	0.8318
μ	0.2211	0.4555	0.5514	0.1680	0.6356	0.8746
σ	0.1844	0.3062	0.3186	0.1488	0.1304	0.0697
	Trial type 2					
Subject	Hip decoders			Knee decoders		
	D1	D2	D3	D1	D2	D3
1	0.0386	0.5449	0.8479	0.0492	0.6250	0.8326
2	0.5039	0.8399	0.9142	0.2660	0.5135	0.6232
3	0.2734	0.7408	0.8723	0.2696	0.7441	0.8753
4	0.4125	0.7581	0.9093	0.2549	0.4435	0.5906
5	0.1508	0.4636	0.7624	0.0875	0.5108	0.6969
6	0.3260	0.7183	0.9077	0.3168	0.7006	0.8649
7	0.4323	0.7826	0.9206	0.3919	0.7779	0.9046
8	0.1569	0.6549	0.8897	0.1549	0.6759	0.8883
9	0.3936	0.7756	0.9279	0.3771	0.7502	0.9027
μ	0.2987	0.6976	0.8835	0.2409	0.6379	0.7977
σ	0.1553	0.1222	0.0520	0.1206	0.1217	0.1255

Table A.1: Pearson correlation coefficient (CC) values of the decodifications of the hip and knee angles for nine subjects and their mean and standard deviations for trial types 1 and 2. D1-D3 stand for the decoder used.

NRMSE	Trial type 1					
Subject	Hip decoders			Knee decoders		
	D1	D2	D3	D1	D2	D3
1	0.3016	0.1467	0.1332	0.3693	0.2621	0.1382
2	0.1386	0.1390	0.1397	0.3589	0.2611	0.1223
3	0.3443	0.2662	0.1948	0.3592	0.2679	0.2031
4	0.1432	0.1701	0.1697	0.3731	0.2686	0.1592
5	0.3136	0.3293	0.3525	0.4030	0.3886	0.2739
6	0.1239	0.1145	0.1186	0.3722	0.3014	0.1597
7	0.3450	0.2515	0.1753	0.3521	0.2565	0.1645
8	0.7377	0.7305	0.7292	0.3751	0.2812	0.2139
9	0.5601	0.5686	0.5856	0.4008	0.3425	0.2178
μ	0.3342	0.3018	0.2887	0.3737	0.2922	0.1836
σ	0.2045	0.2129	0.2229	0.0177	0.0452	0.0474
	Trial type 2					
Subject	Hip decoders			Knee decoders		
	D1	D2	D3	D1	D2	D3
1	0.4016	0.3422	0.2234	0.4000	0.3284	0.2720
2	0.2776	0.1740	0.1332	0.2676	0.2491	0.2426
3	0.3425	0.2391	0.1755	0.2913	0.2035	0.1555
4	0.3251	0.2417	0.1588	0.2798	0.2820	0.2720
5	0.3283	0.3311	0.2441	0.3166	0.2864	0.2417
6	0.3295	0.2444	0.1462	0.2574	0.1941	0.1361
7	0.2711	0.1919	0.1232	0.3012	0.2310	0.1895
8	0.3567	0.2726	0.1671	0.3459	0.2582	0.1652
9	0.3266	0.2248	0.1334	0.2796	0.2015	0.1302
μ	0.3288	0.2513	0.1672	0.3044	0.2482	0.2005
σ	0.0391	0.0565	0.0417	0.0447	0.0455	0.0572

Table A.2: Normalized root mean square error (NRMSE) values of the decodifications of the hip and knee angles for nine subjects and their mean and standard deviations for trial types 1 and 2. D1-D3 stand for the decoder used.

SNR	Trial type 1					
Subject	Hip decoders			Knee decoders		
	D1	D2	D3	D1	D2	D3
1	0.0660	4.8023	7.5955	0.1446	1.1483	6.9661
2	0.8047	1.0010	1.2076	0.2627	1.2316	8.3188
3	0.0845	1.0615	3.4154	0.0867	1.0538	3.3091
4	0.1198	0.2819	0.3125	0.1600	1.2398	4.8973
5	0.0547	0.1986	0.4409	0.1132	0.6402	1.7562
6	0.1006	0.5210	0.6138	0.1040	0.7984	4.7015
7	0.0725	1.2278	3.8479	0.1262	1.3141	5.2767
8	0.0408	0.5050	1.2274	0.0313	1.0217	4.0348
9	0.1146	0.5723	1.2355	0.0507	0.5771	2.4405
μ	0.1620	1.1301	2.2107	0.1199	1.0028	4.6334
σ	0.2425	1.4220	2.3806	0.0677	0.2702	2.0830

SNR	Trial type 1					
Subject	Hip decoders			Knee decoders		
	D1	D2	D3	D1	D2	D3
1	0.1797	0.9921	3.3389	0.1503	1.0912	2.9009
2	0.5916	2.8349	5.8515	0.3970	0.7395	1.2041
3	0.1016	1.1737	3.4835	0.1289	1.5161	4.1045
4	0.4208	2.0321	5.7645	0.5063	0.9903	1.4626
5	0.3849	1.0746	2.3876	0.2019	0.9461	1.6554
6	0.2323	1.4419	5.1985	0.1970	1.2177	3.2991
7	0.3197	2.0092	5.6284	0.2182	1.7077	3.8768
8	0.0638	0.8850	4.4156	0.0646	0.9454	4.3786
9	0.1159	1.2583	6.1902	0.0999	0.9138	3.8707
μ	0.2678	1.5224	4.6954	0.2182	1.1186	2.9725
σ	0.1754	0.6428	1.3487	0.1440	0.3117	1.2317

Table A.3: Signal-Noise Ratio (SNR) values of the decodifications of the hip and knee angles for nine subjects and their mean and standard deviations for trial types 1 and 2. D1-D3 stand for the decoder used.

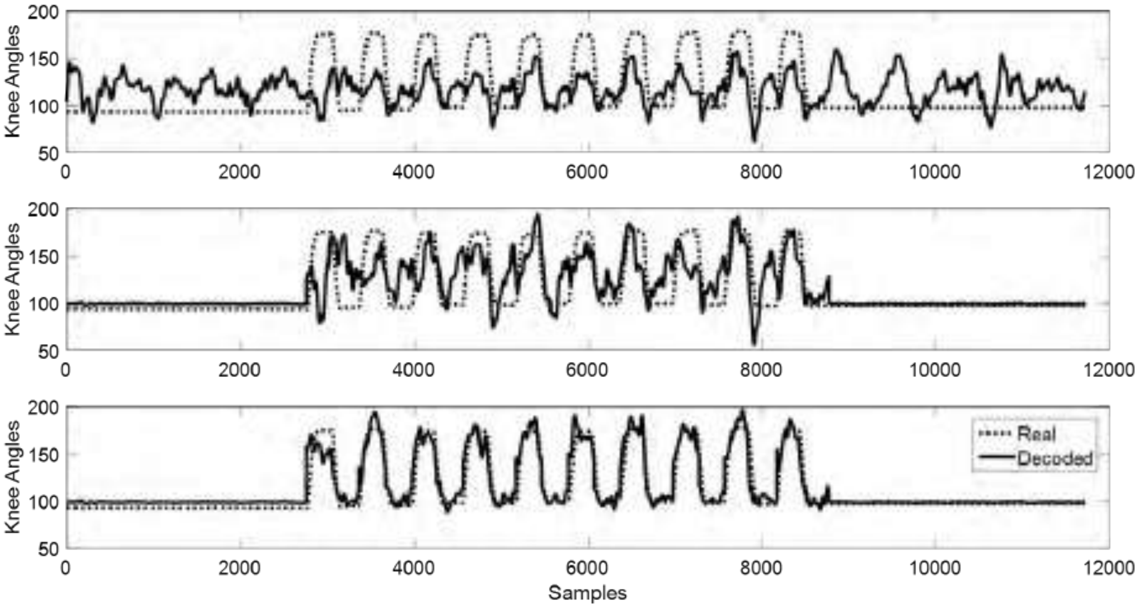

Figure A.3: Decodification of the knee angles using three decoders. From top to bottom: Decoder 1 (D1), Decoder 2 (D2), and Decoder 3 (D3). As illustrated in Figure A.2.

IV Discussion

In the case of decoding kinematics, creating different MLR models according to the action performed seems to give better results than using a single one. As can be seen in the increasing mean values of CC and SNR, and the decreasing mean values of NRMSE. In some occasions a single MLR gave a higher CC value than the decodification done by two or three; however, the NRMSE and SNR values proved that this was misleading. Nevertheless, the current results of CC, NRMSE and SNR, although good, might not reveal the desired movement accurately. This could be appreciated in the transitioning of the MLRs for each action. If there is an abrupt transition, it might lead to a bad outcome of the output signal. Also, in this work, the specific periods of each action were known for the testing of the decoder since it is a complete and strictly offline study.

V Concluding remarks

Using different MLR models for the different actions proved to give better results in CC, NRMSE and SNR values. However, the transitioning between MLR models should be taken into consideration. Also, since this work was strictly offline, the different action periods were known. For future work, a better transitioning between models should be considered. Furthermore, the classification of each action could be obtained during the testing in order to perform the appropriate decodification without prior knowledge of the action. All of these considerations should be taken into account in order to focus the study into future BCI applications, be them prosthetic, using exoskeletons or virtual reality rehabilitation.

Acknowledgment

Authors would like to thank Laboratorio de Procesamiento de Señales Biomédicas on Cinvestav-Mty for lending the MOBITA-W-32EEG system.

Funding

Authors are members of the research network ”Biosystems and Biomechatronics” and thank to PRODEP-SEP for financial support (grant 103.5/15/14156). Luis Mercado and G. Quiroz thank the National Council of Science and Technology (CONACYT) for granting the scholarship number 401834 and grant number 220187, respectively. This research was carried out in the framework of the project Associate - Decoding and stimulation of motor and sensory brain activity to support long term potentiation through Hebbian and paired associative stimulation during rehabilitation of gait (DPI2014-58431-C4-2-R), which is funded by the Spanish Ministry of Economy and Competitiveness and by the European Union through the European Regional Development Fund (ERDF), “A way to build Europe”.

References

[1] CDC/National Center for Health Statistics, “Disability and Functioning (Non-institutionalized Adults Aged 18 and Over),” May 2017. [Online; accessed April-09-2018].

[2] American Community Survey (ACS), “2016 american community survey 1-year estimates,” 2016. [Online; accessed April-12-2018].

[3] EUROSTAT, "Your key to European statistics," [Online; accessed April-12-2018].

[4] L. R. Hochberg, M. D. Serruya, G. M. Friehs, J. A. Mukand, M. Saleh, A. H. Caplan, A. Branner, D. Chen, R. D. Penn, and J. P. Donoghue, "Neuronal ensemble control of prosthetic devices by a human with tetraplegia," *Nature*, vol. 442, pp. 164–171, 2006.

[5] S. Waldert, T. Pistohl, C. Braun, T. Ball, A. Aertsen, and C. Mehring, "A review on directional information in neural signals for brain-machine interfaces," *J. Physiol. (Paris)*, vol. 103, pp. 244–254, 2009.

[6] A. H. Do, P. T. Wang, C. E. King, S. N. Chun, and Z. Nenadic, "Brain-computer interface controlled robotic gait orthosis," *Journal of NeuroEngineering and Rehabilitation*, vol. 10, pp. 1–9, 2013.

[7] Y. He, K. Nathan, A. Venkatakrishnan, R. Rovekamp, C. Beck, R. Ozdemir, G. E. Francisco, and J. L. Contreras-Vidal, "An Integrated Neuro-Robotic Interface for Stroke Rehabilitation using the NASA X1 Powered Lower Limb Exoskeleton," in *2014 36th Annual International Conference of the IEEE Engineering in Medicine and Biology Society (EMBC)*, pp. 3985–3988, 2014.

[8] A. Úbeda, D. Planelles, A. Costa, E. Hortal, E. Iáñez, and J. M. Azorín, "Decoding knee angles from EEG signals for different walking speeds," in *2014 IEEE International Conference on Systems, Man, and Cybernetics (SMC)*, pp. 1475–1478, October 2014. DOI: 10.1109/SMC.2014.6974123.

[9] A. Presacco, R. Goodman, L. Forrester, and J. L. Contreras-Vidal, "Neural decoding of treadmill walking from noninvasive electroencephalographic signals," *Journal of Neurophysiology*, vol. 106, pp. 1875–1887, July 2011. doi:10.1152/jn.00104.2011.

[10] A. Úbeda, A. Costa, E. Iáñez, E. Piñuela-Martín, E. Márquez-Sánchez, A. J. del Ama, A. Gil-Agudo, and J. M. Azorín, "Single joint movement decoding from EEG in healthy and incomplete spinal cord injured subjects," in *2015 IEEE/RSJ International Conference on Intelligent Robots and Systems (IROS)*, pp. 6179–6183, October 2015. DOI: 10.1109/IROS.2015.7354258.

BIBLIOGRAPHY

[1] World Health Organization (WHO). World report on disability 2011, [Online; accessed 17-February-2015]. `http://www.who.int/entity/disabilities/world_report/2011/report.pdf`.

[2] EUROSTAT. Your key to European statistics, [Online; updated March 23, 2019; accessed April 15, 2019]. `http://appsso.eurostat.ec.europa.eu/nui/show.do?dataset=hlth_dp040&lang=en`.

[3] Danielle M. Taylor. Americans with disabilities: 2014. Current Population Reports P70-152, U.S. Census Bureau, Washington, DC, November 2018.

[4] ESCAP Social Development Division. Disability at a Glance 2015: Strengthening Employment Prospects for Persons with Disabilities in Asia and the Pacific. Technical report, United Nations Economic and Social Commission for Asia and the Pacific, Bangkok, 2015.

[5] World Health Organization (WHO). Congenital anomalies. Fact sheet N°370. `http://www.who.int/mediacentre/factsheets/fs370/en/`, January 2014. [Online; accessed 17-February-2015].

[6] Division of Birth Defects and Developmental Disabilities, NCBDDD, Centers for Disease Control and Prevention. Data & Statistics. `http://www.cdc.gov/ncbddd/birthdefects/data.html`. [Online; page last reviewed: April 30, 2018; accessed April 15, 2019].

[7] World Health Organization (WHO). Spinal cord injury. `https://www.who.int/en/news-room/fact-sheets/detail/spinal-cord-injury`, November 2013. [Online; accessed April 15, 2019].

[8] Judith Mackay and George A. Mensah. The atlas of heart disease and stroke. Technical report, World Health Organization & Centers for Disease Control and Prevention (U.S.), 2004.

[9] J.P. Gutiérrez, J. Rivera-Dommarco, T. Shamah-Levy, S. Villalpando-Hernández, A. Franco, L. Cuevas-Nasu, M. Romero-Martínez, and M. Hernández-Ávila. Encuesta nacional de salud y nutrición 2012. Resultados nacionales, Instituto Nacional de Salud Pública (MX), Cuernavaca, México, 2012.

[10] Laura E Mitchell, N Scott Adzick, Jeanne Melchionne, Patrick S Pasquariello, Leslie N Sutton, and Alexander S Whitehead. Spina bifida. *The Lancet*, 364(9448):1885–1895, November 2004.

[11] National Center on Birth Defects and Developmental Disabilities, Centers for Disease Control and Prevention. What is Spina Bifida? `https://www.cdc.gov/ncbddd/spinabifida/facts.html`. [Online; page last reviewed: September 13, 2018; accessed April 15, 2019].

[12] Division of Birth Defects and Developmental Disabilities, NCBDDD, Centers for Disease Control and Prevention. Birth Defects. Facts about Upper and Lower Limb Reduction Defects. `https://www.cdc.gov/ncbddd/birthdefects/ul-limbreductiondefects.html`. [Online; page last reviewed: April 20, 2018; accessed April 15, 2019].

[13] World Health Organization (WHO). Stroke, Cerebrovascular accident. `http://www.who.int/topics/cerebrovascular_accident/en/`. [Online; accessed April 15, 2019].

[14] National Center on Birth Defects and Developmental Disabilities , Centers for Disease Control and Prevention. Spina Bifida. Health Issues & Treatments. `https://www.cdc.gov/ncbddd/spinabifida/treatment.html`. [Online; page last reviewed: January 30, 2019; accessed April 15, 2019].

[15] Russell Thomas Frood. The use of treadmill training to recover locomotor ability in patients with spinal cord injury. *Bioscience Horizons*, 4:108–117, February 2011. doi:10.1093/biohorizons/hzr003.

[16] Belda-Lois et al. Rehabilitation of gait after stroke: a review towards a top-down approach. *Journal of NeuroEngineering and Rehabilitation*, 8:66, 2011. doi:10.1186/1743-0003-8-66.

[17] Saeid Sanei and J. A. Chambers. *EEG signal processing.* John Wiley & Sons Ltd, 2007.

[18] Duk Shin, Yasuhiko Nakanishi, Chao Chen, Hiroyuki Kambara, Natsue Yoshimura, and Yasuharu Koike. Decoding of Kinetic and Kinematic Information from Electrocorticograms in Sensorimotor Cortex: A Review. *International Journal of Neurorehabilitation*, 1(102), 2014. doi:10.4172/ijn.10001102.

[19] Jinhua Zhang, Jiongjian Wei, Baozeng Wang, Jun Hong, and Jing Wang. Nonlinear EEG Decoding Based on a Particle Filter Model. *BioMed Research International*, 2014:13, 2014. doi:10.1155/2014/159486.

[20] Nathan A. Fitzsimmons, Mikhail A. Lebedev, Ian D. Peikon, and Miguel A. L. Nicolelis. Extracting kinematic parameters for monkey bipedal walking from cortical neuronal ensemble activity. *Frontiers in Integrative Neuroscience*, 3(3), 2009. doi:10.3389/neuro.07.003.2009.

[21] German Rodriguez-Bermudez and Pedro J Garcia-Laencina. Analysis of EEG signals using nonlinear dynamics and chaos: a review. *Applied mathematics & information sciences*, 9(5):2309, 2015.

[22] U. Rajendra Acharya, Vidya K. Sudarshan, Hojjat Adeli, Jayasree Santhosh, Joel E.W. Koh, and Amir Adeli. Computer-aided diagnosis of depression using EEG signals. *European Neurology*, 73:329–336, 2015.

[23] Sutrisno Ibrahim, Khalil AlSharabi, Ridha Djemal, and Abdullah Alsuwailem. An Adaptive Learning Approach for EEG-Based Computer Aided Diagnosis of Epilepsy. In *2016 International Seminar on Intelligent Technology and Its Application (ISITIA)*, pages 55–60, 2016.

[24] Roxana Toderean Aldea, Oana Geman, Iuliana Chiuchisan, and Anca Mihaela Lazar. A comparison between healthy and neurological disorders patients us-

ing nonlinear dynamic tools. In *2016 International Conference and Exposition on Electrical and Power Engineering (EPE)*, pages 299–303, 2016.

[25] Gaojie Yu, Jianhua Wang, Weihai Chen, and Jianbin Zhang. EEG-based brain-controlled lower extremity exoskeleton rehabilitation robot. In *2017 IEEE International Conference on Cybernetics and Intelligent Systems (CIS) and IEEE Conference on Robotics, Automation and Mechatronics (RAM)*, pages 763–767, 2017.

[26] Khaled Sayed, Mahmoud Kamel, Mohammed Alhaddad, Hussein M. Malibary, and Yasser M. Kadah. Characterization of phase space trajectories for brain-computer interface. *Biomedical Signal Processing and Control*, 38:55 – 66, 2017.

[27] Yongtian He, Kevin Nathan, Anusha Venkatakrishnan, Roger Rovekamp, Christopher Beck, Recep Ozdemir, Gerard E. Francisco, and Jose L. Contreras-Vidal. An Integrated Neuro-Robotic Interface for Stroke Rehabilitation using the NASA X1 Powered Lower Limb Exoskeleton. In *2014 36th Annual International Conference of the IEEE Engineering in Medicine and Biology Society (EMBC)*, pages 3985–3988, 2014.

[28] Yongtian He, David Eguren, José M Azorín, Robert G Grossman, Trieu Phat Luu, and Jose L Contreras-Vidal. Brain-machine interfaces for controlling lower-limb powered robotic systems. *Journal of Neural Engineering*, 15(2):021004, 2018.

[29] An H. Do, Po T. Wang, Christine E. King, Sophia N. Chun, and Zoran Nenadic. Brain-computer interface controlled robotic gait orthosis. *Journal of NeuroEngineering and Rehabilitation*, 10:1–9, 2013.

[30] Atilla Kilicarslan, Saurabh Prasad, Robert G Grossman, and Jose L Contreras-Vidal. High accuracy decoding of user intentions using EEG to control a lower-body exoskeleton. In *Engineering in medicine and biology society (EMBC), 2013 35th annual international conference of the IEEE*, pages 5606–5609. IEEE, 2013.

[31] No-Sang Kwak, Klaus-Robert Müller, and Seong-Whan Lee. A lower limb exoskeleton control system based on steady state visual evoked potentials. *Journal of neural engineering*, 12(5):056009, 2015.

[32] Eliana García-Cossio, Marianne Severens, Bart Nienhuis, Jacques Duysens, Peter Desain, Nöel Keijsers, and Jason Farquhar. Decoding sensorimotor rhythms during robotic-assisted treadmill walking for brain computer interface (BCI) applications. *PloS one*, 10(12):e0137910, 2015.

[33] Eduardo López-Larraz, Fernando Trincado-Alonso, Vijaykumar Rajasekaran, Soraya Pérez-Nombela, Antonio J del Ama, Joan Aranda, Javier Minguez, Angel Gil-Agudo, and Luis Montesano. Control of an ambulatory exoskeleton with a brain–machine interface for spinal cord injury gait rehabilitation. *Frontiers in neuroscience*, 10:359, 2016.

[34] Ana RC Donati, Solaiman Shokur, Edgard Morya, Debora SF Campos, Renan C Moioli, Claudia M Gitti, Patricia B Augusto, Sandra Tripodi, Cristhiane G Pires, Gislaine A Pereira, et al. Long-term training with a brain-machine interface-based gait protocol induces partial neurological recovery in paraplegic patients. *Scientific reports*, 6:30383, 2016.

[35] Kyuhwa Lee, Dong Liu, Laetitia Perroud, Ricardo Chavarriaga, and José del R Millán. A brain-controlled exoskeleton with cascaded event-related desynchronization classifiers. *Robotics and Autonomous Systems*, 90:15–23, 2017.

[36] Yuhang Zhang, Saurabh Prasad, Atilla Kilicarslan, and Jose L Contreras-Vidal. Multiple kernel based region importance learning for neural classification of gait states from EEG signals. *Frontiers in neuroscience*, 11:170, 2017.

[37] Thierry Castermans, Matthieu Duvinage, Guy Cheron, and Thierry Dutoit. Towards Effective Non-Invasive Brain-Computer Interfaces Dedicated to Gait Rehabilitation Systems. *Brain Science*, 4:1–48, 2014. doi:10.3390/brainsci4010001.

[38] Ali Bashashati, Mehrdad Fatourechi, Rabab K Ward, and Gary E Birch. A survey of signal processing algorithms in brain-computer interfaces based on

electrical brain signals. *Journal of Neural Engineering*, 4(2):R32–R57, 2007. doi:10.1088/1741-2560/4/2/R03.

[39] Rabie A. Ramadan and Athanasios V. Vasilakos. Brain computer interface: control signals review. *Neurocomputing*, 223:26 – 44, 2017.

[40] K. . Muller, C. W. Anderson, and G. E. Birch. Linear and nonlinear methods for brain-computer interfaces. *IEEE Transactions on Neural Systems and Rehabilitation Engineering*, 11(2):165–169, June 2003.

[41] Andrés Úbeda, Daniel Planelles, Álvaro Costa, Enrique Hortal, Eduardo Iáñez, and José M. Azorín. Decoding knee angles from EEG signals for different walking speeds. In *2014 IEEE International Conference on Systems, Man, and Cybernetics (SMC)*, pages 1475–1478, October 2014. DOI: 10.1109/SMC.2014.6974123.

[42] Alessandro Presacco, Ronald Goodman, Larry Forrester, and Jose Luis Contreras-Vidal. Neural decoding of treadmill walking from noninvasive electroencephalographic signals. *Journal of Neurophysiology*, 106:1875–1887, July 2011. doi:10.1152/jn.00104.2011.

[43] Thierry Castermans, Thierry Dutoit, and Matthieu Duvinage. Method to Determine an Artificial Limb Movement from an Electroencephalographic Signal. Patent, February 2013. US 2013046715A1.

[44] U. Rajendra Acharya, S. Vinitha Sree, G. Swapna, Roshan Joy Martis, and Jasjit S. Suri. Automated EEG analysis of epilepsy: A review. *Knowledge-Based Systems*, 45:147–165, 2013.

[45] Kannathal Natarajan, Rajendra Acharya U, Fadhilah Alias, Thelma Tiboleng, and Sadasivan K Puthusserypady. Nonlinear analysis of EEG signals at different mental states. *BioMedical Engineering OnLine*, 3(7), 2004.

[46] Kusuma Mohanchandra, Snehanshu Saha, and K. Srikanta Murthy. Evidence of chaos in EEG signals: An application to BCI. In Ahmad Taher Azar and Sundarapandian Vaidyanathan, editors, *Advances in Chaos Theory and Intel-*

ligent Control, volume 337, pages 609–625. Springer International Publishing, 2016.

[47] E.I. Scarlat, Cristina Stan, and C.P. Cristescu. Chaotic features in romanian transition economy as reflected onto the currency exchange rate. *Chaos, Solitons & Fractals*, 33(2):396 – 404, 2007.

[48] Subir Mansukhani. Predictability of time series. *Analytics. Maryland: INFORMS*, pages 29–31, July/August 2012.

[49] Gopika Gopan K, Neelam Sinha, and Dinesh Babu J. EEG signal classification in non-linear framework with filtered training data. In *2015 23rd European Signal Processing Conference (EUSIPCO)*, pages 624–628, Aug 2015.

[50] N. Kannathal, U. Rajendra Acharya, C.M. Lim, and P.K. Sadasivana. Characterization of EEG-A comparative study. *Computer Methods and Programs in Biomedicine*, 80(1):17–23, 2005.

[51] U. Rajendra Acharya, Oliver Faust, N. Kannathal, TjiLeng Chua, and Swamy Laxminarayan. Non-linear analysis of EEG signals at various sleep stages. *Computer Methods and Programs in Biomedicine*, 80(1):37–45, 2005.

[52] Harold Edwin Hurst. Long-term storage capacity of reservoirs. *Transactions of American Society of Civil Engineers*, 116:770–799, 1951.

[53] Francesco Camastra. Data dimensionality estimation methods: a survey. *Pattern Recognition*, 36(12):2945 – 2954, 2003.

[54] Benoit Mandelbrot. How long is the coast of britain? statistical self-similarity and fractional dimension. *Science*, 156(3775):636–638, 1967.

[55] Peter Grassberger and Itamar Procaccia. Measuring the strangeness of strange attractors. *Physica D: Nonlinear Phenomena*, 9(1-2):189–208, 1983.

[56] Mei Ying Boon, Bruce I. Henry, Catherine M. Suttle, and Stephen J. Dain. The correlation dimension: A useful objective measure of the transient visual evoked potential? *Journal of Vision*, 8(1):6, 2008.

[57] Glenn Elert. The Chaos Hypertextbook. `https://hypertextbook.com/chaos/lyapunov-1/`, 1998-2016. [Online; accessed July-24-2018].

[58] Alan Wolf, Jack B. Swift, Harry L. Swinney, and John A. Vastano. Determining lyapunov exponents from a time series. *Physica D: Nonlinear Phenomena*, 16(3):285–317, 1985.

[59] Fernanda Strozzi, Eugénio Gutierrez, Carlo Noè, Tommaso Rossi, Massimiliano Serati, and José Manuel Zaldívar. Application of non-linear time series analysis techniques to the nordic spot electricity market data. 2007.

[60] Trieu Phat Luu, Sho Nakagome, Yongtian He, and Jose L Contreras-Vidal. Real-time EEG-based brain-computer interface to a virtual avatar enhances cortical involvement in human treadmill walking. *Scientific reports*, 7(1):8895, 2017.

[61] Alessandro Presacco, Larry W. Forrester, and Jose Luis Contreras-Vidal. Decoding intra-limb and inter-limb kinematics during treadmill walking from scalp electroencephalographic (EEG) signals. *IEEE Transactions on neural systems and rehabilitation engineering*, 20:212–219, March 2012.

[62] Andrés Úbeda, Álvaro Costa, Eduardo Iáñez, Elisa Piñuela-Martín, Ester Márquez-Sánchez, Antonio J. del Ama, Ángel Gil-Agudo, and José M. Azorín. Single joint movement decoding from EEG in healthy and incomplete spinal cord injured subjects. In *2015 IEEE/RSJ International Conference on Intelligent Robots and Systems (IROS)*, pages 6179–6183, October 2015. DOI: 10.1109/IROS.2015.7354258.

[63] Jose M Carmena, Mikhail A Lebedev, Roy E Crist, Joseph E O'Doherty, David M Santucci, Dragan F Dimitrov, Parag G Patil, Craig S Henriquez, and Miguel AL Nicolelis. Learning to control a brain–machine interface for reaching and grasping by primates. *PLoS biology*, 1(2):e42, 2003.

[64] Sung-Phil Kim, Justin C Sanchez, Yadunandana N Rao, Deniz Erdogmus, Jose M Carmena, Mikhail A Lebedev, MAL Nicolelis, and JC Principe. A comparison of optimal mimo linear and nonlinear models for brain–machine interfaces. *Journal of neural engineering*, 3(2):145, 2006.

[65] Andrew H Fagg, Nicholas G Hatsopoulos, Brian M London, Jacob Reimer, Sara A Solla, Di Wang, and Lee E Miller. Toward a biomimetic, bidirectional, brain machine interface. In *Engineering in Medicine and Biology Society, 2009. EMBC 2009. Annual International Conference of the IEEE*, pages 3376–3380. IEEE, 2009.

[66] Robert D Flint, Po T Wang, Zachary A Wright, Christine E King, Max O Krucoff, Stephan U Schuele, Joshua M Rosenow, Frank PK Hsu, Charles Y Liu, Jack J Lin, et al. Extracting kinetic information from human motor cortical signals. *NeuroImage*, 101:695–703, 2014.

[67] Trent J Bradberry, Rodolphe J Gentili, and Jose L Contreras-Vidal. Decoding three-dimensional hand kinematics from electroencephalographic signals. In *Engineering in Medicine and Biology Society, 2009. EMBC 2009. Annual International Conference of the IEEE*, pages 5010–5013. IEEE, 2009.

[68] Jose L Contreras-Vidal, Trent J Bradberry, and Harshavardhan Agashe. Movement decoding from noninvasive neural signals. In *Engineering in Medicine and Biology Society (EMBC), 2010 Annual International Conference of the IEEE*, pages 2825–2828. IEEE, 2010.

[69] Jiaen Liu, Christopher Perdoni, and Bin He. Hand movement decoding by phase-locking low frequency EEG signals. In *Engineering in Medicine and Biology Society, EMBC, 2011 Annual International Conference of the IEEE*, pages 6335–6338. IEEE, 2011.

[70] Patrick Ofner and Gernot R Müller-Putz. Decoding of velocities and positions of 3d arm movement from EEG. In *Engineering in Medicine and Biology Society (EMBC), 2012 Annual International Conference of the IEEE*, pages 6406–6409. IEEE, 2012.

[71] Andres Ubeda, Enrique Hortal, Eduardo Ianez, Daniel Planelles, and Jose M Azorin. Passive robot assistance in arm movement decoding from EEG signals. In *Neural Engineering (NER), 2013 6th International IEEE/EMBS Conference on*, pages 895–898. IEEE, 2013.

[72] Jeong-Hun Kim, Felix Bießmann, and Seong-Whan Lee. Decoding three-dimensional trajectory of executed and imagined arm movements from electroencephalogram signals. *IEEE Transactions on Neural Systems and Rehabilitation Engineering*, 23(5):867–876, 2015.

[73] Jinhua Zhang, Baozeng Wang, Jun Hong, and Ting Li. The analysis of decoding parameter selection of hand movements based on brain function network. In *Ubiquitous Robots and Ambient Intelligence (URAI), 2015 12th International Conference on*, pages 587–592. IEEE, 2015.

[74] Simon S. Haykin. *Adaptive Filter Theory.* Prentice-Hall information and system sciences series. Prentice Hall, 1996.

[75] Leonardo Rey Vega and Hernan Rey. *A Rapid Introduction to Adaptive Filtering.* SpringerBriefs in Electrical and Computer Engineering. Springer Berlin Heidelberg, 2012.

[76] David Freedman. *Statistical Models: Theory and Practice.* Cambridge University Press, 2009.

[77] Alvin C. Rencher and William F. Christensen. *Methods of Multivariate Analysis.* Wiley Series in Probability and Statistics. Wiley, 2012.

[78] Lennart Ljung. *System Identification: Theory for the User.* Pearson Education, 1998.

[79] J.C. Sanchez and J.C. Príncipe. *Brain-machine Interface Engineering.* Synthesis lectures on biomedical engineering. Morgan & Claypool Publishers, 2007.

[80] Melanie Mitchell. *An Introduction to Genetic Algorithms.* A Bradford book. Bradford Books, 1998.

[81] Arif Wicaksana Oyong, S Parasuraman, and Veronica Lestari Jauw. Robot assisted stroke rehabilitation: Estimation of muscle force/joint torque from emg using ga. In *Biomedical Engineering and Sciences (IECBES), 2010 IEEE EMBS Conference on*, pages 341–347. IEEE, 2010.

[82] Andrew Y Paek, Jeremy D Brown, R Brent Gillespie, Marcia K O'Malley, Patricia A Shewokis, and Jose L Contreras-Vidal. Reconstructing surface EMG from scalp EEG during myoelectric control of a closed looped prosthetic device. In *Engineering in Medicine and Biology Society (EMBC), 2013 35th Annual International Conference of the IEEE*, pages 5602–5605. IEEE, 2013.

[83] Yoshiaki Hayashi and Kazuo Kiguchi. A study of features of EEG signals during upper-limb motion. In *Advanced Intelligent Mechatronics (AIM), 2015 IEEE International Conference on*, pages 943–946. IEEE, 2015.

[84] Darrell Whitley. A genetic algorithm tutorial. *Statistics and computing*, 4(2):65–85, 1994.

[85] Marina Sokolova and Guy Lapalme. A systematic analysis of performance measures for classification tasks. *Information Processing & Management*, 45(4):427–437, 2009.

[86] Martin Billinger, Ian Daly, Vera Kaiser, Jing Jin, Brendan Z. Allison, Gernot R. Müller-Putz, and Clemens Brunner. *Is It Significant? Guidelines for Reporting BCI Performance*, pages 333–354. Springer Berlin Heidelberg, Berlin, Heidelberg, 2013.

[87] Martin Spüler, Andrea Sarasola-Sanz, Niels Birbaumer, Wolfgang Rosenstiel, and Ander Ramos-Murguialday. Comparing metrics to evaluate performance of regression methods for decoding of neural signals. In *Engineering in Medicine and Biology Society (EMBC), 2015 37th Annual International Conference of the IEEE*, pages 1083–1086. IEEE, 2015.

[88] Douglas C Montgomery and George C Runger. *Applied Statistics and Probability for Engineers.* John Wiley & Sons, 3rd edition, 2003.

[89] Rob J. Hyndman and Anne B. Koehler. Another look at measures of forecast accuracy. *International Journal of Forecasting*, 22(4):679 – 688, 2006.

[90] Xun Chen, Aiping Liu, Martin J McKeown, Howard Poizner, and Z Jane Wang. An eemd-iva framework for concurrent multidimensional EEG and

unidimensional kinematic data analysis. *IEEE Transactions on Biomedical Engineering*, 61(7):2187–2198, 2014.

[91] Justin C Sanchez, Sung-Phil Kim, Deniz Erdogmus, Yadunandana N Rao, Jose C Principe, Johan Wessberg, and Miguel Nicolelis. Input-output mapping performance of linear and nonlinear models for estimating hand trajectories from cortical neuronal firing patterns. In *Neural Networks for Signal Processing, 2002. Proceedings of the 2002 12th IEEE Workshop on*, pages 139–148. IEEE, 2002.

[92] Zheng Li, Joseph E O'Doherty, Timothy L Hanson, Mikhail A Lebedev, Craig S Henriquez, and Miguel AL Nicolelis. Unscented kalman filter for brain-machine interfaces. *PloS one*, 4(7):e6243, 2009.

[93] Jun Lv, Yuanqing Li, and Zhenghui Gu. Decoding hand movement velocity from electroencephalogram signals during a drawing task. *Biomedical engineering online*, 9(1):64, 2010.

[94] Francis R Willett, Aaron J Suminski, Andrew H Fagg, and Nicholas G Hatsopoulos. Improving brain–machine interface performance by decoding intended future movements. *Journal of neural engineering*, 10(2):026011, 2013.

[95] Trieu Phat Luu, Yongtian He, Samuel Brown, Sho Nakagome, and Jose L Contreras-Vidal. Gait adaptation to visual kinematic perturbations using a real-time closed-loop brain-computer interface to a virtual reality avatar. *Journal of Neural Engineering*, 13(3), 2016.

[96] Joseph T. Gwin, Klaus Gramann, Scott Makeig, and Daniel P. Ferris. Removal of movement artifact from high-density EEG recorded during walking and running. *Journal of Neurophysiology*, 103(6):3526–3534, 2010. PMID: 20410364.

[97] Luis Fernando Nicolas-Alonso and Jaime Gomez-Gil. Brain computer interfaces, a review. *Sensors*, 12(2):1211–1279, 2012.

[98] Jeong-Hun Kim, Ricardo Chavarriaga, José del R Millán, and Seong-Whan Lee. Three-dimensional upper limb movement decoding from EEG signals. In

Brain-Computer Interface (BCI), 2013 International Winter Workshop on, pages 109–111. IEEE, 2013.

[99] Aapo Hyvärinen. Fast and robust fixed-point algorithms for independent component analysis. *IEEE transactions on Neural Networks*, 10(3):626–634, 1999.

[100] Pierre Comon. Independent component analysis, a new concept? *Signal processing*, 36(3):287–314, 1994.

[101] Aapo Hyvärinen and Erkki Oja. Independent component analysis: algorithms and applications. *Neural networks*, 13(4-5):411–430, 2000.

[102] Maarten Mennes, Heidi Wouters, Bart Vanrumste, Lieven Lagae, and Peter Stiers. Validation of ICA as a tool to remove eye movement artifacts from EEG/ERP. *Psychophysiology*, 47(6):1142–1150, 2010.

[103] Filipa Campos Viola, Stefan Debener, Jeremy Thorne, and Till R Schneider. Using ICA for the analysis of multi-channel EEG data. *Simultaneous EEG and fMRI: Recording, Analysis, and Application: Recording, Analysis, and Application*, pages 121–133, 2010.

[104] Ruhi Mahajan and Bashir I Morshed. Unsupervised eye blink artifact denoising of EEG data with modified multiscale sample entropy, kurtosis, and Wavelet-ICA. *IEEE journal of Biomedical and Health Informatics*, 19(1):158–165, 2015.

[105] Md Kafiul Islam, Amir Rastegarnia, and Zhi Yang. Methods for artifact detection and removal from scalp EEG: A review. *Neurophysiologie Clinique/Clinical Neurophysiology*, 46(4-5):287–305, 2016.

[106] E Iáñez, Á Costa, E Ceseracciu, E Márquez-Sánchez, E Piñuela-Martín, G Asín, AJ del Ama, Á Gil-Agudo, M Reggiani, JL Pons, et al. Experimental architecture for synchronized recordings of cerebral, muscular and biomechanical data during lower limb activities. In *Control and Automation (MED), 2015 23th Mediterranean Conference on*, pages 143–149. IEEE, 2015.

[107] Valer Jurcak, Daisuke Tsuzuki, and Ippeita Dan. 10/20, 10/10, and 10/5 systems revisited: their validity as relative head-surface-based positioning systems. *Neuroimage*, 34(4):1600–1611, 2007.

[108] CDC/National Center for Health Statistics. Disability and Functioning (Non-institutionalized Adults Aged 18 and Over). [Online; accessed April 9, 2018].

[109] Leigh R. Hochberg, Mijail D. Serruya, Gerhard M. Friehs, Jon A. Mukand, Maryam Saleh, Abraham H. Caplan, Almut Branner, David Chen, Richard D. Penn, and John P. Donoghue. Neuronal ensemble control of prosthetic devices by a human with tetraplegia. *Nature*, 442:164–171, 2006.

[110] Stephan Waldert, Tobias Pistohl, Christoph Braun, Tonio Ball, Ad Aertsen, and Carsten Mehring. A review on directional information in neural signals for brain-machine interfaces. *J. Physiol. (Paris)*, 103:244–254, 2009.